TECHNISCHE UNIVERSITÄT MÜNCHEN

Fakultät für Physik
Lehrstuhl E23 für Technische Physik

Walther-Meißner-Institut für Tieftemperaturforschung
der Bayerischen Akademie der Wissenschaften

Spin Pumping in Ferrimagnet/Normal Metal Bilayers

Johannes Robert Karl Lotze

Vollständiger Abdruck der von der Fakultät für Physik der Technischen Universität München zur Erlangung des akademischen Grades eines

Doktors der Naturwissenschaften

genehmigten Dissertation.

Vorsitzender:		Univ.-Prof. Dr. Björn Garbrecht
Prüfer der Dissertation:	1.	Univ.-Prof. Dr. Rudolf Gross
	2.	apl. Prof. Dr. Martin S. Brandt

Die Dissertation wurde am 01.06.2015 bei der Technischen Universität München eingereicht und durch die Fakultät für Physik am 21.07.2015 angenommen.

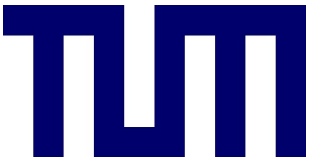

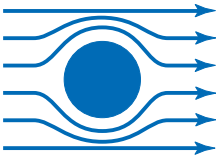

TECHNISCHE
UNIVERSITÄT
MÜNCHEN

WALTHER-MEIßNER-
INSTITUT FÜR TIEF-
TEMPERATURFORSCHUNG

BAYERISCHE
AKADEMIE DER
WISSENSCHAFTEN

Spin Pumping in Ferrimagnet/Normal Metal Bilayers

Dissertation
by
Johannes Lotze

Abstract

This thesis deals with different aspects of spin pumping. Spin pumping is a method of generating a pure spin current in a ferromagnet/normal metal bilayer. In a series of electrically detected spin pumping experiments on yttrium iron garnet (YIG)/platinum bilayer samples with variable platinum thickness, we characterize the spin Hall angle and the spin diffusion length of platinum. We also analyze the dependence of spin pumping on the yttrium iron garnet layer thickness, and observe a strong enhancement of spin pumping efficiency for thick ($t_{\mathrm{YIG}} > 60\,\mathrm{nm}$) YIG layers.

We investigate the possibility of using electrically detected spin pumping to directly measure the excitation of the magnetization in a strongly coupled system consisting of a YIG single crystal and a microwave cavity. We develop a model, based on input-output theory, which is valid in the weak and strong coupling limit, to calculate the magnetization excitation in such a system and to predict the spin pumping signal as a function of microwave frequency and magnetic field. We compare the model predictions to the experimental observations, finding good quantitative agreement in the weakly coupled case. In the strongly coupled case, our model allows us to exclude spin pumping as a possible source of the observed dc voltage signal.

Spin pumping is modeled for the first time in ferrimagnetic systems, taking into account the richer magnetic structure of ferrimagnets as compared to that of ferromagnets, which features multiple magnetic sublattices. We find that in ferrimagnets, the polarization direction of the pumped spin current depends on the effective gyromagnetic ratio, but not on the orientation of the magnetic sublattice at the normal metal interface. We verify our model experimentally by performing spin pumping on a gadolinium iron garnet/platinum bilayer as a function of temperature. We extend our model to antiferromagnets and find that they have a lower spin pumping efficiency relative to ferromagnets.

Finally, we conduct for the first time microwave frequency spin Hall magnetoresistance experiments on YIG/platinum bilayer samples. We show that the spin Hall angle in platinum is frequency independent up to frequencies of at least 3 GHz. Our experiments also show that it is possible to read out the orientation of the magnetization of the yttrium iron garnet film at GHz frequencies.

Contents

Chapter 1

Introduction

In electronic devices today, the charge of the electron is used to transport and manipulate information. However, electrons do not only carry charge but also spin, quantum mechanical angular momentum. Spintronics is the field of research that wants to take advantage of the electron spin, which also can be used to transport and store information encoded in orientation of the electron spin. Today spintronics is a very diverse field of research [1–3]. One distinguishes between spin-polarized currents, which is a flow of electrons in which the majority of electron spins are oriented either up or down, and pure spin currents. A pure spin current is a directed flow of angular momentum without an associated net flow of charge, which has even been suggested to be dissipation-free, because it is invariant under time-reversal [4]. For the transport of information, this would be a great advantage of pure spin currents over electric currents, which cause Joule heating, thus impeding miniaturization due to cooling issues. The idea of using spin currents for logic operations in semiconductors has existed for quite some time, since the spin field effect transistor was first suggested by Datta and Das [5] in 1990. The development of methods for the generation of pure spin currents has therefore been of considerable interest. By far the most technologically relevant innovation in the field of spintronics is the discovery of the giant magnetoresistance effect by Fert [6] and independently Grünberg [7], for which they were awarded the Nobel prize in physics in 2007. Their discovery and that of the related tunneling magnetoresistance enabled the construction of magnetic tunnel junctions. In these devices, featuring alternating layers of magnetic and non-magnetic materials, the resistance depends of the relative orientation of the magnetic layers, making magnetic tunnel junctions very sensitive magnetic field sensors. They are today used in read heads of magnetic mass storage media, in which information is stored in a magnetized

disk.

Magnetic tunnel junctions can also be directly used to store information, in the orientation of the magnetic layers, which is exploited for example in magnetoresistive random access memory (MRAM). MRAM allows for very fast read and write operations, like today's electric random access memory (RAM). In addition to very fast data rates, the memory is also non-volatile, meaning that the stored information persists even when power is cut, like in today's hard disks. It is therefore conceivable to integrate data storage and RAM. The persistence of information in MRAM also makes it energy efficient. To perform a write operation in MRAM, the magnetization in a magnetic layer of a tunnel junction needs to be reoriented. Reorienting the magnetization usually necessitates the use of an external magnetic field, which is generated by an electric current flowing in a lead. This electric current also produces a considerable amount of heat, which limits data density and speed. At the same time, stray magnetic fields from the current lead need to be prevented from interacting with neighboring magnetic elements, causing write errors. The use of spin currents instead of magnetic fields to reorient the magnetization of MRAM cells resolves these problems. Spin currents, injected into a magnetic material, can change the magnetization orientation in ferromagnets due to spin transfer torque [8–10]. Such a spin current can be directly channeled to the magnetic element, where it acts locally, eliminating stray fields. Spin transfer torque switching using pure spin currents also reduces the amount of heat generated in the writing process.

The inverse of the spin transfer torque is spin pumping: The magnetization of a ferromagnetic thin film is excited in a non-equilibrium state which generates a pure spin current flowing into an adjacent normal metal. If the magnetization of the magnetic material is resonantly excited (ferromagnetic resonance, FMR), one speaks of spin pumping [11–16]. On the other hand, if the non-equilibrium state of the spin system is due to a thermal gradient between the magnetic material and the normal metal, the spin current generation process is referred to as the spin Seebeck effect (SSE) [17–23]. Conversely, a pure spin current can also be generated in the normal metal. By driving a current parallel to the ferromagnet/normal metal interface, a spin current is induced which propagates perpendicularly to the interface, due to the spin Hall effect [24–26]. The magnetization orientation dependent absorption of that spin current is the basis of the recently discovered spin Hall magnetoresistance (SMR) [27–29].

This thesis investigates spin current generation in magnetic material/normal metal bilayers. The exploration of methods for generating a pure spin current is one of the essential steps in the advancement of spintronics research. Spin pumping is one such method and is here examined in new contexts, such as that of strong coupling, of compensating ferrimagnets, and of antiferromagnets. The frequency dependence of the spin Hall effect, another method for creating a pure spin current, is probed in this thesis using the SMR effect.

The thesis is organized as follows: In chapter 2, the basic ingredients of the spin pumping mechanism are discussed. These are further illustrated in chapter 3, in which we describe electrically detected spin pumping in thin film bilayers of the magnetic insulator yttrium iron garnet (YIG) and the normal metal platinum. Thereby, we vary both the layer thicknesses of the YIG and of the Pt layers. Varying the layer thickness of the platinum allows us to determine the relevant properties for spin current propagation in platinum, namely the spin diffusion length, which governs the distance a spin current can propagate in the material before decaying and the spin Hall angle, which controls the efficiency of its conversion into a charge current due to the inverse spin Hall effect.

In chapter 4, we contrast spin pumping in a YIG thin film/Pt bilayer sample and in a bulk single crystal YIG/Pt bilayer sample. In a microwave cavity-based spin pumping experiment, the transition from thin film to bulk YIG causes an enhancement of the coupling between the photonic excitations in the cavity and the magnonic excitations of the spin system of the YIG, so that superposition states form. We model the cavity excitation as well as the excitation of the spin system and predict the spin pumping voltage generated in the thin film as well as bulk cases, both as a function of microwave frequency and magnetic field. In particular, we are able to quantitatively predict the spin pumping signal from a FMR measurement, using only the spin mixing conductance, the spin diffusion length and the spin Hall angle. We find that in bilayer samples where the ferromagnet is of greater volume, the spin pumping signal decreases relative to thin film ferromagnet bilayers. Our model is quantitatively consistent with electrically detected spin pumping experiments performed on a thin film YIG/Pt bilayer sample. In analyzing spin pumping data on a bulk YIG/Pt bilayer sample, our model allows us to distinguish voltage signals due to spin pumping and voltage signals due to the spin Seebeck effect.

In chapter 5, we discuss spin pumping in ferrimagnets and antiferromagnets. In

the context of magnetic storage, using antiferromagnets is advantageous, as they do not produce any stray magnetic fields [30]. Furthermore the spin current needed for switching of the magnetization orientation is predicted to be smaller than in ferromagnets [31]. Conversely, ferrimagnets and antiferromagnets are magnetically more complicated than ferromagnets. While ferromagnets can be described in terms of one single magnetic moment, ferrimagnets and antiferromagnets comprise at least two magnetic sublattices. We model the spin pumping spin current in ferrimagnet/normal metal. We find that the orientation of the polarization of the dc spin current generated by spin pumping depends only on the effective gyromagnetic ratio of the ferrimagnet. We then confirm our model by performing spin pumping experiments on gadolinium iron garnet, a compensating ferrimagnet in which the magnetic system is strongly temperature dependent, as a function of temperature. Using the same approach as for ferrimagnets, we calculate the spin pumping amplitude in an easy-axis-antiferromagnet/normal metal bilayer sample. We then perform spin pumping as a function of magnetic field and microwave frequency on the easy-axis antiferromagnet manganese(II) fluoride.

In chapter 6, we take a closer look at the spin Hall magnetoresistance (SMR), performing magnetoresistance experiments at microwave frequencies. Previously only performed using dc charge currents, we here perform SMR measurements at microwave frequency. Microwave frequency spin Hall magnetoresistance measurements give insight into the interaction time governing the spin Hall effect. In the SMR effect, the orientation of the magnetization in a magnetic layer can be probed without the use of a magnetic field using the magnetization orientation dependent transmission of a spin current across the interface. It thus explores the possibility of using the SMR effect to quickly read the magnetization orientation in a ferromagnetic element. We develop and calibrate a test fixture for a thin film YIG/Pt bilayer, capable of supporting ac microwave current. We then measure the impedance of the YIG/Pt bilayer as a function of magnetic field orientation as well as microwave frequency, for frequencies of up to 8 GHz. Our results show that within experimental accuracy, the spin Hall magnetoresistance is independent of frequency for frequencies of at least 3 GHz.

Finally, a summary of the most important results of this thesis is given in chapter 7.

Chapter 2

Foundations of Spin Pumping

In a bilayer of a ferromagnetic material and a normal metal the damping and therefore linewidth of ferromagnetic resonance (FMR) is increased compared to the bulk material value. This phenomenon prompted Tserkovnyak *et al.* [32–34] to propose the spin pumping mechanism, which has since been well established. [11–16, 35, 36]. Spin puming is illustrated in Fig. 2.1. In FMR, the magnetization of the ferromagnetic material is resonantly excited by microwave radiation. The precessing magnetization drives a spin current flowing into the normal metal, in a parametric pumping process. This transfer of angular momentum from the ferromagnet to the normal metal acts as an additional damping mechanism for the precession of the magnetization of the ferromagnet in ferromagnetic resonance. Spin pumping is thus a method of generating a pure spin current in a bilayer of a magnetic material and a normal metal. Spin currents are a directed flow of angular momentum. In addition to their propagation direction, spin currents are also characterized by the orientation of the spin current polarization. A more detailed discussion of spin currents can be found in Ref. [37]. In the case of spin pumping, the spin current flow direction is normal to the ferromagnet/normal metal interface [32]. The polarization depends on the magnetization orientation in the ferromagnet. Spin pumping is generally divided into two parts: The first is dc spin pumping, where the polarization of the spin current (i.e., the spin orientation) is in the direction of the equilibrium magnetization of the ferromagnet. The second is ac spin pumping, where the polarization direction changes at the same frequency as the precession frequency [15, 38]. In the course of this thesis, dc spin pumping experiments were performed. In the following chapter, we discuss the fundamental ingredients of the dc spin pumping mechanism.

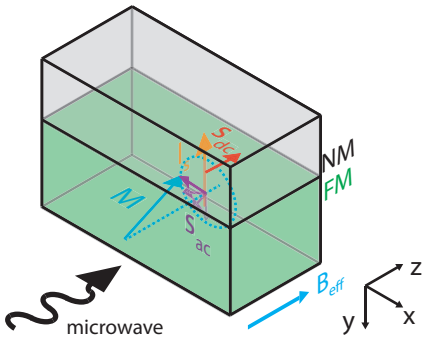

Figure 2.1: The spin pumping mechanism: A microwave magnetic field is used to excite the magnetization M of the ferromagnet, which precesses. The relaxing magnetization generates a spin current flowing from the ferromagnet into the normal metal along y. The spin current comprises a dc part with a polarization $\mathbf{s}$ along the magnetic field direction $\mathbf{B}_{\text{eff}}$ and an ac part with a polarization direction which rotates in the x-y plane with the ferromagnetic precession frequency.

2.1 Ferromagnetic Resonance

We start by giving a short overview of ferromagnetic resonance, the resonant absorption of microwave radiation by a ferromagnetic material [39]. In a ferromagnet, the magnetic moments are coupled by exchange interaction. Thus, they are aligned parallelly even in small external magnetic fields. The magnetic moments can then be described within the macrospin approximation by the magnetizaton $\mathbf{M}$ [40]. In an external magnetic field $\mathbf{B}_0 = B_0\mathbf{e}_z$,[1] a force is acting to align $\mathbf{M}$ along $\mathbf{B}_0$. This force acts to align the magnetization and external magnetic field. There is an angular momentum $\mathbf{L} = \mathbf{M}V/\gamma$ associated with the magnetization, where γ is the gyromagnetic ratio and V is the volume of the ferromagnet. In ferromagnetic systems, where unpaired electrons provide the magnetic moment, the gyromagnetic ratio is negative, due to the negative charge of the electron. The magnetic moment and angular momentum of an electron are thus antiparallel [41]. The force that tries to align the magnetization with the external magnetic field thus generates a torque on the angular momentum of the ferromagnet. This results in a precessional motion of the magnetization and angular momentum vectors around the magnetic field axis. The

[1] In this thesis, $B_0 = \mu_0 H_0$, where H_0 is the externally applied magnetic field. However, we will use the term external magnetic field or applied magnetic field also for B_0.

dynamics of the magnetization can be expressed as

$$\dot{\mathbf{M}} = \gamma \mathbf{M} \times \mathbf{B}_0 \,, \tag{2.1}$$

The precession frequency of the system is

$$\boldsymbol{\omega} = \gamma \mathbf{B} \,. \tag{2.2}$$

In addition to an external magnetic field, there are also internal fields, stemming from the crystalline and shape anisotropies as well as exchange interaction. To take into account the anisotropies, the external magnetic field $\mathbf{B}_0$ is replaced by an effective magnetic field $\mathbf{B}_{\text{eff}}$ in a ferromagnet. It can be calculated by [39]

$$B_{i,\text{eff}} = \frac{\partial F}{\partial M_i} \,, \tag{2.3}$$

where F is the free energy density of the ferromagnet. The free energy density in a single domain ferromagnet consists of $F = F_{\text{Z}} + F_{\text{A}} + F_{\text{S}}$, where F_{Z} is the Zeeman energy density, F_{A} is the energy density of the crystalline anisotropy and F_{S} is the free energy density of the shape anisotropy [39]. In a ferromagnet with multiple magnetic domains, exchange energy also needs to be taken into account.

According to Eq. (2.1), the magnetization will precess for an infinitely long time once it is excited. There are however dissipative processes that allow the magnetization to return to its equilibrium position along the effective magnetic field. This damping is usually expressed as a viscous damping term which is amended to Eq. (2.1), resulting in the well-known Landau-Lifschitz-Gilbert (LLG) equation [39, 42]:[2]

$$\dot{\mathbf{M}} = \gamma \mathbf{M} \times \mathbf{B}_{\text{eff}} + \frac{\alpha}{M} \mathbf{M} \times \dot{\mathbf{M}} \,, \tag{2.4}$$

where we have introduced the Gilbert damping constant α. The second summand in Eq. (2.4) is a change in magnetization direction perpendicular to both $\mathbf{M}$ and $\dot{\mathbf{M}}$ and causes the magnetization to spiral back to a position along $\mathbf{B}_{\text{eff}}$.

In FMR, the precession of the magnetization is driven by a time-dependent microwave magnetic field $\mathbf{b}_1(t)$. This process is most efficient when the $\mathbf{b}_1(t)$ oscillates

[2] Eq. (2.4) is strictly true only as long as $\alpha \ll 1$. Otherwise, the precession frequency will be a function of $1/(1+\alpha^2)$. However, in this thesis we only treat cases where the condition $\alpha \ll 1$ is fulfilled. For more information, we refer to [39]

at the eigenfrequency of the magnetization precession. Thus the absorption of microwave radiation by the ferromagnet is frequency dependent. The absorption of microwaves is given by the imaginary part of the rf susceptibility χ''. A thorough derivation of the rf susceptibility is available in Ref. [40]. For the purpose of this thesis it is sufficient that the rf susceptibility as a function of the magnetic field is described by a Lorentzian with a half width half maximum linewidth of [40]

$$\Delta B = \alpha\omega/\gamma\,. \tag{2.5}$$

The cone angle of the magnetization precession θ depends on the ratio of microwave power and FMR linewidth and is in resonance and for small cone angles calculated as [43]:

$$\theta = \frac{b_1}{\Delta B}\,, \tag{2.6}$$

where b_1 is the effective amplitude of the microwave magnetic field. Note that Eq. (2.6) is valid only assuming that all damping is viscous (Gilbert-like). The cone angle of the magnetization precession therefore depends on both the ac magnetic field strength and the damping.

2.2 The Spin Pumping Mechanism

We will in this section introduce the spin pumping mechanism from the point of view of an angular momentum conservation, a principle we will discuss in greater detail in Sect. 5.1. Since the magnetization M of a spin system is associated with an angular momentum $\gamma L = MV$, where V is the volume of the ferromagnet, the precession of the magnetization in ferromagnetic resonance also entails a precession of an angular momentum around the magnetic field axis. The torque needed for the precession of the angular momentum is provided by the effective magnetic field. The torque needed for the damping of the magnetization is exerted by the lattice, via magnetoelastic interactions [42]. In a ferromagnet in contact with a normal metal, the damping torque can also be exerted by the normal metal, via the absorption of a spin current. This so-called spin pumping process thus can be described by an expression which has the same form as the Gilbert damping term in Eq. (2.4). As compared to an isolated ferromagnet with Gilbert damping constant α_0, the effective damping constant of the

ferromagnet in a ferromagnet/normal metal bilayer thus reads

$$\alpha = \alpha_0 + \alpha' \,, \tag{2.7}$$

where α_0 is the value of the damping constant in the ferromagnet without any contact to a normal metal.

Following Ref. [32], the spin pumping damping constant α' depends on the efficiency of the spin current absorption of the normal metal, which is described by the spin-mixing conductance $g^{\uparrow\downarrow}$. The spin-mixing conductance $g^{\uparrow\downarrow}$ depends on the interface quality between the ferromagnet and the normal metal, but does not strongly depend on the material combination at the interface [12]. It can be related to the damping parameter α' by [32]

$$\alpha' = \frac{g^{\uparrow\downarrow} g \mu_{\mathrm{B}}}{4\pi M V} \,, \tag{2.8}$$

where g is the Landé g factor, μ_{B} is the Bohr magneton, and V is the volume of the ferromagnet. Following Refs. [32,33], the spin current density pumped into the normal metal is:

$$I_{\mathbf{s}} = \frac{\hbar g^{\uparrow\downarrow}}{4\pi} \mathbf{m} \times \dot{\mathbf{m}} \,, \tag{2.9}$$

where $\mathbf{m}$ is the unit vector of magnetization. The flow direction of $J_{\mathbf{s}}$ is from the ferromagnet to the normal metal, normal to the interface. The orientation of the spin current polarization $\mathbf{s}$ is along $\mathbf{m} \times \dot{\mathbf{m}}$, and thus oscillates with the FMR frequency.

The dc part of the spin pumping is found by time-averaging the spin current. In ferromagnetic resonance precession with small precession cone angles, the unit vector of magnetization can be expressed as $\mathbf{m} = (m_1 \cos(\omega t), m_1 \sin(\omega t), 1)$. Here $m_1 = \sin(\theta)$ It follows that in an effective magnetic field along z,

$$[\mathbf{m} \times \dot{\mathbf{m}}] = \omega \sin^2(\theta) \mathbf{e}_z \,, \tag{2.10}$$

where [...] denotes time averaging. All spin current polarization components which are not along the z-direction are averaged to zero and one finds [12,35]:

$$I_z = \frac{\hbar}{4\pi} \omega g^{\uparrow\downarrow} \sin^2 \theta \,, \tag{2.11}$$

where the precession cone angle θ depends on both the microwave power used to excite FMR and the damping parameter α (see Eq. (2.6)). In chapter 5.1.1, this expression

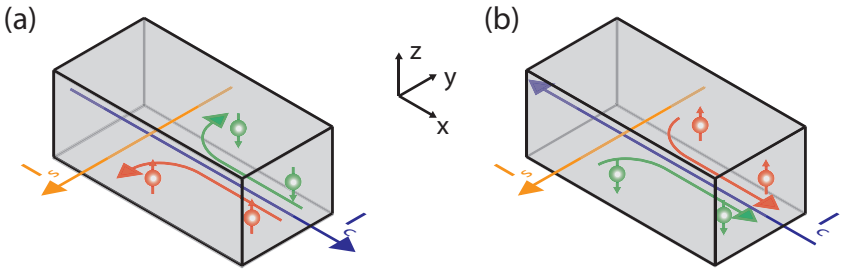

Figure 2.2: (a) The spin Hall effect: The spin 'up' and spin 'down' electrons in a charge current $\mathbf{I}_c$ propagating in a metal are scattered opposite ways, resulting in a spin current $\mathbf{I}_\mathbf{s}$, perpendicular to both the direction of $\mathbf{I}_c$ and the spin current polarization $\mathbf{s}||\mathbf{e}_z$ (b) The inverse spin Hall effect: A spin current, consisting of spin 'up' and spin 'down' electrons traveling in opposite direction, is injected into a metal. Spin 'up' and spin 'down' electrons are scattered in opposite directions relative to their direction of travel. A charge current ensues, which is unpolarized, and perpendicular to both the spin current propagation direction and the spin current polarization.

will be further motivated.

2.3 Measuring Spin Pumping

Spin pumping can be measured in two ways: The first method is to compare the ferromagnetic resonance linewidth of a ferromagnet in contact with a normal metal layer with the linewidth of the same ferromagnetic material without the normal metal, as performed in Ref. [44]. This allows one to measure the damping constants α_0 and α' (Eqs. (2.7) and (2.5)). It is thus possible to measure the spin-mixing conductance directly (Eq. (2.8)). Here, we describe in detail only the second method, electrically detected spin pumping. This method is based on measuring the spin current across the interface instead of the increased damping in FMR. However, it is not straightforward to detect a spin current – one cannot simply buy spin current detection electronics. Instead, in this work we exploit the inverse spin Hall effect [25, 26] to convert the spin current into a charge current which is easily measurable [36].

2.3.1 The Spin Hall and Inverse Spin Hall Effects

We here describe the spin Hall effect and its inverse in a purely phenomenological way. We start with the spin Hall effect [25]. The mechanism is presented in Fig. 2.2(a). If

an unpolarized charge current $\mathbf{I}_c$, consisting of an equal number of spin 'up' and spin 'down' electrons, is injected into a normal metal along the x-direction, electrons are predominantly scattered in the y-direction perpendicular to both the current direction and the spin polarization direction of the electron. If this scattering is due to spin orbit mechanisms, such as skew-scattering [45], side jump scattering [46], and intrinsic interactions [47], the scattering direction is spin-dependent: While spin 'up' electrons are scattered in negative y-direction, spin 'down' electrons are scattered in positive y-direction. The result is a pure spin current in negative y-direction: the same number of spin 'up'-electrons travel in negative y-direction as spin 'down' electrons travel in positive y-direction. The spin current can thus be described as $\mathbf{I}_\mathrm{s} = \mathbf{I}_\mathrm{s}{}^{\uparrow} - \mathbf{I}_\mathrm{s}{}^{\downarrow}$. The spin Hall effect is given by

$$\mathbf{I}_\mathrm{s} = \theta_\mathrm{SH} \left(-\frac{\hbar}{2e}\right) \mathbf{s} \times \mathbf{I}_\mathrm{c}\,, \tag{2.12}$$

where θ_SH is the spin Hall angle, parameterizing the strength of the spin orbit coupling in the metal. $\mathbf{s}$ is the polarization direction of the spin current. The ratio between the spin and charge of the electron is $-\hbar/2e$. [3]

The opposite process is also possible: A spin current can be converted to a charge current. This process is then called the inverse spin Hall effect (Fig. 2.2(b)). Consider a pure spin current polarized along positive z-direction injected along the negative y-direction. It consists of equal parts spin 'up' electrons traveling in negative y-direction and spin 'down' electrons traveling in positive y-direction. These are again scattered spin-dependently: spin 'up' electrons are scattered to the left relative to their propagation direction, in x-direction. spin 'down' electrons are scattered to the right, also in x-direction. A non-polarized charge current in negative x-direction ensues $\mathbf{I}_\mathrm{c} = \mathbf{I}_\mathrm{c}{}^{\uparrow} + \mathbf{I}_\mathrm{c}{}^{\downarrow}$ The inverse spin Hall effect is described by:

$$\mathbf{I}_\mathrm{c} = \theta_\mathrm{SH} \left(-\frac{2e}{\hbar}\right) \mathbf{s} \times \mathbf{I}_\mathrm{s}\,. \tag{2.13}$$

The spin Hall angle is identical for the direct spin Hall and inverse spin Hall effects, since they depend on the same scattering mechanisms.

[3] Note that the charge of the electron is $q_\mathrm{e} = -e$.

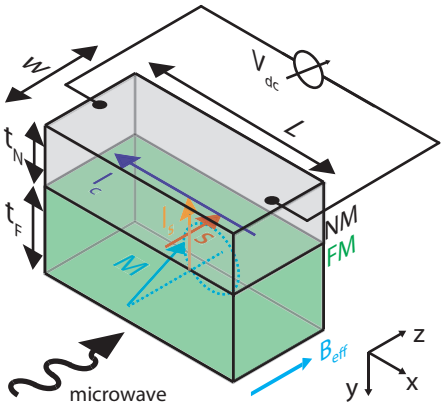

Figure 2.3: Electrically detected dc spin pumping: A microwave magnetic field is used to excite the magnetization M of the ferromagnet, which precesses. The relaxing magnetization generates a dc spin current flowing from the ferromagnet into the normal metal (along y), with a polarization $\mathbf{s}$ along the magnetic field direction $\mathbf{B}_{\text{eff}}$. In the normal metal, it is converted into a charge current by the inverse spin Hall effect. The dc component of this spin current can then be measured as a dc voltage between contacts placed at either end of the sample.

2.3.2 Electrically Detected Spin Pumping

The inverse spin Hall effect is a valuable tool in measuring spin currents since it allows for the conversion of spin currents into charge currents, which can then be measured electrically. In open circuit condition, the charge current generated by the inverse spin Hall effect causes a measurable electric voltage between two contacts placed orthogonally to the spin polarization direction $\mathbf{s}$.

The measurement geometry for electrically detected spin pumping, i.e., for the detection of the pumped spin current via the inverse spin Hall effect, is shown in Fig. 2.3. The magnetization of the ferromagnet (shown in green) is excited in FMR by microwave radiation. The precession of the magnetization around its equilibrium position along the effective magnetic field $\mathbf{B}_{\text{eff}}$ generates a spin current $\mathbf{I}_{\mathbf{s}}$ with a propagation direction normal to the ferromagnet/normal metal interface. The orientation of the dc spin current polarization $\mathbf{s}$ is given by the orientation of the effective magnetic field. In the normal metal this spin current is converted to a charge current due to the inverse spin Hall effect and is then electrically detected as a voltage in open circuit conditions. Since the direction of the charge current and thus the polarity of the voltage depends on the polarization direction of the spin current, it can be inferred from the polarity of the measured dc voltage signal. The measured dc volt-

age in ferromagnetic resonance in an electrically detected spin pumping experiment is [12, 35, 37]:[4]

$$V_{\mathrm{sp}} = e g^{\uparrow\downarrow} \theta_{\mathrm{SH}} \lambda_{\mathrm{SD}} \tanh\left(\frac{t_{\mathrm{N}}}{2\lambda_{\mathrm{SD}}}\right) \frac{\omega}{2\pi} R w \sin^2(\theta) P \eta \,, \tag{2.14}$$

where e is the elementary charge, t_{N} is the thickness of the normal metal layer, R is the resistance of the bilayer, and w is the width of the bilayer. λ_{SD} is the spin diffusion length of the normal metal, i.e., the distance that a spin current can travel in a metal before it vanishes due to spin flip scattering processes in the normal metal [35]. P is the ellipticity correction factor which is introduced to take into account that the precession of the magnetization in a ferromagnet is in general not circular but elliptical, due to the crystalline and shape anisotropies present in the ferromagnet. Elliptical precession can either be more or less efficient than circular precession at pumping spin current [48], depending on the anisotropies and the frequency of the FMR precession. In this thesis, we investigate spin pumping in yttrium iron garnet (YIG) as a ferromagnet, at X-band frequencies (10 GHz). The ellipticity correction factor is very close to one in this regime [37]. Therefore in the following it is disregarded, by setting $P = 1$.

The spin backflow correction factor [49]

$$\eta = \left(1 + 2 g^{\uparrow\downarrow} \rho \lambda_{\mathrm{SD}} \frac{e^2}{h} \coth\left(\frac{t_{\mathrm{N}}}{\lambda_{\mathrm{SD}}}\right)\right)^{-1} \tag{2.15}$$

takes into account the fact that the normal metal layer is not a perfect spin sink. In spin pumping, the spin current injected into the normal metal will cause a spin accumulation to build up in the normal metal. This spin accumulation drives a spin current back into the ferromagnet, thus reducing the effective spin current. However, the spin current injected into the normal metal will decay on the length scale of the spin diffusion length λ_{SD}. Consequently no spin accumulation can build up further away from the ferromagnet/metal interface than λ_{SD}. The spin current driven by any spin accumulation close to the interface therefore flows away from the interface, instead of back toward the ferromagnet. If the normal metal layer is thicker than the spin diffusion length in the normal metal, the backflow is small, and $\eta \approx 1$.

It is important to note that V_{sp} is independent of w, since R is proportional to $1/w$.

[4] Although technically this voltage is an inverse spin Hall effect voltage due to a spin current generated by spin pumping, in the following, this voltage will often be referred to simply as 'spin pumping voltage'

Conversely, it is possible to increase the V_{sp} signal by increasing the length L of the sample, thus increasing R.

Eq. (2.14) does not imply that an increase in $g^{\uparrow\downarrow}$ always leads to an increased dc voltage in resonance. In fact, according to Eqs. (2.5)-(2.8), increasing $g^{\uparrow\downarrow}$ leads to an increase in the damping constant, which in turn decreases θ (assuming the microwave magnetic field is kept constant). The reduced precession cone angle leads in turn to a decrease in the dc pumped spin current and thus V_{sp}. The dependence of V_{sp} on $g^{\uparrow\downarrow}$ (using $g^{\uparrow\downarrow} \propto \alpha'$, and $\sin^2(\theta) \propto 1/\alpha^2$) is summarized in terms of damping constants as:

$$V_{\mathrm{sp}} \propto \frac{\alpha'}{(\alpha_0 + \alpha')^2}\,. \tag{2.16}$$

An increase in $g^{\uparrow\downarrow}$ viz. α' is therefore beneficial until the magnetic resonance linewidth increase from spin pumping is equal to the linewidth of the bulk ferromagnet, $\alpha_0 = \alpha'$. A further increase in $g^{\uparrow\downarrow}$ beyond this point then decreases the dc pumped spin current and V_{sp}. In ferromagnets with low damping constants, such as ytrrium iron garnet [50] or permalloy [51], $\alpha' > \alpha_0$ is easily achieved. In other words, to optimize V_{dc} in a system consisting of a low linewidth ferromagnet and a normal metal, the interface between the ferromagnet and normal metal should not be 'too perfect'. We stress that the pumped spin current (i.e. the dc voltage) does not increase with increasing FMR frequency ω. Instead, Eqs. (2.5) and (2.6) show that the precession cone angle θ is inversely proportional to the microwave frequency (if the damping is entirely Gilbert-like). It follows that V_{sp} in effect scales as

$$V_{\mathrm{sp}} \propto 1/\omega\,. \tag{2.17}$$

At a given microwave input power, spin pumping is therefore more efficient at lower frequencies, as is also pointed out in Ref. [35].

2.3.3 Rectification Effects

In a typical electrically detected spin pumping experiment, the dc voltage that is measured between the contacts is not entirely due to spin pumping. Microwave rectification effects can also play a role. These dc voltages are generated by the down-conversion of a microwave ac current in a metallic conductor due to the resistance in that metal changing at the same frequency. The microwave current is induced by

the microwave electric field of the cavity or waveguide resonator used to drive the FMR in spin pumping experiments. Although the sample is placed in such a way that the microwave magnetic field b_1 is optimized, part of the sample and dc leads are exposed to the microwave electric field as well. The oscillating resistance is due to magnetoresistance effects. If the ferromagnet used in spin pumping is metallic the angle-dependent magnetoresistance (AMR) effect modulates the resistance due to the periodic change in direction of the magnetization of the ferromagnetic material in ferromagnetic resonance precession [52–54]. If the ferromagnet used is an insulator, the spin Hall magnetoresistance effect (see chapter 6) modulates the resistance of the normal metal film in a similar fashion [55, 56]. In cavity-based spin pumping experiments, SMR rectification voltages are usually smaller than spin pumping voltages, except when spin pumping is suppressed (see chapter 5.1). In both AMR and SMR rectification, the oscillating current and resistance homodyne, as

$$U(t) = (R_0 + R_1 \cos(\omega t)) I \cos(\omega t + \phi) \tag{2.18}$$

$$= \frac{R_1 I}{2} \cos(\phi) + R_0 I \cos(\omega t + \phi) + \frac{R_1 I}{2} \cos(\phi + 2\omega t) \tag{2.19}$$

features a dc component. The phase difference ϕ between the resistance modulation and the induced microwave current depends on the geometry of the experiment (relative orientation of B_{eff}, b_1 and the contacts), which is constant in a spin pumping experiment, as well as an the external magnetic field magnitude, since the phase difference changes by π while sweeping over the FMR resonance field. Depending on the magnetic field magnitude independent part of the phase difference, the dc rectification voltage as a function of the magnetic field in general consists of a symmetric Lorentzian line centered at the FMR resonance field and an antisymmetric peak-dip lineshape, also centered at the resonance field. Without angle-dependent measurements, the symmetric contribution from rectification is indistinguishable from a voltage generated by spin pumping.

Chapter 3

Spin Pumping on Yttrium Iron Garnet/Platinum Bilayers

In spin pumping experiments, it is possible to determine the spin mixing conductance $g^{\uparrow\downarrow}$, which governs the effectiveness of spin transport across interfaces and is thus of great importance in such experiments. The magnitude of the spin pumping spin current itself, as well as the magnitudes of spin transfer torque [8–10], the spin Seebeck effect [17–23] and spin Hall magnetoresistance [27, 29], depend on $g^{\uparrow\downarrow}$ [57]. Furthermore, the spin Hall angle θ_{SH} and the spin diffusion length λ_{SD} are critical in the efficiency of spin and charge current conversions, via the (inverse) spin Hall effect. Unfortunately, the experimental determination of one of the parameters $g^{\uparrow\downarrow}$, λ_{SD}, or θ_{SH} in electrically detected spin pumping experiments is usually achieved assuming the magnitudes of the other two values are known. This is due to the fact that the product of all three values features in Eq. (2.14). Due to this problem, many spin pumping and other experiments found in literature quote differing values for $g^{\uparrow\downarrow}$, λ_{SD}, or θ_{SH}, with ranges of $10^{18}\,\mathrm{m}^{-2} < g^{\uparrow\downarrow} < 10^{20}\,\mathrm{m}^{-2}$ in ferromagnet/platinum interfaces [12, 28, 58] and $0.003 < \theta_{\mathrm{SH}} < 0.13$ for the spin Hall angle in platinum [11, 12, 28, 58–61]. The range of λ_{SD} in platinum is the smallest of the three but still spans an order of magnitude, $1\,\mathrm{nm} < \lambda_{\mathrm{SD}} < 14\,\mathrm{nm}$ [12, 28, 57, 60, 62, 63]. Of course all of these values are interconnected, so an underestimation in one parameter usually leads to an overestimation of another value to account for the measured effect amplitude. In this chapter, we put forward a careful analysis of the dependence of the electrically detected spin pumping signal V_{dc} in different yttrium iron garnet (YIG)/Pt bilayers[1] on the thick-

[1] In this and the following sections, we use "ferromagnetic" as a synonym for "exchange coupled", which also includes ferrimagnetic materials. A more rigorous treatment of ferrimagnetic spin pumping will be given in chapter 5.1

nesses of the YIG as well as the Pt layer. We find a consistent set of values for $g^{\uparrow\downarrow}$ of yttrium iron garnet/platinum interfaces, and θ_{SH} and λ_{SD} of platinum. The electrically dependent spin pumping data presented in this chapter has also been used to experimentally show that the spin mixing conductance is common to spin pumping, the spin Seebeck effect, and the spin Hall magnetoresistance [57], and has also been published in the spin pumping study [44]

In the course of this thesis, electrically detected spin pumping experiments were performed on a series of thin film YIG/Pt bilayers. The thickness of the Pt was varied between 1.3 nm and 20 nm, at constant YIG thickness of about 55 nm. In addition the YIG thickness was also varied, between 16 nm and 200 nm. A list of samples used in the following analysis can be found in appendix A.

A direct measurement of $g^{\uparrow\downarrow}$ using FMR linewidth measurements performed as a function of YIG film thickness performed at Regensburg University [44] yields a value for the spin mixing conductance of $g^{\uparrow\downarrow} = 9.7 \times 10^{18}\,\mathrm{m}^{-2}$. The advantage of determining the value of $g^{\uparrow\downarrow}$ using 'damping detected spin pumping' is that the measurement technique does not depend on either θ_{SH} or λ_{SD}. We here describe the corresponding electrically detected spin pumping experiments performed at the WMI, on samples that were fabricated analogously to the samples used in damping detected spin pumping. We then analyze the dependency of the spin pumping voltage measured on a series of samples with differing Pt thicknesses, allowing us to determine the spin diffusion length in platinum. In a last step, we can then extract θ_{SH} in platinum from our measurements.

3.1 Experimental

The samples used in the experiments presented in this thesis were fabricated at the WMI by Sibylle Meyer and Stephan Geprägs. A yttrium iron garnet thin film was deposited by pulsed laser deposition either on single crystal gadolinium gallium garnet or single crystal yttrium aluminum garnet substrates. Subsequently, electron beam evaporation was used to cover the YIG film with a Pt layer. To improve the YIG/Pt interface quality, the vacuum was not broken between the YIG and Pt deposition steps. The finished samples were then diced into pieces of approximately $L = 4\,\mathrm{mm}$ and $w = 1\,\mathrm{mm}$. They were inserted into a Bruker ER4108 TMH microwave cavity resonator mounted between the pole shoes of an electromagnet. The microwave ra-

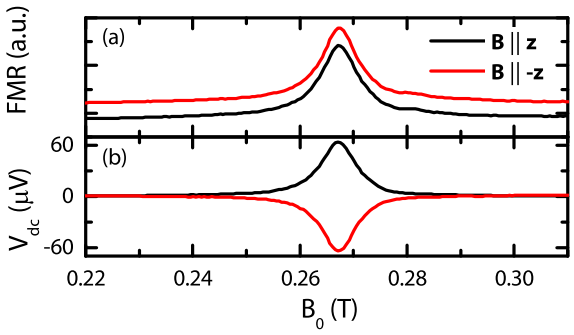

Figure 3.1: Typical FMR and spin pumping data, measured simultaneously. (a) The Lorentzian shaped FMR line is clearly evident at an external magnetic field of $B_0 = 0.267\,\mathrm{T}$. The red and black lines are recorded for opposite magnetic field polarities. (b) The V_{dc} spin pumping data recorded simultaneously with the FMR also show Lorentzian peaks with the same center magnetic field and linewidth as the FMR. However, the reversal of the external magnetic field results in a sign change of V_{dc}.

diation at the cavity frequency of 9.85 GHz is provided by a microwave source. The reflection from the cavity is measured by a homodyne detection circuit designed in the course of this thesis. This circuit allows us to record the FMR signal. Details of the detection circuit can be found in appendix B. To measure the dc voltage V_{dc} we contacted the Pt layer at the short sides of the sample as shown in Fig. 2.3. V_{dc} was then measured using a nanovoltmeter.

In electrically detected spin pumping experiments, the external magnetic field is swept, while simultaneously recording the FMR signal and V_{dc}. Typical data are shown in Fig. 3.1. In Fig. 3.1(a), a Lorentzian shaped FMR line is clearly visible. It does not change upon magnetic field reversal. Figure 3.1(b) shows the spin pumping dc voltage recorded simultaneously. The spin pumping data show the same Lorentzian peaks as the FMR data. Here, the reversal of the external magnetic field causes a sign change in the polarization $\mathbf{s}$ of the pumped spin current and thus leads to a change of the sign of the spin pumping voltage (see Eq. (2.13)). For each of the samples, with different layer thicknesses t_{Pt} and t_{YIG}, spin pumping data are recorded. We fit the V_{dc} curves with a Lorentzian to extract the amplitude of the spin pumping voltage at resonance and the FMR linewidth ΔB. The linewidth can be used to compute the precession cone angle θ of the magnetization according to Eq. (2.6). To this end, the microwave magnetic field b_1 needs to be known. It was calibrated using power dependent linewidth measurements on isotopically pure ^{28}Si. At a microwave input

power of 65 mW incident on the resonant cavity, the magnetic field was found to be $b_1 = 0.032\,\mathrm{mT}$ in the Bruker ER4108 TMH cavity resonator used in our experiments. Although we carefully mounted each sample in the cavity, a small variation in sample placement between the different samples could not be avoided. Thus, the microwave magnetic field b_1 is expected to vary slightly, too.

3.2 Spin Diffusion Length and Spin Hall Angle in Platinum

We now extract the spin diffusion length from the t_{Pt}-dependent spin pumping data. Since all samples used in our experiments have been fabricated within two months and in the same setup, we assume the parameters $g^{\uparrow\downarrow}$ and θ_{SH} to be the same in all the samples for the purpose of this analysis. According to Eq. (2.14),

$$V_{\mathrm{dc}}/(\sin^2(\theta)Rw) = C\lambda_{\mathrm{SD}}\eta(t_{\mathrm{N}},\lambda_{\mathrm{SD}})\tanh(t_{\mathrm{Pt}}/(2\lambda_{\mathrm{SD}}))\,, \tag{3.1}$$

where $C = eg^{\uparrow\downarrow}\theta_{\mathrm{SH}}\frac{\omega}{2\pi}$. The backflow correction factor $\eta(t_{\mathrm{N}},\lambda_{\mathrm{SD}})$ is (see Eq. (2.15))

$$\eta(t_{\mathrm{N}},\lambda_{\mathrm{SD}}) = \left(1 + 2g^{\uparrow\downarrow}\rho\lambda_{\mathrm{SD}}\frac{e^2}{h}\coth\left(\frac{t_{\mathrm{N}}}{\lambda_{\mathrm{SD}}}\right)\right)^{-1}. \tag{3.2}$$

As a function of thickness, $V_{\mathrm{dc}}/(\sin^2(\theta)Rw)$ depends on the thickness of the platinum in first approximation as $\tanh(t_{\mathrm{N}}/2\lambda_{\mathrm{SD}})$. As we will later see, the backflow correction is small ($\eta \approx 1$). In Fig. 3.2, we plot $V_{\mathrm{dc}}/(\sin^2(\theta)Rw)$ as a function of t_{Pt}. For $t_{\mathrm{Pt}} < 3\,\mathrm{nm}$, $V_{\mathrm{dc}}/(\sin^2(\theta)Rw)$ clearly increases. For $t_{\mathrm{Pt}} > 7\,\mathrm{nm}$, the $V_{\mathrm{dc}}/(\sin^2(\theta)Rw)$ data show no clear trend, but scatter around a constant value, due to different sample placement in the cavity. A increase of $V_{\mathrm{dc}}/(\sin^2(\theta)Rw)$ at $t_{\mathrm{N}} < 2\lambda_{\mathrm{SD}}$ and constant $V_{\mathrm{dc}}/(\sin^2(\theta)Rw)$ for $t_{\mathrm{N}} > 2\lambda_{\mathrm{SD}}$ is expected for the $\tanh(t_{\mathrm{N}}/2\lambda_{\mathrm{SD}})$ dependence. To extract λ_{SD} accounting also for backflow correction, we now fit $\eta(t_{\mathrm{N}},\lambda_{\mathrm{SD}})\tanh(t_{\mathrm{N}}/2\lambda_{\mathrm{SD}})$ to $V_{\mathrm{dc}}/(\sin^2(\theta)Rw)$ (red line in Fig. 3.2). We use as constants as the spin mixing conductance $g^{\uparrow\downarrow} = 10^{19}\,\mathrm{m}^{-2}$, as determined by FMR linewidth measurements of Ref. [44] and the mean resistivity of all Pt films, $\rho = 10^{-6}\,\Omega\mathrm{m}$ (the actual values are within a factor of two around this mean value). The fit yields a spin diffusion length in Pt of $\lambda_{\mathrm{SD}} = 1.6 \pm 0.5\,\mathrm{nm}$. There are two studies using dc transport (spin Hall magnetoresistance, see also chapter 6) measurements [28, 64] instead of spin pumping on samples

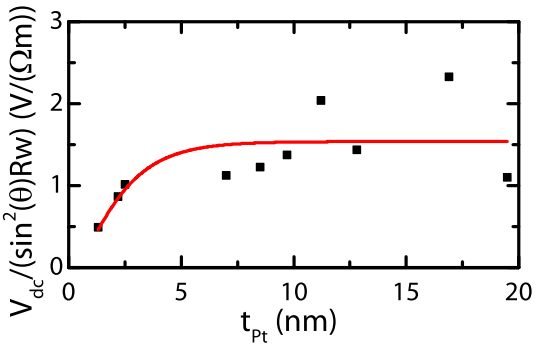

Figure 3.2: . The spin pumping voltage V_{dc} measured in electrically detected spin pumping, divided by the sample dependent values of $\sin^2(\theta)$, the resistance R between contacts, and the width w of the sample, as a function of the Pt thickness. The data are fitted according to Eq. (3.1) to extract the spin diffusion length (see text).

also fabricated at the WMI to determine the λ_{SD}, which find the very similar value of 1.5 nm. This shows the consistency of these measurement methods.

We can now extract the spin Hall angle using Eq. (2.14):

$$\theta_{\mathrm{SH}} = \frac{V_{\mathrm{dc}}}{e g^{\uparrow\downarrow} \lambda_{\mathrm{SD}} \tanh\left(\frac{t_{\mathrm{N}}}{2\lambda_{\mathrm{SD}}}\right) \frac{\omega}{2\pi} R w \sin^2(\theta)}\,, \tag{3.3}$$

Since we have already determined the spin diffusion length to be 1.6 nm, the backflow correction factor can be disregarded even for the sample with the lowest platinum thickness $t_{\mathrm{Pt}} = 1.3\,\mathrm{nm}$. We therefore simply use $\eta = 1$ in the calculation of θ_{SH}. In Fig. 3.3, we show the calculated spin Hall angles according to Eq. (3.3) as a function of the Pt film thickness. Taking an average over the values measured on the different samples, we find that $\theta_{\mathrm{SH}} = 0.06 \pm 0.04$. The dc transport experiments of Refs. [28, 64] find a larger spin Hall angle of $\theta_{\mathrm{SH}} = 0.10 - 0.11$, on the upper end of the range of θ_{SH} determined here. This discrepancy is most likely due to experimental error. In particular, the exact determination of the microwave magnetic field b_1 seems a likely source of error. The introduction of the samples with a magnetic layer and an electrically conducting film as well as the metal leads needed to measure the spin pumping voltage into the microwave resonator alters the electromagnetic mode inside the cavity. This changes the microwave magnetic fields relative to those determined in the calibration experiment and lead to a systematic, sample-independent error. The

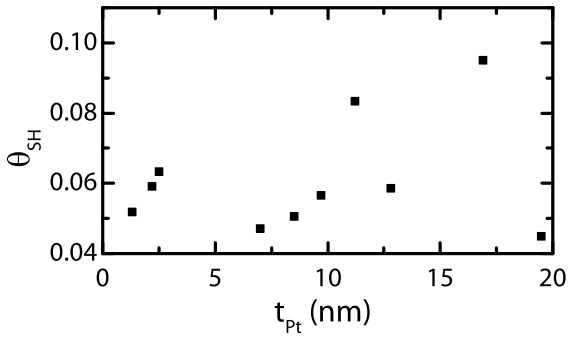

Figure 3.3: The spin Hall angle θ_{SH} as a function of Pt thicknesses calculated according to Eq.(3.3) from the spin pumping voltage in electrically detected spin pumping experiments as a function of the Pt thickness t_{Pt}.

sample independent error does not impact the determination of λ_{SD}, since it does not change the tanh dependency of $V_{\mathrm{dc}}/(\sin^2(\theta)Rw)$. However, the sample independent error leads to an uncertainty in the spin Hall angle θ_{SH}, since it depends on $\sin^2(\theta)^{-2}$. An overestimate of the microwave magnetic field in the resonator thus leads to an underestimate for the spin Hall angle θ_{SH}, which might explain the slight discrepancy between our result and the dc transport results of Refs. [28, 64].

Since the different samples cannot be mounted in exactly the same place, there is also a sample dependent statistical error. In the determination of λ_{SH}, the statistical error leads an error in $V_{\mathrm{dc}}/(\sin^2(\theta)Rw)$, negatively impacting the fit quality of the fit to Eq. (3.1) (See Fig. 3.2). The statistical error also can be easily seen in the scatter of Fig. 3.3 of the values of θ_{SH} for the different samples around the average value.

3.3 Dependence of Spin Pumping on the YIG thickness

The preceding analysis is based on the assumption that spin pumping is a pure interface effect. The spin mixing conductance $g^{\uparrow\downarrow}$, in other words, is thought to be the same, irrespective of the thickness of the ferromagnet or the normal metal thicknesses.

To test this hypothesis, we also performed electrically detected spin pumping experiments on YIG/Pt bilayers with differing YIG thicknesses. The results are shown

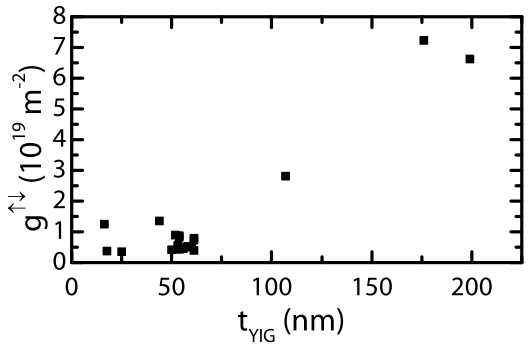

Figure 3.4: The spin mixing conductance calculated from the spin pumping voltage in a variety of YIG/Pt samples as a function of the YIG thickness t_{YIG}.

in Fig. 3.4, where we calculate the spin mixing conductance $g^{\uparrow\downarrow}$ as a function of t_{YIG}, using the values of θ_{SH} and λ_{SD} identified in the previous analysis. The graph can be loosely split in two parts: In the regime of $t_{\mathrm{YIG}} < 60\,\mathrm{nm}$, $g^{\uparrow\downarrow}$ is constant within a factor of 3. This factor of 3 can be explained by considering that the sample fabrication process is not sufficiently optimized to guarantee completely reproducible interfaces. Furthermore, as already explained above, the exact positioning of the sample in the cavity also impacts b_1 and thus V_{dc} and also leads to an uncertainty in $g^{\uparrow\downarrow}$.

However in the regime with $t_{\mathrm{YIG}} > 60\,\mathrm{nm}$, $g^{\uparrow\downarrow}$ increases strongly with t_{YIG}. Experimental uncertainty or fabrication variations are insufficient to explain this strong increase in by about an order of magnitude for $t_{\mathrm{YIG}} = 200\,\mathrm{nm}$. This is surprising, since spin pumping is modeled as a purely interface-related effect, and $g^{\uparrow\downarrow}$ should only depend on the interface quality, not the sample thickness. The strong increase in $g^{\uparrow\downarrow}$ to YIG film thicknesses of 200 nm suggests that this may be an oversimplification. In any case, a more systematic study of the YIG thickness in YIG/Pt bilayers is necessary to explore the precise dependency of $g^{\uparrow\downarrow}$ on t_{YIG}, which would then help find an explanation for the strong increase of $g^{\uparrow\downarrow}$ with YIG thickness.

3.4 Conclusions

We performed electrically detected spin pumping measurements on YIG/Pt bilayer samples with varying layer thicknesses of both the YIG and Pt layers. Combined with damping detected spin pumping data measured at Regensburg University, which fix the spin-mixing conductance $g^{\uparrow\downarrow}$ of YIG/Pt interfaces, the measurements allow

us to determine the spin diffusion length $\lambda_{SD} = 1.6 \pm 0.5\,\text{nm}$ and spin Hall angle $\theta_{SH} = 0.06 \pm 0.04$. The comparison with λ_{SD} and θ_{SH} as determined from dc transport (spin Hall magnetoresistance) measurements shows that both methods can be used in a complementary fashion. In principle, the method of using spin pumping to determine λ_{SD} and θ_{SH} can be applied to other normal metals (e.g. Au, Ta, Pd) as well.

In spin pumping experiments, where the thickness of the YIG layer is varied, we also find that at thicknesses $t_{YIG} > 60\,\text{nm}$, the spin mixing conductance $g^{\uparrow\downarrow}$ is strongly enhanced. The conventional model of spin pumping does not predict this enhancement, necessitating further, systematic YIG thickness dependent spin pumping experiments.

Chapter 4

Spin Pumping in the Strong Coupling Regime

Spin pumping measurements, like those described in Sect. 3 are usually performed in the weak coupling limit, meaning that even in resonance, the magnetic specimen under study only slightly perturbs the properties of the microwave circuitry used. The microwave power driving the resonance is then described in terms of the ac magnetic field b_1, which acts on the magnetization. This implies that the magnetic system and the microwave cavity can be treated as two independent entities. However, if the coupling rate g_{eff}, which describes the transfer of energy between the microwave cavity and the magnetic system, exceeds both the relaxation rates γ_{s} of the magnetic system and κ of the microwave cavity, strong coupling is reached (Fig. 4.1). In the strong coupling limit, the microwave cavity and the magnetic system are no longer independent. Instead, a cavity-ferromagnet superposition state is formed. This is similar to atoms hybridizing to form a molecule. In the frequency and magnetic field dependent spectrum of such a system, the hybridization into the superposition state is accompanied by a characteristic anticrossing of the dispersion lines ω_{c} of the microwave cavity and $\omega_{\text{s}}(B)$ of the magnetic resonance (see Fig. 4.1(b)). The superposition states can be tuned by an applied magnetic field B_0. At the ferromagnetic resonance field B_{FMR}, the frequencies of the cavity and spin system are the same $\omega_{\text{c}} = \omega_{\text{s}}(B_{\text{FMR}})$, and the microwave cavity and magnetic system states are fully hybridized. If B_0 is tuned so that $\omega_{\text{s}}(B_0)$ is different by more than the coupling rate from ω_{c} the cavity and spin system can be excited separately in a pure (cavity or magnetic) state. If this pure state is subsequently transformed into a hybridized state by tuning the magnetic field, the excitation will periodically transform from a 'photon-like' to a

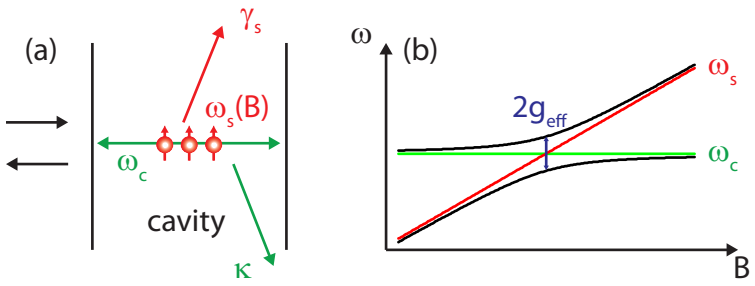

Figure 4.1: Coupling between a spin ensemble and a microwave cavity. (a) An ensemble of spins (red) is coupled to a microwave cavity mode (green). The cavity is driven by an external microwave source. The cavity and spin ensemble relax with relaxation rates κ and γ_s, respectively. If the coupling between the cavity and spin ensemble g_{eff} exceeds both κ and γ_s, strong coupling is reached. (b) In strong coupling, the magnetic field dependent frequency dispersion $\omega_s(B)$ of the spin ensemble and ω_c of the cavity form an anticrossing.

'magnetic-like' state and back [65]. These periodic oscillations are usually observed by measuring time-dependently the microwave signals emitted from the microwave resonator [65–67]. In a spin pumping experiment in which a ferromagnet/normal metal bilayer sample is strongly coupled to a microwave cavity, it should be possible to also measure the excitation state of the ferromagnet through the spin pumping voltage, completing the picture. Pumped spin currents will occur only during those periods of time in which the cavity-ferromagnet superposition state is 'magnetic-like', while in those periods of time in which the superposition state is 'photon-like', there should be no magnetization excitation and thus also no spin current. Taking advantage of the inverse spin Hall effect to monitor the magnitude of the spin current, it is possible to simultaneously but separately study the 'magnetic-like' and the 'photon-like' excitation states in time-resolved spin pumping experiments in the strong coupling limit. In such an approach, the magnetization dynamics viz. the magnetic-like excitations would be detected via the inverse spin Hall signal while the microwave cavity dynamics viz. the photon-like excitations would be observed via the conventional FMR signal. However, before attempting such time-resolved spin pumping experiments in the strong coupling limit, it must first be established that the spin pumping scheme indeed is operational in the strong coupling limit.

Although the magnetic coupling of resonator modes to a spin ensemble is typically small, it has been proposed that the coupling can be enhanced by increasing the

number of polarized spins in the microwave resonator [68]. This concept has been extended to the coupling of a ferromagnet to a resonator [69, 70]. The coupling rate g_{eff} scales as the square root of number of polarized spins N_{s} coupled to the cavity [71–74]

$$g_{\mathrm{eff}} = g_0\sqrt{N_{\mathrm{s}}}\,, \tag{4.1}$$

where g_0 is the coupling rate of a single spin to the microwave cavity. The advantages of ferromagnets are that the spins in a ferromagnet are nearly completely polarized even at room temperature and the number of spins per volume is typically much larger than that in paramagnetic spin ensembles. Varying the volume of the magnetic specimens makes it possible to intentionally work in the weak or the strong coupling regime.

Strong coupling between a resonator and a ferromagnet was realized experimentally at the WMI [74]. In particular, we were able to couple a piece of YIG strongly to a superconducting coplanar waveguide resonator. The evaluation of these data was performed in the course of this thesis. Recently, more experimental and theoretical work was performed on the coupling of YIG to a microwave cavity resonator [65,75,76].

In this section, we explore spin pumping in the strong coupling regime. We first develop a model, which allows us to predict the expected FMR as well as spin pumping signals in the weak and strong coupling limits. We then perform a continous wave spectroscopy experiment, where we simultaneously record both the conventional FMR signal as well as the ISHE-detected dc spin pumping signal of two qualitatively different YIG/Pt bilayer samples in a CW FMR spectrometer: One sample features a 180 nm thick YIG thin film, covered by a thin platinum layer. This sample allows us to experimentally explore the weakly coupled regime. The other YIG/Pt hybrid sample is based on a bulk YIG crystal. The much larger volume of the ferromagnet in this sample enhances the coupling strength relative to the thin film sample, so that we can work in the strongly coupled regime. In contrast to the superconducting coplanar waveguide resonator used in Ref. [74], we use a microwave cavity resonator, enabling experiments at room temperature. Nevertheless, the cavity still has a sufficiently low relaxation rate κ to be suitable for strong coupling experiments.

4.1 Theoretical considerations

We follow the approach laid out in Refs. [77, 78] for calculating the well-established input-output formalism, which describes the microwave signal from the cavity coupled to the spin system. We expand this treatment to derive quantitatively the excitation of a spin system coupled to that cavity, from which we infer the magnitude of the expected spin pumping signal. The Hamiltonian of Eq. (4.2) represents the complete system, consisting of a microwave drive and bath, the cavity, the spin system, as well as their respective interactions:

$$\mathcal{H} = \mathcal{H}_{\text{bath}} + \mathcal{H}_{\text{bc}} + \mathcal{H}_{\text{TC}} \,. \tag{4.2}$$

The first term on the right-hand side of Eq. (4.2),

$$\mathcal{H}_{\text{bath}} = \sum_q \hbar\omega_q \, b_q^\dagger b_q \,, \tag{4.3}$$

describes the bath of microwave photons outside the cavity (in the feedline), including the incoming drive signal. The operators $b_q^\dagger$, b_q are ladder operators for the bath photons. The index q identifies the modes in the bath. ω_q is the frequency belonging to the state q of the feedline photons. The interaction between bath and photons in the cavity is modeled by

$$\mathcal{H}_{\text{bc}} = -\imath\hbar \sum_q \left(f_q a^\dagger b_q - f_q^* b_q^\dagger a \right) \,, \tag{4.4}$$

where $a^\dagger$, a are the raising and lowering operators for the cavity and f_q is the transition matrix element describing the creation of a cavity photon with the simultaneous annihilation of a bath photon. Only the cavity photons can interact with the spin system. The cavity photons, spin excitations and their interaction are governed by the so-called Tavis-Cummings Hamiltonian [72]:

$$\mathcal{H}_{\text{TC}} = \hbar\omega_{\text{c}} a^\dagger a + \hbar\omega_{\text{s}} s^\dagger s + \hbar g_{\text{eff}} (s^\dagger a + a^\dagger s) \,. \tag{4.5}$$

Here, ω_{c} is the cavity resonant frequency and ω_{s} is the FMR frequency of the spin system. $s^\dagger$ and s are the raising and lowering operators for the spin system. In particular, we treat the excitations in the spin system as if they were bosonic. For

large spin ensembles ($N_\mathrm{s} \gg 1$) this approach is known as the Holstein-Primakoff approximation [79]. In detail, a spin ensemble of large scale can be treated as a macrospin with a quantum number S with its corresponding $2S+1$ equally spaced energy levels (when a magnetic field is applied). As long as the number of bosonic excitations does not exceed $2S$, the energy spectrum thus is very similar to that of a harmonic oscillator. It is important to note that $\omega_s = g\mu_\mathrm{B}B/\hbar$, the spacing of the energy levels, is magnetic field dependent.

In the Heisenberg interaction picture, we next derive the equations of motion for a, b_q, and s:

$$\dot{a} = \frac{\imath}{\hbar}[\mathcal{H}, a] = -\imath\omega_\mathrm{c} a - \imath g_\mathrm{eff} s - \sum_q f_q b_q \tag{4.6}$$

$$\dot{b}_q = \frac{\imath}{\hbar}[\mathcal{H}, b_q] = -\imath\omega b_q + f_q^* a \tag{4.7}$$

$$\dot{s} = \frac{\imath}{\hbar}[\mathcal{H}, s] = -\imath\omega_s s - \imath g_\mathrm{eff} a\,. \tag{4.8}$$

We solve Eq. (4.7), in terms of the initial state at t_0 of the bath and in terms of the final state of the bath at t_1:

$$b_q(t) = \mathrm{e}^{-\imath\omega_q(t-t_0)} b_q(t_0) + f_q^* \int_{t_0}^{t} \mathrm{d}\tau\, \mathrm{e}^{-\imath\omega_q(t-\tau)} a(\tau) \tag{4.9}$$

$$b_q(t) = \mathrm{e}^{\imath\omega_q(t_1-t)} b_q(t_1) - f_q^* \int_{t}^{t_1} \mathrm{d}\tau\, \mathrm{e}^{-\imath\omega_q(t-\tau)} a(\tau)\,. \tag{4.10}$$

From Eq. (4.9), it follows that

$$\begin{aligned}\sum_q f_q b_q(t) = &\sum_q f_q \mathrm{e}^{-\imath\omega_q(t-t_0)} b_q(t_0) \\ &+ \int_{t_0}^{t} \mathrm{d}\tau\, \mathrm{e}^{-\imath\omega_\mathrm{c}(t-\tau)} a(\tau) \sum_q |f_q|^2\, \mathrm{e}^{-\imath(\omega_q-\omega_\mathrm{c})(t-\tau)}\,.\end{aligned} \tag{4.11}$$

Via Fermi's Golden Rule, the external coupling constant κ_e between the resonator and the feedline can be related to the matrix element f_q:

$$2\kappa_\mathrm{e}(\omega_\mathrm{c}) = 2\pi \sum_q |f_q|^2\, \rho(\omega_q)\,, \tag{4.12}$$

where $\rho(\omega_q)$ is the density of states. In the case of a cavity resonator with only a single mode,

$$\rho(\omega_q) = \delta(\omega_\mathrm{c} - \omega_q)\,. \tag{4.13}$$

Note that the dimension of $\rho(\omega_q)$ is seconds. Assuming the transition probability and the matrix elements are constant with respect to frequency and time (Markov approximation), a Fourier transform of Eq. (4.12) yields:

$$2\kappa_\mathrm{e}\delta(t-\tau) = \sum_q |f_q|^2\, \mathrm{e}^{-\imath(\omega_q-\omega_\mathrm{c})(t-\tau)}\,. \tag{4.14}$$

Inserting Eq. (4.14) into Eq. (4.11), we find:

$$\sum_q f_q b_q = \sqrt{2\kappa_\mathrm{e}}\, b_\mathrm{in} + \kappa_\mathrm{e} a\,. \tag{4.15}$$

where we have defined the 'input mode'

$$b_\mathrm{in}(t) = \frac{1}{\sqrt{2\pi\rho}} \sum_q \mathrm{e}^{-\imath\omega_q(t-t_0)} b_q(t_0)\,. \tag{4.16}$$

$b_\mathrm{in}(t)$ is can be anticipated as a microwave field moving toward the cavity in the feedline.

By using the solution of Eq. (4.10) instead of Eq. (4.9), we can analogously derive

$$\sum_q f_q b_q = \sqrt{2\kappa_\mathrm{e}}\, b_\mathrm{out} + \kappa_\mathrm{e} a\,. \tag{4.17}$$

Here,

$$b_\mathrm{out}(t) = \frac{1}{\sqrt{2\pi\rho}} \sum_q \mathrm{e}^{\imath\omega_q(t_1-t)} b_q(t_1) \tag{4.18}$$

is the 'output' mode, interpreted as the field moving away from the cavity in the feedline. Equations (4.17) and (4.15) together yield:

$$b_\mathrm{out} = b_\mathrm{in} + \sqrt{2\kappa_\mathrm{e}}\, a\,. \tag{4.19}$$

Inserting Eq. (4.15) into the equations of motion Eqs. (4.6) yields:

$$\dot{a} = -\imath\omega_\mathrm{c} a - \kappa_\mathrm{e} a - \imath g_\mathrm{eff} s - \sqrt{2\kappa_\mathrm{e}}\, b_\mathrm{in} \tag{4.20}$$

As we can see, from a the point of view of the cavity, the interaction with the bath leads to a linear damping term (second term in Eq. (4.20)). In a real cavity resonator, excitation can be lost by interaction with bath, or with the spin system. It can also be lost due to internal resonator damping which is not included in the Hamiltonian of Eq. (4.2). At this point, we account for this internal damping mechanism by introducing $\kappa_\mathrm{c} a$ to the right side of Eq. (4.20), where κ_c is the internal relaxation rate of the cavity:

$$\dot{a} = -\imath\omega_\mathrm{c} a - (\kappa_\mathrm{e} + \kappa_\mathrm{c})a - \imath g_\mathrm{eff} s - \sqrt{2\kappa_\mathrm{e}}\, b_\mathrm{in}\,. \tag{4.21}$$

The value $\kappa = \kappa_\mathrm{e} + \kappa_\mathrm{c}$ is the total relaxation rate of the cavity. In the same fashion, a relaxation term for the spin system is added. The equation of motion for s is therefore:

$$\dot{s} = -\imath\omega_\mathrm{s} s - \gamma_\mathrm{s} s - \imath g_\mathrm{eff} a\,. \tag{4.22}$$

With Eqs. (4.21) and (4.22), we calculate the states of the cavity and spin system in frequency space, as a function of the input field b_in. With

$$a(t) = \frac{1}{\sqrt{2\pi}} \sum_q \mathrm{e}^{-\imath\omega_q t} a(\omega) \tag{4.23}$$

$$s(t) = \frac{1}{\sqrt{2\pi}} \sum_q \mathrm{e}^{-\imath\omega_q t} s(\omega) \tag{4.24}$$

$$b_\mathrm{in}(t) = \frac{1}{\sqrt{2\pi}} \sum_q \mathrm{e}^{-\imath\omega_q t} \underbrace{\frac{1}{\sqrt{\rho}} \mathrm{e}^{\imath\omega_q t_0} b_q(t_0)}_{=b_\mathrm{in}(\omega)} \tag{4.25}$$

$$b_\mathrm{out}(t) = \frac{1}{\sqrt{2\pi}} \sum_q \mathrm{e}^{-\imath\omega_q t} \underbrace{\frac{1}{\sqrt{\rho}} \mathrm{e}^{\imath\omega_q t_1} b_q(t_1)}_{=b_\mathrm{out}(\omega)}\,. \tag{4.26}$$

we find in steady state:

$$a(\omega) = \frac{\sqrt{2\kappa_\mathrm{e}}}{\imath(\omega - \omega_\mathrm{c}) - (\kappa_c + \kappa_e) + \frac{g_\mathrm{eff}^2}{\imath(\omega - \omega_\mathrm{s}) - \gamma_\mathrm{s}}} b_\mathrm{in}(\omega)\,, \tag{4.27}$$

and

$$s(\omega) = \frac{\imath g_\mathrm{eff}\sqrt{2\kappa_e}}{(\imath(\omega - \omega_\mathrm{c}) - (\kappa_c + \kappa_e))(\imath(\omega - \omega_\mathrm{s}) - \gamma_\mathrm{s}) + g_\mathrm{eff}^2} b_\mathrm{in}(\omega)\,. \tag{4.28}$$

Using Eq. (4.27) together with Eq. (4.19), we derive the power reflected at the microwave cavity relative to the power incident on the cavity,

$$\begin{aligned} |S_{11}(\omega)|^2 &= \frac{b^\dagger_{\mathrm{out}}(\omega) b_{\mathrm{out}}(\omega)}{b^\dagger_{\mathrm{in}}(\omega) b_{\mathrm{in}}(\omega)} \\ &= \left| 1 + \frac{2\kappa_{\mathrm{e}}}{\imath(\omega - \omega_{\mathrm{c}}) - (\kappa_c + \kappa_e) + \frac{g^2_{\mathrm{eff}}}{\imath(\omega - \omega_{\mathrm{s}}) - \gamma_{\mathrm{s}}}} \right|^2 , \end{aligned} \tag{4.29}$$

which is known as the input-output formalism [78]. For spin pumping, we are interested in the number of magnetic excitations

$$\begin{aligned} N_{\mathrm{ex,s}}(\omega) &= s^\dagger s \\ &= \frac{P_{\mathrm{in}}}{\hbar\omega} \left| \frac{\imath g_{\mathrm{eff}} \sqrt{2\kappa_{\mathrm{e}}}}{(\imath(\omega - \omega_{\mathrm{s}}) - \gamma_{\mathrm{s}})(\imath(\omega - \omega_{\mathrm{c}}) - (\kappa_c + \kappa_e)) + g^2_{\mathrm{eff}}} \right|^2 , \end{aligned} \tag{4.30}$$

where we have used

$$P_{\mathrm{in}} = \hbar\omega b^\dagger_{\mathrm{in}}(\omega) b_{\mathrm{in}}(\omega) \, . \tag{4.31}$$

As laid out in Sect. 2.2, the amount of angular momentum transported from the ferromagnet to the normal metal in spin pumping is proportional to $\sin^2(\theta)$, where θ is the magnetization precession cone angle (see Eq. (2.11)). Note that $\sin^2(\theta)$ is only proportional to the dc damping torque and thus the spin current in the classical limit, when $N_{\mathrm{s}} \gg 1$ (see also chapter 5.1). We now relate the number of excitations in the spin system to the precession cone angle. In a single domain ferromagnet, the spin behaves just like a one large spin, with $S = N_{\mathrm{s}}$, where S is the spin quantum number. The precession cone angle of such a system is given by (see Fig. 4.2)

$$\begin{aligned} \cos(\theta) &= \frac{\langle S_z \rangle}{\langle S \rangle} \\ &= \frac{\hbar(N_{\mathrm{s}} - N_{\mathrm{ex,s}})}{\hbar\sqrt{S(S+1)}} , \end{aligned} \tag{4.32}$$

where $\langle S \rangle$ is the expectation value of the total angular momentum of the spin system and $\langle S_z \rangle$ is the expectation value of its z-component. M is the magnetic quantum number $-S \leq M \leq S$. For $N_{\mathrm{s}} \gg 1$ and $N_{\mathrm{ex,s}} \ll N_{\mathrm{s}}$ Eq. (4.32) simplifies to:

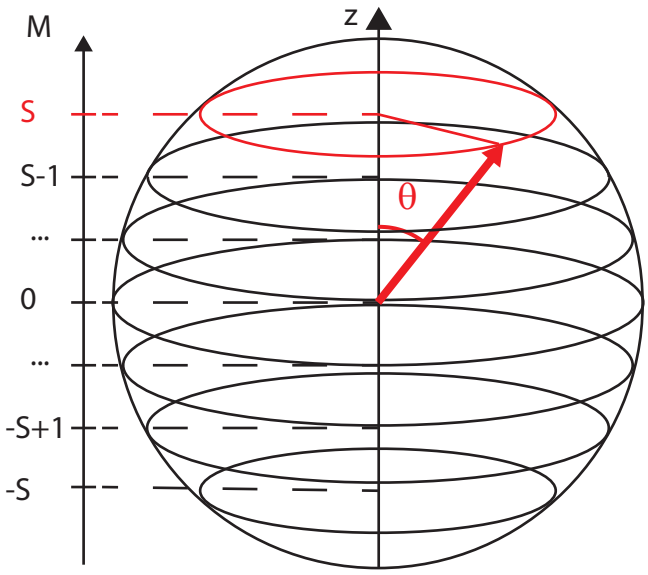

Figure 4.2: Trajectory of a spin system with in a magnetic field in z direction (quantization axis). The precession cone angle θ can be inferred from the expectation value $\hbar\sqrt{S(S+1)}$ of the total angular momentum S (sphere) and its z-component S_z, $\hbar M$, where M is the magnetic quantum number. In a ferromagnet, $S \gg 1$ and there are $2S+1$ quasi-continuous states.

$$\theta = \sqrt{\frac{2N_{\mathrm{ex,s}}}{N_{\mathrm{s}}}}\,. \tag{4.33}$$

This means that the spin pumping voltage generated is directly proportional to $N_{\mathrm{ex,s}}$.

Since all variables determining $N_{\mathrm{ex,s}}$ are accessible in a frequency and magnetic field dependent FMR experiment (see below), Eq. (4.33) can in principle also be used to calibrate the microwave magnetic field b_1 in the resonator in the presence of a sample, via $\theta = b_1/\Delta B$ (See Chapter 2.2). This is otherwise difficult, since any ac magnetic field measurement device that is inserted into the resonator will also perturb the cavity resonance mode.

Using Eqs. (2.14), and (4.33) we calculate the spin pumping voltage as

$$V_{\mathrm{sp}}(\omega,\omega_{\mathrm{s}}) = 2eg^{\uparrow\downarrow}\theta_{\mathrm{SH}}\lambda_{\mathrm{SD}}\tanh\left(\frac{t_{\mathrm{N}}}{2\lambda_{\mathrm{SD}}}\right)\frac{\omega}{2\pi}Rw\frac{N_{\mathrm{ex,s}}(\omega,\omega_{\mathrm{s}})}{N_{\mathrm{s}}}\,, \tag{4.34}$$

where the resonance frequency of the spin system ω_{s} is a function of the external magnetic field B and internal (anisotropy) magnetic fields. If the external magnetic fields are larger than the internal magnetic fields, ω_{s} is approximately linear in the

external magnetic field

$$\omega_s = \omega_c + \gamma(B - B_{FMR}) , \tag{4.35}$$

where B_{FMR} is the FMR resonance field at the cavity frequency ω_c and γ is the gyromagnetic ratio.

Summing up, the input-output formalism together with Eq. (4.30) allows us to calculate the cavity-like and the magnetic-like (spin pumping) signal of the coupled spin-cavity system, in both the weak and the strong coupling limit, as a function of frequency and applied magnetic field.

4.1.1 Weak Coupling

In this section we will simulate the microwave reflection $|S_{11}(\omega)|^2$ as well as the spin pumping voltage, using Eqs. (4.29) and (4.34) for a spin system weakly coupled to a microwave cavity. The simulation is done using parameters which will be as similar as possible to the parameters of the experiment described below in section 4.2.1, performed on a YIG(180 nm)/Pt(7 nm) bilayer sample. This will help us compare the model introduced here to experiment. In chapter 3, we have already determined the parameters relevant for spin pumping in that sample, $g^{\uparrow\downarrow}$, λ_{SD}, and θ_{SH}. All other necessary parameters are derived from the experiment described in section 4.2.1. This ensures that the results of the calculation done in this section can easily be compared to the experimental data presented below. The parameters use are compiled in Tab. 4.1.

Figure 4.3(a) shows $|S_{11}(\omega)|^2$, i.e. a measure for the microwave power reflected from the cavity, in a false color plot. The (nearly magnetic-field independent) cavity absorption appears at ω_c as a horizontal line, with a half width half maximum (HWHM) linewidth of $(\kappa_c + \kappa_e)$. The impact of the spin system on the cavity dispersion is not discernible in the false color representation of Fig. 4.3(a), since the spin system only weakly perturbs the cavity in this limit. However, upon plotting the change in resonance frequency from the unperturbed cavity frequency $\Delta\omega$ in Fig. 4.3(c) and change in cavity linewidth $\Delta\kappa$ in Fig. 4.3(d), it becomes clear that the spin system indeed slightly alters the cavity properties. The resonant frequency of the coupled system changes slightly as a function of magnetic field, increasing and then decreasing. The linewidth of the system peaks at B_{FMR}, which is marked by a blue line in Fig. 4.3(c,d). Both changes are only in the range of a few tens of kHz, which is small compared to

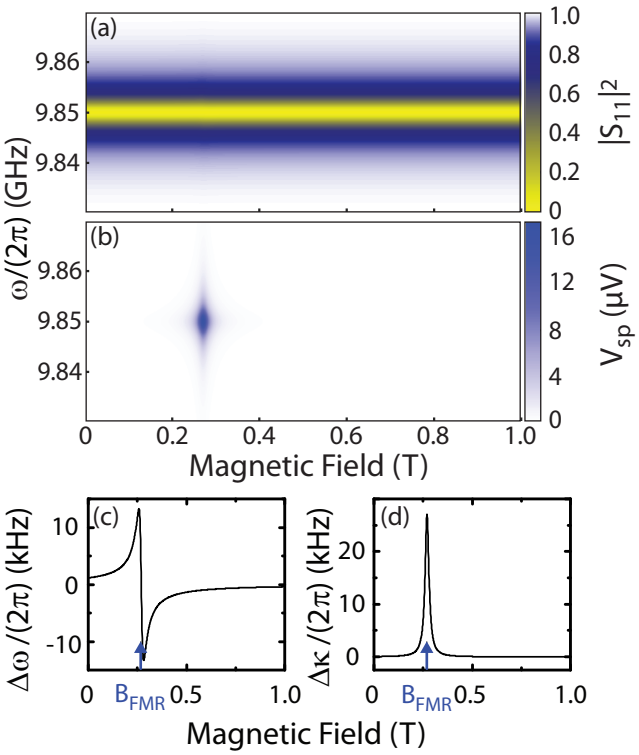

Figure 4.3: Simulation of a frequency and magnetic field dependent spin pumping experiment using a magnetic thin film sample. The relatively low number of spins in the magnetic thin film results to a weak coupling between cavity and spin system. The parameters used in the calculation are listed in Tab. 4.1. (a) Microwave reflection $|S_{11}|^2$ calculated using Eq. (4.29). $|S_{11}|^2$ is shown in a false color plot as a function of external magnetic field and microwave frequency. (b) Spin pumping voltage a function of magnetic field and frequency of the same system calculated using Eq. (4.34). (c) Change of frequency $\Delta\omega$ from the unperturbed cavity mode as a function of external magnetic field. (d) Change of the cavity resonance frequency $\Delta\omega$ as a function of the applied magnetic field.

the FMR linewidth (MHz) and the FMR resonant frequencies (GHz). However, the change of the cavity frequency and the change in cavity quality factor still result in a change in amplitude of the reflected microwave signal. This is the quantity studied in conventional, cavity-based, fixed frequency CW magnetic resonance experiments [80].

The spin pumping voltage V_{sp} is calculated from Eq. (4.34) and is depicted as a function of magnetic field and microwave frequency in a false color plot in Fig. 4.3(b). Clearly, the spin system is only excited in ferromagnetic resonance, where spin pumping appears as a nearly vertical line at $B_{\mathrm{FMR}} = 0.27\,\mathrm{T}$. The magnitude of the spin pumping voltage is strongest at the cavity frequency ω_{c} and weakens with increasing frequency detuning, due to the filtering of the microwave radiation by the cavity. The maximum spin pumping voltage is $V_{\mathrm{sp,max}} = 17\,\mu\mathrm{V}$ at the FMR resonance field B_{FMR} and at the cavity frequency ω_{c}. Figures 4.3(a) and (b) show that in the weakly coupled case, the microwave reflection and the spin pumping voltage are complementary. The former is a measure of the photon-like excitation in the cavity, while the latter is a measure of the excitation of the spin system.

Table 4.1: Parameters used in the calculations shown in Figs. 4.3 (weak coupling) and 4.4 (strong coupling)

	weak coupling	strong coupling
$\omega_{\mathrm{c}}/(2\pi)$ (GHz)	9.85	9.85
$\kappa_{\mathrm{e}}/(2\pi)$ (MHz)	1.3	1.15
$\kappa_{\mathrm{c}}/(2\pi)$ (MHz)	1.3	1.15
$g_{\mathrm{eff}}/(2\pi)$ (MHz)	3	150
$\gamma_{\mathrm{s}}/(2\pi)$ (MHz)	336	100
B_{FMR} (T)	0.27	0.35
$g^{\uparrow\downarrow}$ ($10^{19}\,\mathrm{m}^{-2}$)	7	1
θ_{SH}	0.06	0.06
λ_{SD} (nm)	1.6	1.6
R (Ω)	180	600
w (mm)	0.8	1
$t_{\mathrm{N}}(nm)$	7	3
N_{s}	10^{16}	10^{20}
P (mW)	77.5	77.5

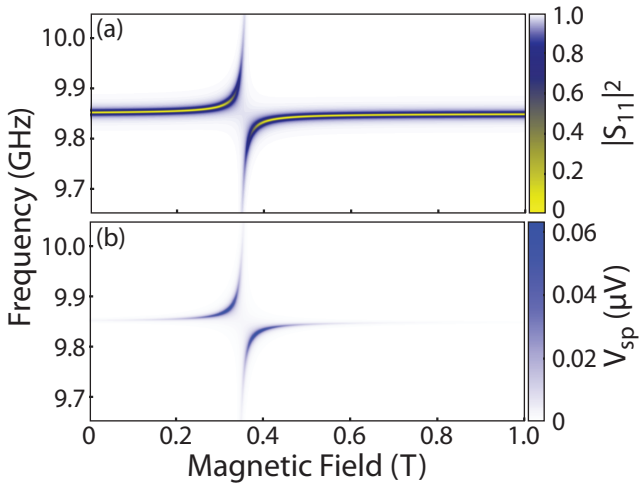

Figure 4.4: (a) Calculated microwave reflection $|S_{11}|^2$ of a strongly coupled microwave cavity - spin system according to Eq. (4.29). The parameters used in the calculation are given in Tab. 4.1. $|S_{11}|^2$ is shown in a false color plot as a function of external magnetic field and microwave frequency. (b) Calculated spin pumping voltage V_{sp} of the same system according to Eq. (4.34).

4.1.2 Strong Coupling

The separate treatment of cavity and spin system is no longer applicable in the strongly coupled case. A simulation of a strongly coupled system is presented in Fig. 4.4, using the corresponding parameters from Tab. 4.1. Again, the parameters are chosen to model the experiment presented below. As evident from the microwave reflection $|S_{11}(\omega)|^2$ in Fig. 4.4(a), the cavity absorption is no longer continuous as a function of the magnetic field, but interrupted by a clear anticrossing in the field-frequency region where the cavity and spin system dispersions would intersect. The two resonance frequencies of the coupled cavity-spin system

$$\omega_{1,2} = \omega_{\mathrm{c}} + \frac{\Delta}{2} \pm \frac{1}{2}\sqrt{\Delta^2 + 4\,g_{\mathrm{eff}}^2} \tag{4.36}$$

can be found by diagonalizing the Hamiltonian of Eq. (4.5). Here, $\Delta = \gamma(B - B_{\mathrm{FMR}})$. The frequency splitting of the upper and lower branches of the dispersion at the FMR field is $2g_{\mathrm{eff}}$. The $|S_{11}(\omega)|^2$ signal intensity again diminishes farther away from the cavity frequency due to the filtering of the cavity.

In the spin pumping voltage amplitude V_{sp} shown in Fig. 4.4(b), the anticrossing of the dispersions is also visible. The magnitude of the spin pumping voltage is

however very small, only reaching about 60 nV. This value is reached on the point of FMR resonance dispersion of the coupled system which is closest to $\omega_c = \omega_s$. The magnitude of the spin excitation is decreasing upon detuning from resonance, both on the magnetic field and the frequency axes. Detuning of the frequency results in a decrease of photon number in the cavity and thus in a decreased excitation of the spin system. A detuning in the field makes the coupled spin-cavity system more cavity-like, also resulting in a reduced pumped spin current. The maximum spin pumping voltage $V_{sp,max} = 60\,\text{nV}$ which can be achieved is smaller than in the weakly coupled case ($V_{sp,max} = 17\,\mu\text{V}$) by about two orders of magnitude, with otherwise comparable parameters. An intuitive explanation is that the microwave magnetic field in the cavity excites a greater number of spins in larger pieces of ferromagnet. Since only the spins at ferromagnet/normal metal the interface contribute to the pumped spin current [33], much of the excitation in the spin system does not generate any pumped spin current. The excitation of the spins far from the interface is 'lost'. This is true even though the coupling of the microwave radiation to the spin system is more efficient in large spin systems. More quantitatively, we can calculate the maximum spin pumping voltage as a function of N_s by inserting Eq. (4.30) into Eq. (4.34), and evaluating this expression at the frequency and magnetic field where V_{sp} is maximum. We find

$$V_{sp} \propto \frac{2}{(g_0^2 N_s + \gamma_s(\kappa_e + \kappa_c))^2} \tag{4.37}$$

for $\gamma_s(\kappa_e + \kappa_c) \geq g_{eff}^2$ and

$$V_{sp} \propto \frac{1}{2g_0^2 N_s \gamma_s(\kappa_e + \kappa_c)} \tag{4.38}$$

for $\gamma_s(\kappa_e + \kappa_c) < g_{eff}^2$. Except when g_{eff}^2 is considerably smaller than $\gamma_s(\kappa_e + \kappa_c)$, an increase in ferromagnet size, and therefore N_s and g_{eff}, leads to a decrease in maximum observable spin pumping voltage. This is illustrated in Fig. 4.5, where the maximum spin pumping voltage $V_{sp,max}$ (at the optimal frequency and magnetic field) is shown as a function of g_{eff}^2.

To sum up, in the strongly coupled case the cavity and spin excitations are no longer independent of each other. Instead, in the region of the anticrossing both the cavity and the spin system are simultaneously excited by the incoming microwave radiation. Spin pumping is predicted to be much less efficient in bulk samples than in thin film samples.

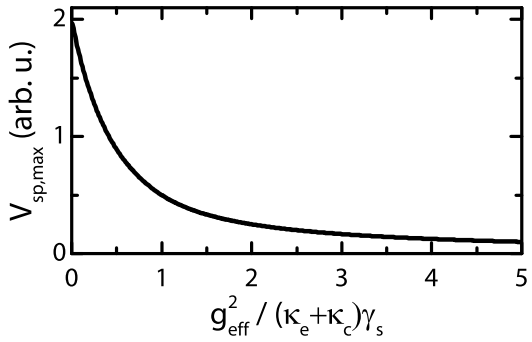

Figure 4.5: Maximum measurable spin pumping voltage $V_{\mathrm{sp,max}}$ as a function of the square of the effective coupling rate g_{eff}^2, which is proportional to the number of spins N_{s} in the ferromagnet.

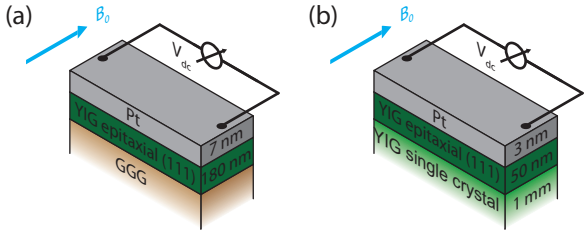

Figure 4.6: (a) Sample #1: A 180 nm thick, (111)-oriented yttrium iron garnet (YIG) thin film, epitaxially grown on a gadolinium gallium garnet (GGG) substrate. A 7 nm Pt film is evaporated in situ on top of the YIG thin film. (b) sample #2: A 50 nm thick, (111)-oriented YIG thin film, epitaxially grown on a 1 mm thick YIG single crystaline substrate. A 3 nm Pt film is evaporated in situ on top of the YIG thin film. The external magnetic field is applied in the film plane and the spin pumping voltage V_{dc} is measured perpendicularly to the magnetic field.

4.2 Experimental Results

We now compare our model calculations to experiment. To that end, we measure the microwave reflection as well as the spin pumping voltage on two different samples.

Sample # 1 is shown schematically in Fig. 4.6(a): it consists of a 180 nm thick YIG film deposited on a (111)-oriented single-crystalline gadolinum gallium garnet (GGG) substrate using laser-MBE [81]. After the YIG growth, the sample was transferred to an electron beam evaporation chamber without breaking the vacuum and a Pt film with a thickness of 7 nm was deposited onto the YIG, as described in more detail in Ref. [28]. After removal from the deposition system, the sample was diced into

rectangular pieces with lateral dimensions of $0.8 \times 3\,\mathrm{mm}^2$. For a spin density in YIG of $\rho_{\mathrm{s,YIG}} = 2 \times 10^{22}\,\mathrm{cm}^{-3}$ [82], the number of spins present in such a sample is $N_{\mathrm{s},1} \approx 10^{16}$.

Sample # 2 is shown schematically in Fig. 4.6(b): it consists of a 50 nm thick YIG film grown by laser-MBE on a 1 mm thick, (111) oriented bulk YIG single crystal. Subsequently, we evaporated a 3 nm Pt film on top, again without breaking the vacuum. This homoepitaxy step is used in sample preparation, because it guarantees that the YIG/Pt interface is clean, thereby enhancing spin pumping over the interface. Sample # 2 was diced to lateral dimensions of $1 \times 5\,\mathrm{mm}^2$, which corresponds to a number of spins of $N_{\mathrm{s},2} \approx 10^{20}$, such that $N_{\mathrm{s},2} \approx 10^4 \times N_{\mathrm{s},1}$. This means that the coupling of the cavity mode to sample # 2 is expected to be enhanced by a factor of $100 = \sqrt{10^4}$ relative to sample # 1 (see Eq. (4.1)).

The FMR and spin pumping measurements were performed in a CW cavity based magnetic resonance spectrometer, using a Bruker ER4108 TMH microwave cavity operating at $\omega_{\mathrm{c}}/(2\pi) = 9.85\,\mathrm{GHz}$. Using an iris at the input port of the microwave cavity, the external coupling rate κ_{e} was tuned to be the same as κ_{c} (crtical coupling). A magnetic field of up to $\pm 1\,\mathrm{T}$ was applied via an electromagnet in the plane of the Pt films. The FMR and spin pumping data were recorded with an Agilent N5242A vector network analyzer (VNA) emitting microwave radiation at a power level of $P_{\mathrm{in}} = 20\,\mathrm{dBm}$. Direct current leads were connected to the sample perpendicular to the applied magnetic field (See Fig. 4.6). The spin pumping dc voltage induced by the excitation of the spin system was amplified using a Stanford Research SR 560 differential preamplifier and then recorded using the auxiliary input port of the VNA. In this way it is possible to simultaneously measure the microwave reflection S_{11} and the dc voltage generated by the inverse spin Hall effect. The data were acquired as a series of microwave frequency sweeps at each external magnetic field B, i.e. the magnetic field was set to a given constant value and $S_{11}(\omega, B)$ and $V_{\mathrm{dc}}(\omega, B)$ were recorded. Subsequently the magnetic field was set to the next value. The power deposited into the microwave cavity is ideally proportional to the quantity $P_{\mathrm{in}}(1 - |S_{11}|^2)$. However, losses also occur in the feedline. Since there were no calibration standards available for the Bruker cavity/waveguide, only uncalibrated measurements were possible, meaning that the characteristics of the used microwave feedline is visible in the recorded spectra.

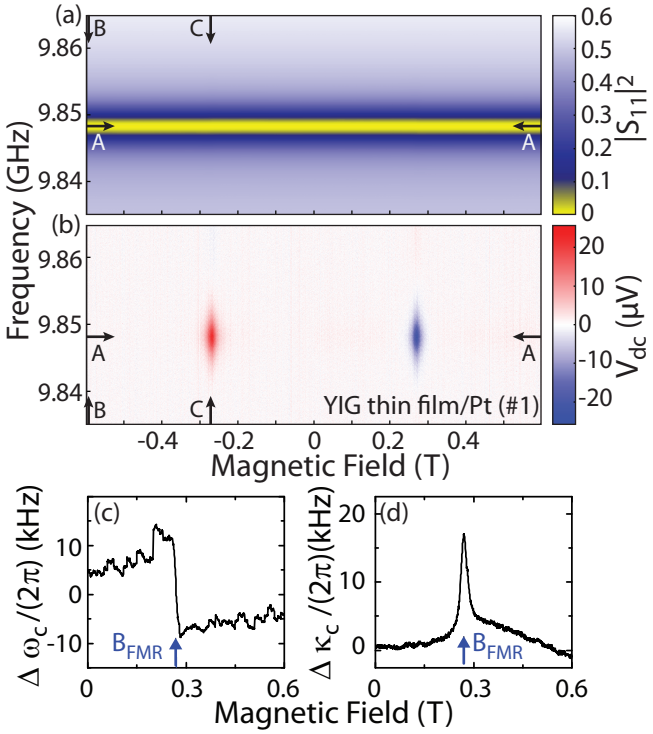

Figure 4.7: (a) Measured microwave reflection $|S_{11}|^2$ of the microwave cavity thin film sample #1 in the weak coupling limit. $|S_{11}|^2$ is shown in a false color plot as a function of external magnetic field and microwave frequency. (b) Measured spin pumping voltage V_{dc} of sample #1, in a false color plot. (c) Change of the cavity resonance frequency ω_c as a function of applied magnetic field. ω_c is extracted from the data by fitting a Lorentzian to each frequency cut.(d) Change of the frequency linewidth κ_c of the cavity mode as a function of external magnetic field extracted with the same fit. The arrows A-A, B-B, and C-C indicate the cuts shown in Fig. 4.8.

4.2.1 180 nm YIG/7 nm Pt bilayer

In Figure 4.7(a), the microwave reflection $|S_{11}|^2$ of sample #1 is presented as a function of frequency and magnetic field strength in a false color plot. The most prominent feature in the data of Fig. 4.7(a) is the absorption line of the cavity at a frequency of $\omega_c/(2\pi) = 9.848\,\text{GHz}$. The cavity resonance frequency for each applied magnetic field value is extracted by performing a Lorentzian fit along the frequency axis. Fig. 4.7(c) shows $\Delta\omega_c = \omega_c(B) - \omega_c(B = 0)$ thus obtained. The resonance frequency changes slightly when the applied magnetic field is varied, as expected from our model calculations (Fig. 4.3(a)). More precisely, the resonance frequency changes

by less than 20 kHz, which is much less than the half width half maximum cavity linewidth $\kappa_/(2\pi) = 2.6\,\mathrm{MHz}$. The cavity linewidth also changes slightly, but systematically as a function of the magnetic field strength, as can be seen in Fig. 4.7(d). The linewidth is maximum at the resonance field, $B_{\mathrm{FMR}} = \pm 0.27\,\mathrm{T}$, indicated by blue arrows in Fig. 4.7(c,d). The change in linewidth is also small compared to the absolute linewidth of the resonance. Taken together, both ω_c and κ_c show the behavior typical for the weak coupling limit. The evolution of ω_c and κ with the magnetic field strength allows us to quantify the effective coupling, by fitting them to [83, 84]:

$$\omega_\mathrm{c} = \omega_{\mathrm{c},0} - g_\mathrm{eff}^2 \Delta/(\Delta^2 + \gamma_\mathrm{s}^2) \tag{4.39}$$

$$\kappa = \kappa_0 + g_\mathrm{eff}^2 \gamma_\mathrm{s}/(\Delta^2 + \gamma_\mathrm{s}^2)\,, \tag{4.40}$$

where $\omega_{\mathrm{c},0}$ and κ_0 are the frequency and relaxation rate of the microwave cavity at $B_0 = 0$. $\Delta = \gamma_\mathrm{YIG}(B - B_\mathrm{FMR})$ is the detuning and $\gamma_\mathrm{YIG} = 1.76 \times 10^{11}\,\mathrm{Ts}^{-1}$ is the gyromagnetic ratio of YIG. In this way we estimate the effective coupling of the spin system to the cavity to be $g_\mathrm{eff} = 3\,\mathrm{MHz}$. We also extract the damping constant of the spin system, $\gamma_\mathrm{s} = 360\,\mathrm{MHz}$. In the recorded spectra, the microwave reflection $|S_{11}|^2$, far away from the cavity resonance frequency ideally should be 1 (total reflection). In our recorded spectra, the maximum reflection $|S_{11,\mathrm{max}}|^2 = 0.6$. This is the effect of the uncalibrated feedline, allowing us to quantify the losses in the cable. The loss ratio of the feedline is $L = \sqrt{|S_{11,\mathrm{max}}|^2} = 0.78$. The square root is due to the fact that the microwave passes the feedline twice in a reflection experiment. This allows us to compute the power incident at the resonator as $P_\mathrm{in} L = 78\,\mathrm{mW}$.

Figure 4.7(b) depicts the dc voltage V_dc measured simultaneously with S_{11} in false color. A finite voltage is observed only around the FMR resonance fields. For negative magnetic fields the sign of the dc voltage is opposite to the one for positive magnetic fields. This is the behavior expected for an ISHE voltage induced by spin pumping: the ISHE voltage is driven by the spin dynamics and thus appears only upon ferromagnetic resonance. With the inversion of the magnetic field, which leads to an inversion of the polarisation of the spin current, the ISHE Voltage changes sign. Like the microwave absorption data, the experimental spin pumping data are fully consistent with the model calculations shown in Fig. 4.3.

For a more quantitative comparison, the FMR and the spin pumping signals are shown in Fig. 4.8(a) as a function of magnetic field at a constant microwave frequency $\omega_\mathrm{c}/(2\pi) = 9.85\,\mathrm{GHz}$ indicated with arrows 'A-A' in Fig. 4.7(a,b). These spectra corre-

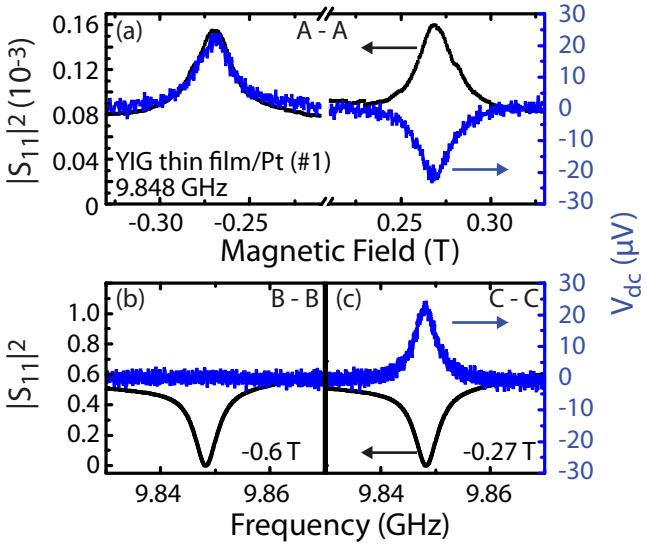

Figure 4.8: Measured microwave reflection $|S_{11}|^2$ and spin pumping voltage V_{dc} in sample # 1: (a) Magnetic field-dependent microwave reflection and spin pumping voltage at constant frequency of $\omega_{\mathrm{c}}/(2\pi) = 9.848\,\mathrm{GHz}$. The lineshape of V_{dc} is the same as for the microwave reflection signal. The sign of V_{dc} changes when the appied magnetic field is inverted. (b),(c) Frequency-dependent microwave reflection and spin pumping voltage at constant magnetic fields. At an off-resonant magnetic field (panel (b)), no spin pumping voltage is measured. At B_{FMR} (panel (c)), the spin pumping signal is clearly visible.

spond to the ones taken in "conventional", fixed-frequency, CW magnetic resonance spectrometers and exhibit the same features [12, 85]: $|S_{11}|^2$, the a measure of the FMR intensity, exhibits a peak in resonance. The spin pumping voltage also shows an extremum with identical line shape at the same resonance fields as the FMR, but inverts sign under magnetic field inversion. Because the cavity and spins are only weakly coupled, the FMR magnetic field linewidth of $\Delta B_{\mathrm{FMR}} = 0.012\,\mathrm{T}$ reflects the damping of the YIG spin system alone (the cavity quality is not magnetic field-dependent). Under the assumption of weak coupling, we can calculate the relaxation rate γ_{s} of the spin simply as $\gamma_{\mathrm{s}}/(2\pi) = \gamma \Delta B_{\mathrm{FMR}} = 336\,\mathrm{MHz}$. This value is consistent with the one determined by a fit of the linewidth to Eq. (4.40) above, again verifying the assumption of weak coupling. It is also much larger than the coupling of only 3 MHz between the cavity and spin system. Under the assumption that the damping of the spin system is exclusively viscous (Gilbert-like), one obtains a Gilbert damping parameter of $\alpha = \gamma_{\mathrm{YIG}} \Delta B_{\mathrm{FMR}}/\omega = 0.034$, with the gyromagnetic ratio $\gamma_{\mathrm{YIG}}/(2\pi) = 28\,\mathrm{GHz/T}$.Note that this value of α is an upper estimate,

since any frequency-independent contribution to the damping in effect will reduce the magnitude of α.

The magnitude of the ISHE spin pumping voltage is $23\,\mu$V at resonance which is in good approximation predicted in the calculation of Fig. 4.3. The slight discrepancy may be due to uncertainty in the determination of the YIG film thickness of sample #1, which is calculated from YIG deposition rate and time.

To analyze the properties of the cavity, we show cuts at fixed magnetic field as a function of frequency in Figs. 4.8(b,c). These fixed fields are indicated with arrows 'B-B' and 'C-C' in Fig. 4.7(a,b). At an off-resonant fixed field 'B-B' in (Fig. 4.8(b)), only the cavity absorption at $\omega_c = 9.848\,\text{GHz}$ with a linewidth of $\Delta\omega_c/(2\pi) = 2.6\,\text{MHz}$ is observed in the microwave signal, while there is no signal in V_{dc}. In the on-resonant case 'C-C' at B_{FMR} shown in Fig. 4.8(c), the cavity resonance position and linewidth are the same as in the off-resonant case. Additionally, an ISHE voltage signal with the same lineshape as that of the cavity absorption is found, showing the excitation of the spin system in resonance.

In summary, in the weak coupling limit, both the FMR and the spin pumping signals observed in experiment are qualitatively and quantitatively consistent with the corresponding theoretical expectations.

4.2.2 1 mm YIG/3 nm Pt bilayer

We now turn to sample #2, which is more strongly coupled to the cavity, due to the much larger number of spins $N_{s,2}$. Due to the appearance of an anticrossing, it is necessary to take data over a much larger frequency range than those in Fig. 4.7. In this much larger frequency window, standing wave interference patterns from the microwave feedline are visible. To better analyze the properties of the cavity and spin system, we subtract the feedline background. This is illustrated in Fig. 4.9. In Fig. 4.9(a), we show the microwave reflection data as measured. We clearly see the standing wave resonance from the feedline as horizontal stripes, overlaying the measurement signal from the coupled cavity and spin system. These standing wave resonances are independent of the applied magnetic field. The raw (as measured) $|S_{11}|^2(\omega)$ data at $B = 0.303\,\text{T}$ for $\omega/(2\pi) < 9.853\,\text{GHz}$ and at $B = 0.390\,\text{T}$ for $\omega/(2\pi) > 9.853\,\text{GHz}$ (red lines in Fig. 4.9(a)) show only the signature of these standing waves, and only negligible signal from the coupled spin-cavity system. We thus can subtract these data (Fig. 4.9(b)) from all other measured data at the respective

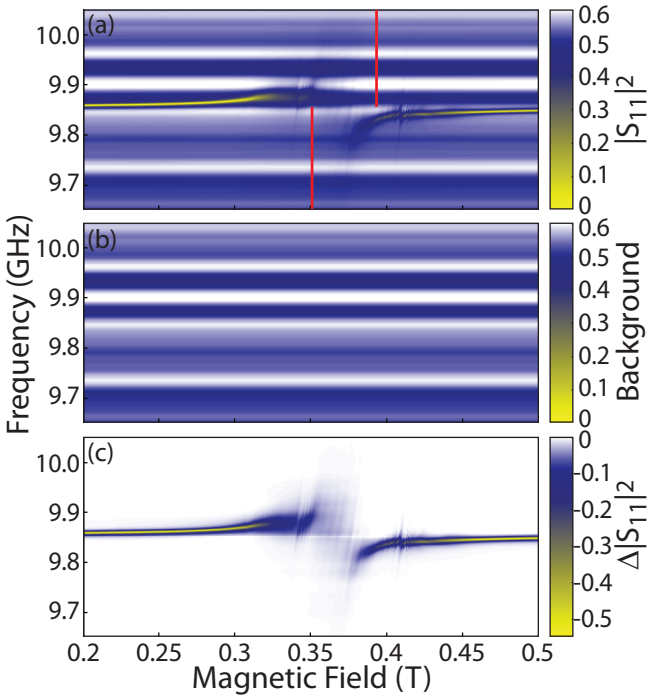

Figure 4.9: (a) $|S_{11}|^2$ (raw data). The red lines denote show the frequency field pairs chosen for background subtraction. (b) background to be subtracted. (c) $|S_{11}|^{2'}$ the backgound is subtracted. The data are the same as shown in Fig. 4.10(a).

frequencies and obtain the 'background-free' $\Delta|S_{11}|^2$ shown Fig. 4.9(c).

In Figure 4.10(a) the experimental microwave reflection data are displayed in a false color plot as a function of microwave frequency and applied magnetic field, over the whole measurement range. They are qualitatively different from the weak coupling regime (Fig. 4.7). The cavity absorption line, as predicted by our model (Fig. 4.4), is no longer continuous, but interrupted by several anticrossings. These clear distortions in the cavity dispersion are quantitative evidence that the system is not in the weak coupling limit. This is expected considering that the coupling is enhanced by a factor 100 compared to sample #1. In contrast to our calculation of Fig. 4.4, we see a series of anticrossings in Fig. 4.10(a), rather than a single anticrossing. These result from the coupling of the cavity to the uniform FMR mode as well as to several spin wave resonance modes that are excited in the bulk YIG. The coupling strengths, deduced from the gaps of the anticrossings, vary for the different resonances.

Unfortunately, the multitude of spin wave resonance modes impedes a quantitative determination of the coupling strength by a fit according to Eq. (4.36), since the

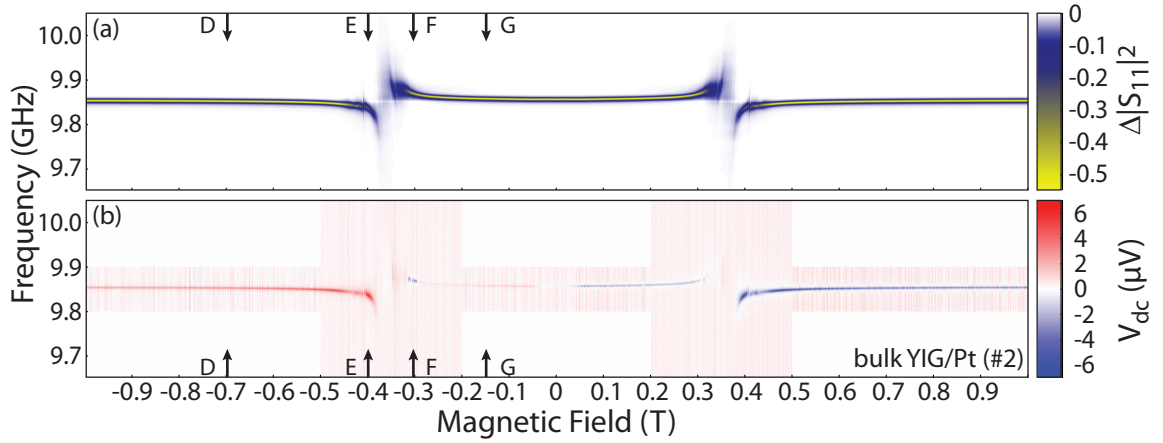

Figure 4.10: (a) measured microwave reflection $\Delta|S_{11}|^2$ of the bulk YIG/Pt sample (#2). $\Delta|S_{11}|^2$ is shown in a false color plot as a function of external magnetic field and microwave frequency. An anticrossing in the dispersions of cavity and spin is clearly visible. (b) measured spin pumping voltage V_{dc} of sample #2. V_{dc} follows the dispersion of the coupled cavity-spin system.

spin wave modes overlap, such that it is impossible to determine the exact number and resonant properties of these modes. It is thus difficult to reliably quantify the linewidth of the resonances of the spin system or their coupling to the cavity. We can estimate the coupling constant g_{eff} as 100 times the coupling strength of sample #1, $g_{\mathrm{eff}} = 3\,\mathrm{MHz} \times 100 = 300\,\mathrm{MHz}$, due to the larger number of spins in sample #2. However, the coupling strength also depends on the ac magnetic field and thus the sample placement in the cavity, meaning $g_{\mathrm{eff}} = 300\,\mathrm{MHz}$ is only a reference. The linewidth γ_{s} of bulk YIG (sample #2) is smaller by at least a factor of ten than that of sample #1, as determined by independent FMR experiments. Together with the approximately constant cavity relaxation rate, this suggests that strong coupling is reached in the FMR and spin pumping experiments performed on sample #2.

Figure 4.10(b) shows the dc voltage, recorded simultaneously with the microwave reflection data. Here, we find a dc voltage at spectral locations where microwave absorption is observed, with clearly resolved anticrossings. The sign of the voltage is positive for negative magnetic fields and negative for positive magnetic fields, consistent with a dc voltage arising from an ISHE voltage due to a pumped spin current, as already discussed in the context of Figs. 4.7 and 4.8 for sample #1.

Comparing the measured dc voltage data of Fig. 4.10(b) to the simulation of Fig. 4.4(b), we find that there are qualitative and quantitative differences. First,

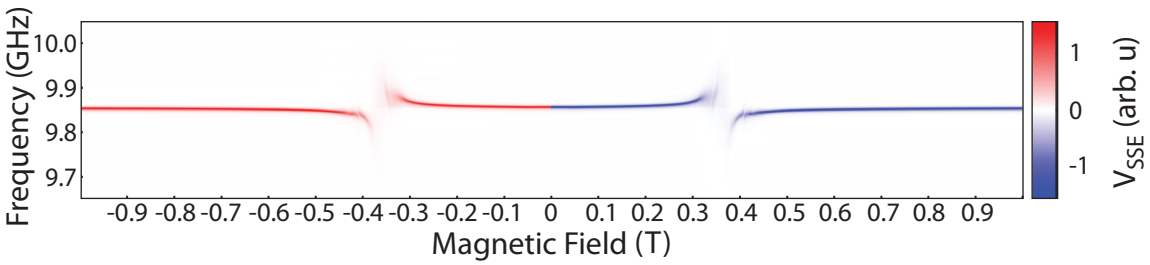

Figure 4.11: Spin Seebeck voltage signal calculated from absorbed microwave power.

the voltage persists at applied magnetic fields far larger and smaller than the resonance field. This is contrary to our model calculation, where the spin pumping dc voltage is only appears at frequency and magnetic field values close to the anticrossing, where the excited mode is partly magnetic-like. Second, the maximum magnitude of the measured dc voltage is approximately $6\,\mu$V, larger than the theoretically predicted magnitude of 60 nV in Fig. 4.4(b) by a factor of 100. Third, comparing the intensities of the dc voltage at magnetic fields lower than B_{FMR} with the dc voltage at magnetic fields higher than B_{FMR}, the data show a voltage of considerably lower magnitude on the lower field side of the anticrossing. This is contrary to our simulation of the spin excitation shown in Fig. 4.10(b), where the intensity is the same on both sides of the anticrossing. All of these observations lead us to the conclusion that the recorded dc voltage is not due to spin pumping. In addition to the excitation of the magnetization by absorption of microwave power, it can also be excited by a temperature gradient between the Pt film and the YIG. Similar to spin pumping, this also gives rise to the emission of a spin current into the Pt layer, with a polarization also along the direction of the magnetization in the ferromagnet. This is the longitudinal spin Seebeck effect (SSE). The spin current due to the SSE also generates a dc ISHE voltage, which changes polarity upon magnetic field inversion [17–23]. The temperature gradient driving the SSE voltage is due to an ac current induced in the Pt film by the microwave electric field in the resonator, causing Joule heating [86]. In a very simple model, the magnitude of the thermal gradient is proportional to the power absorbed by the cavity. The amount of microwave power absorbed by the coupled cavity-spin system can be inferred from the microwave absorption spectrum in Fig. 4.10(a). However, the SSE voltage cannot be calculated quantitatively, since the proportionality factor between the absorbed power and the temperature gradient that drives the SSE is not known. This factor depends on the distribution of the

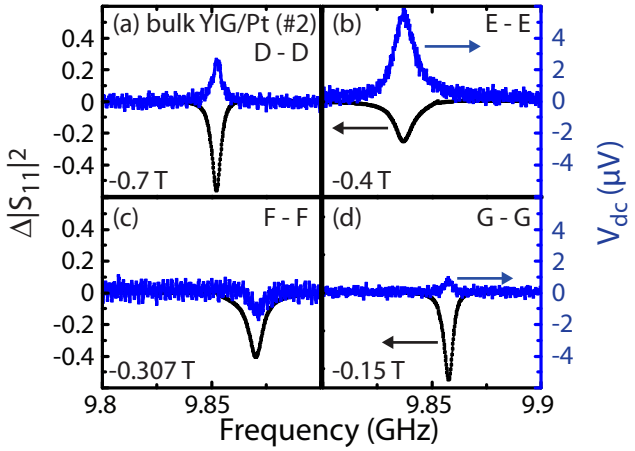

Figure 4.12: Measured microwave reflection $|S_{11}|^2$ and spin pumping voltage V_{dc} in sample # 2 at constant magnetic fields indicated by the arrows D, E, F, G in Fig. 4.10: The linewidth of the cavity mode as well as the resonance frequency are strongly dependent on the applied magnetic field, consistent with strong coupling. The magnitude of V_{dc} varies with applied magnetic field.

electric and magnetic fields in the loaded cavity and the sample position in the cavity. To completely suppress the SSE in a spin pumping experiment, a microwave cavity that does not feature any microwave electric field at the sample position has to be used for the spin pumping experiment. Since the SSE induced voltage also depends on the orientation of the magnetization in the YIG, it is predicted to change sign upon inversion of the magnetic field, as is observed in our experiment. Based on the reflection spectrum of Fig. 4.10(a), from which the absorbed power can be inferred, we calculate the relative magnitude of the SSE signal (proportional to the absorbed power) in Fig. 4.11. It reproduces many of the features observed in the dc voltage of Fig. 4.10(b). It shows the same anticrossings in the dc voltage, and the dc voltage appears over the whole magnetic field range. The dc voltage signal observed in experiment (Fig. 4.10(b)) is thus consistent with a SSE-induced ISHE voltage (Fig. 4.11). However, SSE cannot account for the lower magnitude of the magnitude of the voltage at magnetic fields smaller than the anticrossing field ($|B_0| < 0.3\,\mathrm{T}$), compared to magnetic fields larger than the anticrossing field ($|B_0| > 0.4\,\mathrm{T}$), which is a feature that appears in Fig. 4.10(b), but not in Fig. 4.11. Finally, we would like to point out that in a narrow magnetic field window around $B = \pm 0.3\,\mathrm{T}$ an inversion of the sign of the dc voltage also is observed. We have no explanation for this effect.

We now turn to frequency cuts at constant magnetic field shown in Fig. 4.12.

These constant magnetic fields are indicated by arrows 'D-D', 'E-E', 'F-F', and 'G-G' respectively in Fig. 4.10(a,b). In contrast to the data presented in Fig. 4.8 for the weakly coupled case, cuts at constant magnetic field show the characteristics of the combined cavity spin system, since the coupling is now much stronger. Therefore, it is sufficient to consider frequency cuts at constant field, since the characteristics of both the spin system and cavity can be seen in these frequency cuts.

At $B_0 = -0.7\,\mathrm{T}$ (Fig. 4.12(a)) a sharp resonance can be seen at the cavity frequency of 9.85 GHz. The linewidth is that of the cavity alone, $\Delta\omega_c/(2\pi) = 2.3\,\mathrm{MHz}$. The linewidth increases to $\Delta\omega/(2\pi) = 5.3\,\mathrm{MHz}$ at $B_0 = -0.4\,\mathrm{T}$ (Fig. 4.12(b)), due to the increasing mixing with the spin system, which is more strongly damped. The resonance field is shifted toward lower frequencies. After the anticrossing, at $B_0 = -0.307\,\mathrm{T}$ (Fig. 4.12(c)), the resonance frequency is shifted to higher frequencies while the dc voltage unexpectedly has a negative sign, as already mentioned above. At $B_0 = -0.15\,\mathrm{T}$ (Fig. 4.12(d)), the resonance linewidth of $\Delta\omega_c/(2\pi) = 2.3\,\mathrm{MHz}$ again reflects that of the cavity alone. There is a non-vanishing positive dc voltage, but it is smaller than at $B_0 = -0.7\,\mathrm{T}$.

The frequency cuts clearly illustrate that near the anticrossing, neither a measurement at fixed frequency nor a measurement at constant field will yield all the information about the spin system or microwave cavity. Instead both will show characteristics of the mixed system.

4.3 Conclusions

We have presented a study of the spin pumping not only as a function of the magnetic field but also of the microwave frequency in thin film YIG/Pt bilayer samples and bulk YIG/Pt bilayers samples. The increase of the volume of the YIG layer from thin film to bulk increases the coupling of the magnetic system to the microwave cavity in which the experiment takes place. When the magnetic system is of sufficiently large volume so that the effective coupling rate exceeds both the relaxation rates of the cavity and the spin system, the spin system and the cavity hybridize and strong coupling is reached. We have developed a theoretical model that quantitatively predicts the amplitude of the resulting spin pumping voltage and is valid for both the weak coupling and the strong coupling regime. This model also allows us to calculate the spin pumping voltage signal from the observed FMR signal, additionally

requiring only the knowledge of the spin mixing conductance of the interface, the spin Hall angle, and the spin diffusion length of the normal metal. Our model shows that to observe spin pumping in the strong coupling regime, the volume of the YIG crystal needs to be balanced between too small and too large: On the one hand, for a system to be in the strongly coupled regime, the ferromagnet needs to be of a certain size, enhancing the coupling. On the other hand, the larger the volume of the ferromagnet, the smaller the spin pumping spin current and the spin pumping voltage will be. Data from electrically detected spin pumping experiments performed on a thin film YIG/Pt bilayer sample are in good quantitative agreement with our model. When repeating the frequency and magnetic field dependent FMR and dc voltage measurements with a YIG(bulk)/Pt bilayer sample, we observe the anticrossing that is expected in strong coupling, in both the FMR signal and the dc voltage signal. However, the dc signal does not have the signature consistent with spin pumping in strong coupling, as predicted by our model. The observed voltage is instead attributed to the spin Seebeck effect, induced by microwave current Joule heating of the Pt layer of the sample.

Furthermore, we show that in standard EPR cavities, with typical cavity relaxation rates of a few MHz, low damping magnetic systems such as YIG, with linewidths as low as $\Delta B_{\mathrm{FMR}} \approx 0.05\,\mathrm{mT} \equiv 1.5\,\mathrm{MHz}$ [87], cannot be described in terms of weak coupling anymore, already for relatively low YIG film thicknesses of a few micrometers. Such YIG films may already be coupled strongly enough to the microwave cavity that the weak coupling limit, in which the relaxation rates of the spin system and the microwave cavity far exceed their coupling rate, is no longer applicable. In particular, this leads to an appreciable modulation of the cavity frequency as well as the cavity linewidth near ferromagnetic resonance fields, which has to be accounted for in the evaluation of FMR and spin pumping experiments. In these cases, FMR and spin pumping experiments should be performed not only as a function of magnetic field but also as a function of frequency to obtain an accurate picture of the spin resonance phenomena in the system and to account for the coupling effects.

When measuring only at the microwave cavity frequency ω_{c}, the dc voltage due to the spin Seebeck effect could even be erroneously attributed to spin pumping: At the resonant field of the spin system, the signal disappears due to the anticrossing. This signature is similar to a peak appearing at the resonant field of the spin system due to spin pumping.

To reduce the impact of the spin Seebeck voltage and thus simplify the analysis of the spin pumping voltage, the strong coupling spin pumping experiments should be performed in a microwave cavity with a very small microwave electric field at the sample position. Such a cavity has recently become available at the WMI. Furthermore, using a YIG crystal featuring a smaller FMR linewidth, which allows the reduction of sample size (and thus coupling strength) while still maintaining strong coupling, should make the spin pumping signal observable also in the strongly coupled regime. YIG films fabricated using liquid-phase epitaxy [88] are promising for this purpose, as they have very low damping and can be grown sufficiently thick to enable strong coupling. In the next step, time domain measurements of the spin pumping voltage could be considered.

To conclude, we here describe and test a model which allows for the calculation of the magnetic field and frequency dependent spin pumping voltage from the FMR reflection spectrum. It is thus an important tool to confirm spin pumping as the source of any measured dc voltage, and to distinguish it from voltages generated by the spin Seebeck effect or microwave rectification.

Chapter 5

Spin Pumping in Multi-Sublattice Magnetic Systems

5.1 Spin Pumping in the Compensating Ferrimagnet $Gd_3Fe_5O_{12}$

In Chapters 3 and 4, we discussed electrically detected spin pumping on yttrium iron garnet (YIG), a ferrimagnet. We have seen that the polarity of the pumped spin current, and the measured dc voltage depend on the magnetization orientation of the magnetic material. However, ferrimagnets comprise at least two magnetic sublattices, which are antiparallelly aligned by exchange interaction. In a two-sublattice ferrimagnet like YIG, the respective sublattice magnetizations $\mathbf{M}_1$ and $\mathbf{M}_2$ are not of equal magnitude, such that a total magnetization $M_{\mathrm{tot}} = M_1 - M_2$ prevails. In spin current-based experiments in ferrimagnets to date, this total magnetization is assumed to determine the polarization of the spin current flowing across the ferrimagnet/normal metal interface [21, 89–91]. In other words, ferrimagnets have been treated the same as ferromagnets, with a magnetization M_{tot}.

Not only spin pumping, but also spin Seebeck effect experiments have been analyzed in this fashion [17–23]. Qualitatively, the spin Seebeck effect is very similar to spin pumping. In both cases, the magnetic system is driven out of equilibrium, which results in a spin current being pumped into an adjacent normal metal layer. In the case of spin pumping, the excitation of the magnetic system is due to the absorption of microwave radiation. In the spin Seebeck effect, the non-equilibrium state is due to a thermal gradient between the normal metal and the magnetic material.

Recently, spin Seebeck experiments have been performed on gadolinium iron gar-

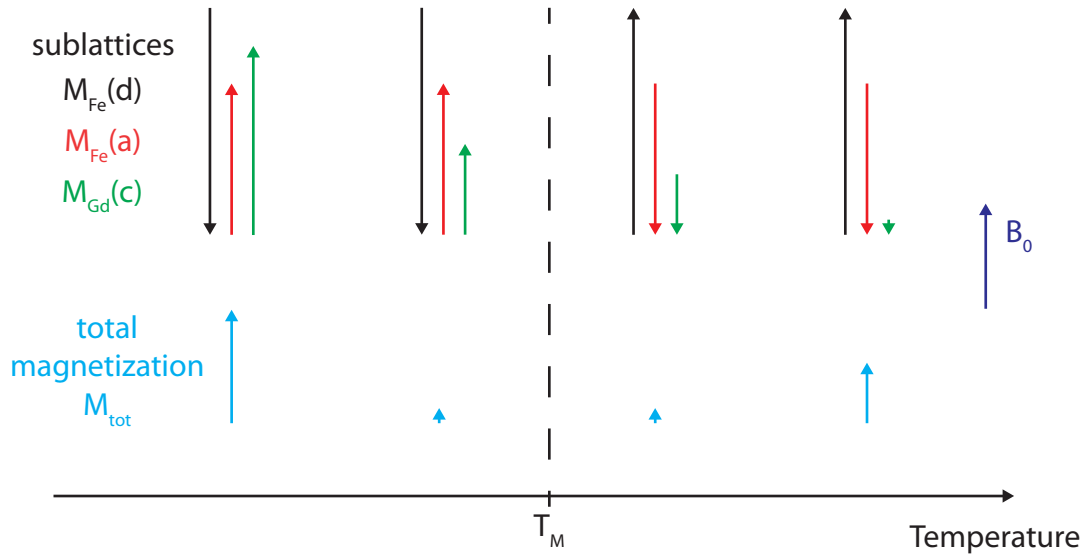

Figure 5.1: Sublattice and total magnetizations of gadolinuium iron garnet as a function of temperature in an external magnetic field B_0. At the compensation temperature T_M, the total magnetization vanishes and the sublattices magnetizations are reoriented.

net/platinum bilayers [92]. Gadolinium iron garnet ($Gd_3Fe_5O_{12}$, GdIG) is a ferrimagnet with three magnetic sublattices, the octahedrally coordinated Fe(III) ions (d-lattice sites), the tetrahedrally coordinated Fe(III) ions (a-lattice sites), and the Gd(III) ions (c-lattice sites), respectively (see Fig. 5.1) [93, 94]. The sublattice exchange interaction within the Gd lattice is much weaker than in the Fe lattices. Therefore, the magnetization of the Gd sublattice is strongly temperature dependent between room temperature and cryogenic temperatures, whereas those of the Fe sublattices are much less affected. Since the magnetization of the Gd sublattice strongly increases with decreasing tempeature, at a compensation temperature T_M the Gd magnetization becomes equal to the magnetization of the combined Fe sublattices, and the total magnetization vanishes. In the following, we will refer to such ferrimagnets with a magnetic compensation point as 'compensating ferrimagnets' [93, 95]. While the total magnetization is at all temperatures aligned along the magnetic field, in SSE experiments performed as a function of temperature on GdIG/Pt bilayers, two sign changes in the ISHE voltage were observed [92]. Clearly, the simple net magnetization based interpretation used in YIG and $NiFe_2O_4$ to date is no longer sufficient to explain the direction of the spin current polarization. Interestingly, neither spin pumping experiments nor theoretical predictions of pumped spin currents have been

put forward to date for compensating ferrimagnet/normal metal heterostructures.

This motivates the development of a model for spin pumping across a ferrimagnet/normal metal interface. We focus on the ferromagnetic mode of the ferrimagnet's magnetization dynamics [96,97]. Our approach explicitly takes into account the more complex magnetic sublattice configuration of the ferrimagnet, and is based on angular momentum conservation. We find that the polarization orientation of the pumped dc spin current depends on the effective gyromagnetic ratio of the ferrimagnet. We use this model to analyze our experimental data, obtained from a simultaneous measurement of both the electrically detected spin pumping and the spin Seebeck voltages in a yttrium and indium doped gadolinium iron garnet/platinum (InYGdIG/Pt) bilayer as a function of temperature from 6 K up to 295 K. InYGdIG features a compensation temperature of 85 K, which is easily accessible in our experimental setup. The temperature dependent voltage signal due to spin pumping is consistent with our model predictions, while the temperature dependent spin Seebeck signal is not. We thus conclude that resonance modes other than the ferromagnetic mode significantly contribute to the spin Seebeck spin current. The experimental work described in this section has been mainly performed by Kathrin Ganzhorn in the course of her master's thesis [98], which I supervised. The results of chapter 5.1 will be published as Ref. [99].

This section is organized as follows: In section 5.1.1, we develop the model describing the interface spin current generated by spin pumping, focusing on the ferromagnetic mode in ferrimagnets. In section 5.1.2, we discuss the temperature dependence of the orientation of the spin current polarization as a function of temperature in a compensating ferrimagnet. In section 5.1.3, we characterize our sample, an indium and yttrium doped GdIG/Pt bilayer, using SQUID magnetometry. We present the experimental setup used for measuring electrically detected spin pumping and spin Seebeck effect voltages simultaneously, on the same sample. In section 5.1.4, we show the dc voltage data as a function of external magnetic field at various temperatures above and below compensation temperature. We discuss the contributions to this voltage due to spin pumping, the spin Seebeck effect, and microwave rectification. In section 5.1.5, we discuss the temperature dependence of the spin pumping and spin Seebeck amplitudes and compare them to our model predictions. Finally, we summarize our results in section 5.1.6.

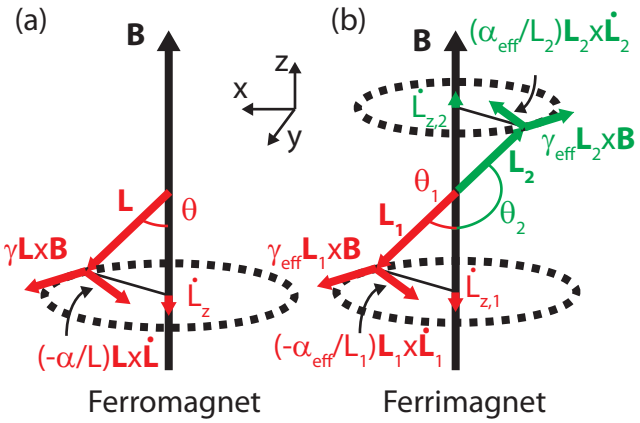

Figure 5.2: Precession modes in (a) a ferromagnet, (b) a ferrimagnet. (a) In a ferromagnet the angular momentum precesses around the magnetic field axis. Damping from the lattice and spin pumping results in a torque perpendicular to the angular momentum and the precession direction, which diminishes the precession cone angle θ. The change of angular momentum in the magnetic field direction is responsible for a pumped spin current in a FM/N bilayer. (b) In a ferrimagnet two sublattices are strongly antiferromagnetically coupled, so that they are antiparallel to each other. In the ferromagnetic resonance mode of a ferrimagnet, the angular momenta of the two sublattices stay antiparallel, and precess around the magnetic field axis together. An effective damping term, consisting of contributions from lattice damping and spin pumping in both sublattices results in a torque perpendicular to the angular momentum and the precession direction, which diminishes the precession cone angle θ_1. At the same time θ_2 is increased. This changes the angular momentum along the magnetic field direction in both sublattices. Since $L_1 > L_2$, there is a net change in L_z, resulting in a pumped spin current.

5.1.1 Modeling Spin Pumping in Multi-Sublattice Systems

In this section we develop a model to describe spin pumping in multi-sublattice ferrimagnets as a function of temperature. In ferromagnets, which comprise only a single magnetic lattice, spin pumping is usually modeled in the theory framework of Tserkovnyak, Brataas and Bauer [32–34]. This framework has been extended to the case of an easy axis antiferromagnet, featuring two identical magnetic sublattices, by Cheng *et al.* [100]. In this extension, the dynamics of the two sublattice magnetizations add constructively to the pumped spin current. However, ferrimagnets like GdIG possess more than two magnetic sublattices. Furthermore, their magnetic properties are different. All of the sublattices can be involved in the spin pumping process.

In our model approach, we consider a steady state situation which applies to most experimental situations. Here, the angular momentum continuously generated by an external perturbation (ac magnetic field, temperature gradient) is removed by dissipative effects. This dissipated angular momentum needs to be absorbed by another system (e.g. the mechanical lattice). In this sense, in the following we loosely speak about relying on angular momentum conservation to describe the pumped spin current. We calculate the dissipated angular momentum of all magnetic sublattices in a system using their individual precession trajectories. In spin pumping, a portion of that angular momentum is ejected to the normal metal as a spin current. While we focus on the ferromagnetic mode of the ferrimagnet, the approach can be generalized and applied to more complicated magnetization excitations.

To clarify the angular momentum conservation approach, we start by expressing the one-sublattice (ferromagnetic) spin pumping theory [32–34] explicitly in terms of angular momentum conservation. In this limit, our model reproduces the results by Tserkovnyak *et al.* In a second step, we then generalize our approach to systems with more than one magnetic sublattice.

We first consider a ferromagnet that can be described by a single magnetic sublattice with magnetization $\mathbf{M}$. The magnetization dynamics are described by the Landau-Lifschitz-Gilbert (LLG) equation [39]

$$\dot{\mathbf{M}} = \gamma \mathbf{M} \times \mathbf{B} + \frac{\alpha}{M} \mathbf{M} \times \dot{\mathbf{M}} \,. \tag{5.1}$$

It is useful to rewrite Eq. (5.1) in terms of angular momentum, using the gyromagnetic ratio $\gamma = -|\gamma| = -(MV)/L$:

$$\dot{\mathbf{L}} = \gamma \mathbf{L} \times \mathbf{B} - \frac{\alpha}{L} \mathbf{L} \times \dot{\mathbf{L}} \,, \tag{5.2}$$

where $L = |\mathbf{L}|$. The angular momentum dynamics according to Eq. (5.2) consist of two parts (see Fig. 5.2(a)): The first term defines the precessional motion of the angular momentum around the effective field $\mathbf{B} = B\hat{\mathbf{e}}_z$. It describes the torque that acts on the magnetic system due to the force exerted on the magnetization by the magnetic field. Although the x- and y-components of the angular momentum precess at a frequency $\omega = \gamma B$, the z-component is conserved (Fig. 5.2(a)). The second term describes the damping of the angular momentum toward its equilibrium position, antiparallel to $\mathbf{B}$, with a damping constant α. In bulk ferromagnets, the

torque inducing this relaxation is exerted by the lattice [39], thus the lattice acts as an effective angular momentum sink. The spin pumping mechanism also generates a damping torque, by transferring angular momentum to an adjacent normal metal adjacent as a spin current [32]. The normal metal then also acts as a spin sink. In the treatment of Tserkovnyak *et al.* [32–34], both lattice and spin pumping damping give rise to a generalized (Gilbert) damping constant:

$$\alpha = \alpha_0 + \alpha' \,, \tag{5.3}$$

where α_0 describes the lattice contribution, while α' parametrizes the spin pumping contribution.

Due to angular momentum conservation, the pumped dc spin current in the normal metal is proportional to the rate of change of the z-component of the angular momentum (torque) due to the second, damping, term in Eq. (5.2), with a proportionality constant α'/α. The identification of the additional damping torque generated by the spin pumping with this spin current I_s is the key idea of our model. We thus write:

$$I_s = -\dot{L}_z \frac{\alpha'}{\alpha} \,. \tag{5.4}$$

This equation can be understood as a result of the partition of the dissipated angular momentum into the normal metal versus the lattice. The pumped dc spin current is the fraction dissipated into the normal metal. The spin current flow direction is normal to the interface, going from the FM to the N. The spin current polarization is along z, meaning positive spin current is polarized along $+\mathbf{e}_z$, while negative spin current is polarized along $-\mathbf{e}_z$. For an increase of the angular momentum of the magnetic system in positive z-direction, angular momentum polarized in negative z-direction needs to be ejected from the magnetic system into the normal metal.

We now calculate the spin current based on Eq. (5.4) for a magnetic system with only one magnetic lattice. The change in the z-component of the angular momentum due to the damping term in Eq. (5.2) can then be expressed in terms of the precession cone angle θ (see Fig. 5.2(a)). Since $L_z = -\cos(\theta)L$, Eq. (5.4) becomes:

$$I_s = -L\sin(\theta)\dot{\theta}\frac{\alpha'}{\alpha} \,. \tag{5.5}$$

The evolution of the cone angle with time is determined by the LLG:

$$\dot{\theta} = \sin(\theta)\alpha\gamma B\,. \tag{5.6}$$

We insert Eq. (5.6) into Eq. (5.5), obtaining

$$I_s = -\sin^2(\theta)\alpha'\gamma BL\,. \tag{5.7}$$

This expression is equivalent the one put forward by Tserkovnyak *et al.* which is exactly the expression for the dc pumped spin current in a FM/N bilayer [11, 32]. Inserting the Eq. (2.8) for α' and the electron gyromagnetic ratio $-\gamma = g\mu_B/\hbar$ into Eq. 5.7, we find Eq. (2.11), which was already introduced in chapter 2. The partition principle of Eq. (5.4) therefore reproduces previous results.

We now extend this treatment to a system with two magnetic sublattices, using the same concept as for the case of a single magnetic lattice. In general, the magnetic sublattices consist of different magnetic ions. Their magnetization $\mathbf{M}_i$, angular momentum $\mathbf{L}_i$, gyromagnetic ratio γ_i, and damping constants $\alpha_{i,0}$, α_i' differ. The precession of a two sublattice system is described by two coupled LLG equations [96,97]. Assuming homogeneous excitations,

$$\dot{\mathbf{M}}_1 = \gamma_1\mathbf{M}_1 \times (\mathbf{B} - \beta\mathbf{M}_2) + \frac{\alpha_1}{M_1}\mathbf{M}_1 \times \dot{\mathbf{M}}_1 \tag{5.8}$$

$$\dot{\mathbf{M}}_2 = \gamma_2\mathbf{M}_2 \times (\mathbf{B} - \beta\mathbf{M}_1) + \frac{\alpha_2}{M_2}\mathbf{M}_2 \times \dot{\mathbf{M}}_2\,, \tag{5.9}$$

where $\beta > 0$ is a mean field parameter, parameterizing the antiferromagnetic coupling between the two sublattices. There are two eigenmodes [101, 102]: The first is the ferromagnetic mode, in which the sublattices align in opposite directions and precess around the external magnetic field axis with precession cone angles that satisfy $\theta_1 + \theta_2 = \pi$ (see Fig. 5.2(b)). This is similar to a simple ferromagnetic system. The other mode is the exchange mode, where the angle between the sublattices differs from 180 degrees, and the sublattice magnetizations essentially precess around the exchange fields $-\beta\mathbf{M}_i$ of the respective other magnetic sublattice.

We focus on the ferromagnetic mode in a ferrimagnet. This is the relevant case for magnetic resonance experiments on ferrimagnetic systems at low (few to tens of GHz) frequencies. By dividing Eq. (5.8) by γ_1 and Eq. (5.9) by γ_2 and then adding them, the precession in the ferromagnetic mode in terms of an unit vector of magnetization

$\boldsymbol{\mu} = \mathbf{M}_1/M_1$ evolves as [97]

$$\dot{\boldsymbol{\mu}} = \gamma_{\text{eff}} \boldsymbol{\mu} \times \mathbf{B} + \alpha_{\text{eff}} \boldsymbol{\mu} \times \dot{\boldsymbol{\mu}} \,, \tag{5.10}$$

with an effective gyromagnetic ratio [97]

$$\gamma_{\text{eff}} = \frac{-M_{\text{tot}} V}{L_{\text{tot}}} = \frac{-V(M_1 - M_2)}{L_1 - L_2} \,, \tag{5.11}$$

where V is the volume of the ferrimagnet. The effective damping constant is [97]

$$\alpha_{\text{eff}} = \frac{\alpha_1 L_1 + \alpha_2 L_2}{L_1 - L_2} \,. \tag{5.12}$$

The total magnetization is $\mathbf{M}_{\text{tot}} = (M_1 - M_2)\boldsymbol{\mu}$. Analogously to the ferromagnetic case, we express Eq. (5.10) in terms of angular momentum, or more precisely the unit vector of the angular momentum $\boldsymbol{\lambda} = \mathbf{L}_1/L_1$,

$$\dot{\boldsymbol{\lambda}} = \gamma_{\text{eff}} \boldsymbol{\lambda} \times \mathbf{B} - \alpha_{\text{eff}} \boldsymbol{\lambda} \times \dot{\boldsymbol{\lambda}} \,. \tag{5.13}$$

The sublattice damping constants, similar to the ferromagnetic case, consist of the contributions from both lattice and spin pumping,

$$\alpha_i = \alpha_{i,0} + \alpha_i' \,. \tag{5.14}$$

Similar to Eq. (5.4), we identify the dc pumped spin current as the z-component change of the angular momentum due to spin pumping,

$$I_s = -\dot{L}_{z,\text{tot}} \frac{\alpha_{\text{eff}}'}{\alpha_{\text{eff}}} \,. \tag{5.15}$$

Using $\dot{\mathbf{L}}_{\text{tot}} = (L_1 - L_2)\dot{\boldsymbol{\lambda}}$ and Eq. (5.13), we find

$$I_s = -\sin^2(\theta) \alpha_{\text{eff}}' \gamma_{\text{eff}} B (L_1 - L_2) \,, \tag{5.16}$$

which corresponds to Eq. (5.7) for the ferromagnetic case. It follows that spin pumping in ferrimagnets driven in the ferromagnetic mode can be described like a ferromagnet with an effective angular momentum $L_1 - L_2$, an effective gyromagnetic ratio γ_{eff}, and an effective spin pumping damping constant α_{eff}'. Since at room temperature, α_{eff}' is of

the same order of magnitude as in simple ferromagnets [90,91,103], the magnitude of spin pumping in ferrimagnets is similar to that in ferromagnets of a comparable total angular momentum (magnetization). This result explains why the spin pumping from yttrium iron garnet, a ferrimagnet, can be treated like a ferromagnet in spin pumping experiments [21,89–91,103].

Equation (5.16) can be rewritten in terms of the sublattice damping constants, in the form

$$I_s = -\sin^2(\theta)\gamma_{\text{eff}}B(\alpha_1' L_1 + \alpha_2' L_2)\,. \tag{5.17}$$

This expression is a key result of our model. It shows that each sublattice pumps angular momentum into the normal metal, with an amplitude given by their respective spin pumping damping constants α_i' (which are positive by definition). This corresponds to the description of antiferromagnetic spin pumping in Ref. [100]. Considering the sign of the pumped spin current, however, Eq. (5.17) shows that it is irrelevant which sublattice is in contact to the normal metal (or if both are). If one sublattice does not pump any spin current, then one of the α_i' in Eq. (5.17) is zero, which decreases the spin pumping amplitude, but does not change the sign. Moreover, it also does not matter in which direction (parallel or antiparallel to the external magnetic field) the pumping sublattice is oriented (note that L_1 and L_2 in Eq. (5.17) denote the magnitude of the sublattice angular momenta, which are positive by definition). Instead, the sign of the pumped spin current depends on the precession sense of the magnetic system, which is given by γ_{eff}. This is easily understood, because γ_{eff} determines which microwave polarization, i.e which direction of angular momentum, can be absorbed by the spin system from the microwave magnetic field driving the magnetic resonance. Owing to angular momentum conservation, only angular momentum absorbed by the magnetic system from the microwave can ultimately be ejected into the normal metal as a spin current. Note finally that the internal damping constants α_i can be substantially smaller than the effective damping constants α_{eff} (see Eq. (5.12)). The effective damping constant α_{eff} is measured directly in an FMR experiment through the FMR linewidth, while the individual α_i are more challenging to quantify experimentally.

The model can easily be expanded to describe an arbitrary number of sublattices, provided no canting occurs [104] (all sublattice angular momenta are either exactly

parallel or exactly antiparallel to each other):

$$I_{s,\mathrm{tot}} = -\sin^2(\theta)\gamma_{\mathrm{eff}} B \sum_i \alpha_i' L_i \,, \tag{5.18}$$

with

$$\gamma_{\mathrm{eff}} = \frac{-M_{\mathrm{tot}} V}{L_{\mathrm{tot}}} = \frac{-V \sum_i (\pm)_i M_i}{\sum_i (\pm)_i L_i} \,, \tag{5.19}$$

and

$$\alpha_{\mathrm{eff}} = \frac{\sum_i \alpha_i L_i}{\sum_i (\pm)_i L_i} \,, \tag{5.20}$$

where $(\pm)_i$ indicates if the sublattice is aligned parallelly or antiparallelly.

5.1.2 Temperature Dependence of the Pumped Spin Current in a Compensating Ferrimagnet

We now apply the above model to predict the temperature dependence of the polarization orientation of the pumped spin current in a compensating ferrimagnet. In a compensating ferrimagnet the sublattice magnetizations M_i have different temperature dependencies. We again use the notation in which M_i denote the magnitudes of the sublattice magnetizations, and are always positive. At the magnetization compensation temperature T_{M}, the total magnetization vanishes, $M_{\mathrm{tot}} = M_1 - M_2 = 0$. Furthermore, there also is an angular momentum compensation temperature, T_{L}, where $L_{\mathrm{tot}} = L_1 - L_2 = 0$. Note that $T_{\mathrm{M}} \neq T_{\mathrm{L}}$, if the gyromagnetic ratios of the sublattices differ.

In Fig. 5.3(a), we show a calculation of the dependence of M_{tot} and L_{tot} on temperature in a prototypical compensating ferrimagnet. The calculation is based on the mean field model proposed by Dionne [93, 105] to describe the magnetization of doped GdIG. In order to better illustrate the different regimes, (i) $T > T_{\mathrm{M}}, T_{\mathrm{L}}$, (ii) $T_{\mathrm{M}} < T < T_{\mathrm{L}}$, and (iii) $T < T_{\mathrm{M}}, T_{\mathrm{L}}$, we chose different magnitudes for the gyromagnetic ratios of the sublattices, $\gamma_2 = 0.6\gamma_1$[1]. This results in distinct compensation temperatures, T_{M}, T_{L}. In our example, $M_1 > M_2$ and $L_1 > L_2$ at room temperature. Upon lowering the temperature, M_2 and L_2 steadily increase. Since $\gamma_2 < \gamma_1$, $L_1 = L_2$ (or, equivalently, $M_1/\gamma_1 = M_2/\gamma_2$) is reached already at a higher temperature than $M_1 = M_2$. Therefore, $T_{\mathrm{L}} > T_{\mathrm{M}}$. We also calculate the effective gyromagnetic ratio

[1] The complete set of parameters used for the calculation is (in the nomenclature of Dionne [93, 105]):$k_d = 0.15$, $k_a = 0.02$ $k_c = 0.3$, $g_{\mathrm{Fe}} = 2$, and $g_{\mathrm{Gd}} = 1.2$

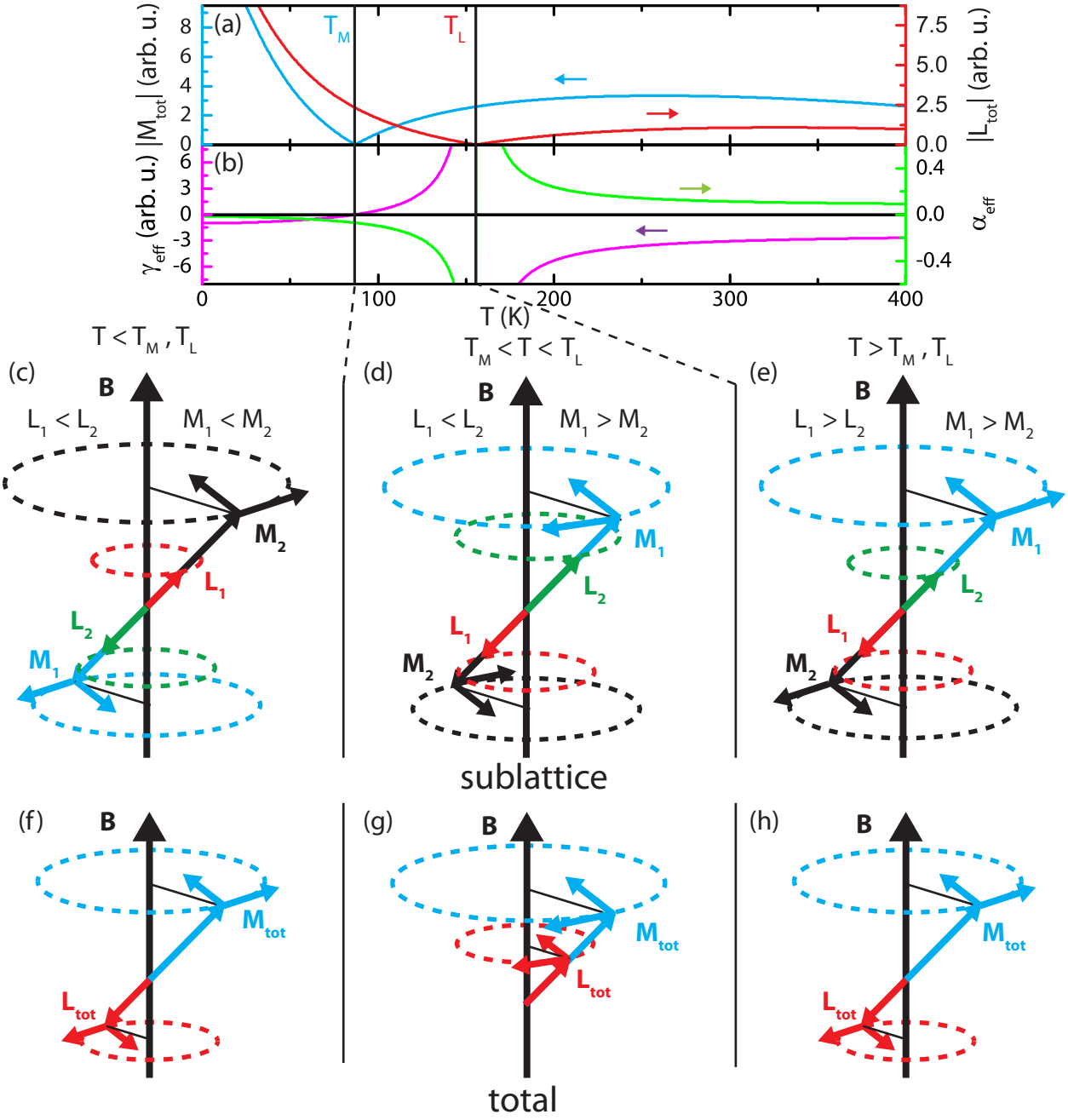

Figure 5.3: Model ferrimagnet composed of two sublattices with magnetizations M_1 and M_2 coupled antiferromagnetically. (a) Absolute values of M_{tot} and L_{tot} as a function of temperature. M_{tot} and L_{tot} vanish at their respective compensation temperatures, T_{M} and T_{L} (b) Temperature dependence of γ_{eff} and α_{eff}. (c-e) Illustration of the precession of the sublattices in the ferromagnetic mode in three different temperature ranges: (c) $T < T_{\mathrm{M}}, T_{\mathrm{L}}$ (d) $T_{\mathrm{M}} < T < T_{\mathrm{L}}$ (e) $T > T_{\mathrm{M}}, T_{\mathrm{L}}$ (f-h) Precession of the total magnetization and angular momentum in the three different temperature ranges.

γ_{eff} and effective damping constant α_{eff} according to Eqs. (5.11) and (5.12). These are shown in Fig. 5.3(b). The precession of the single sublattice magnetizations $\mathbf{M}_i$ and angular momenta $\mathbf{L}_i$ in all three regimes is sketched in Figs. 5.3(c-e). We also show the qualitative precession of the total magnetization $\mathbf{M}_{\text{tot}}$ and total angular momentum $\mathbf{L}_{\text{tot}}$ in the same three regimes (Figs. 5.3(f-h)).

Above T_{L}, $\mathbf{M}_{\text{tot}}$ is along $\mathbf{M}_1$, and $\mathbf{L}_{\text{tot}}$ is antiparallel to $\mathbf{M}_{\text{tot}}$, along $\mathbf{L}_1$ (Figs. 5.3(e) and (h)). We see that this results in a negative γ_{eff}. The precession is therefore right-handed. The effective damping constant α_{eff}, given by Eq. (5.20), is positive in this regime. According to Eq. (5.10), one finds that the damping works to align $\mathbf{M}_1$ (and the total magnetization $\mathbf{M}_{\text{tot}}$) along $\mathbf{B}$, and thus aligns $\mathbf{L}_{\text{tot}}$ antiparallelly to $\mathbf{B}$.

Between T_{L} and T_{M} (Figs. 5.3(d) and (g)), γ_{eff} is positive. This has two consequences. First, $\mathbf{M}_{\text{tot}}$ and $\mathbf{L}_{\text{tot}}$ are now parallel to each other, and second the magnetization precession is left-handed. This should result in a change of the polarization of the pumped spin current (see Eq. (5.17)). The reason for this sign change is apparent in Fig. 5.3(g). The damping still tries to align $\mathbf{M}_1$ (and the total magnetization $\mathbf{M}_{\text{tot}}$) along $\mathbf{B}$. (Note that the sign of α_{eff} is negative under these conditions, which is mandatory to maintain the damping-like character considering that the precession direction has inverted, too). The z-projection of the change of total angular momentum $\dot{L}_{\text{tot,z}}$ is inverted relative to the situation in Fig. 5.3(h).

The regime below T_{M} (Figs. 5.3(c) and (f)) is very similar to the one above T_{L}, with all label indices (1,2) exchanged. A negative γ_{eff} results in right-handed precession. In this case γ_{eff} and α_{eff} are of the same sign. The damping therefore aligns $\boldsymbol{\mu}$ in the direction opposite the external magnetic field. $\mathbf{M}_2$, which is antiparallel to $\boldsymbol{\mu}$ is aligned along $\mathbf{B}$. Since the total magnetization below T_{M} is parallel to $\mathbf{M}_2$, the total magnetization $\mathbf{M}_{\text{tot}}$ is damped toward the external magnetic field. The polarization of the pumped spin current is the same as in the temperatures above T_{L}. Note that if the polarization of the pumped spin current depended on the orientation of the individual sublattices, we would expect the opposite spin current polarization in this regime as compared to $T > T_{\text{M}}$, T_{L}.

In summary, our model predicts a sign change in electrically detected spin pumping, i.e. a reversal of the pumped spin current spin polarization, exclusively in the temperature range between T_{M} and T_{L}. The sign of spin pumping is the same for $T > T_{\text{M}}, T_{\text{L}}$ and for $T < T_{\text{M}}, T_{\text{L}}$, even though the sublattices have swapped orientations. (Figs. 5.3(c) and (e)) This holds irrespective of the values of α_i (see Eq. (5.17)).

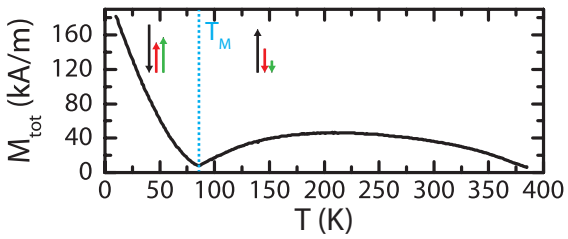

Figure 5.4: Magnetization of the InYGdIG/Pt bilayer as a function of temperature measured using SQUID magnetometry in an external magnetic field of 1 T. The magnetization compensation temperature $T_M = 85.5$ K is clearly evident as a dip in the $M(T)$ evolution. The arrows represent the relative orientations of the Fe d-sublattice (black) the Fe a-sublattice (red), and the Gd sublattice (green), respectively.

5.1.3 Sample and Experimental Setup

We studied spin pumping in the compensating ferrimagnetic insulator InYGdIG, due to the low ferromagnetic resonance linewidth of the material, as well as its convenient compensation temperature of about 85 K. The InYGdIG/Pt bilayer was fabricated by growing a 62 nm thick InYGdIG film on a (111)-oriented yttrium aluminum garnet substrate using laser MBE. The In/Fe ratio of the target was 1:4, while the Y/Gd ratio was 1:2. After the growth process, the sample was transferred to an electron beam evaporation chamber without breaking the vacuum, where a 3.6 nm thick platinum film was deposited onto the InYGdIG layer. From the $5 \times 5\,\mathrm{mm}^2$ sample fabricated this way we cut a $1.9 \times 5\,\mathrm{mm}^2$ piece for use in our experiments. The sample was prepared in close analogy to the samples discussed in Ref. [92].

The magnetic properties of the bilayer were studied via SQUID magnetometry, in an external magnetic field of 1 T applied in the thin film plane. The total magnetization M_{tot} is plotted as a function of temperature in Fig. 5.4. It shows the typical behavior for this class of compensating ferrimagnets [106, 107]: The d-lattice magnetization (black arrow) is antiparallel to the a-(red arrow) and c- lattice (green arrow) magnetizations. The net Fe magnetization is largely independent of temperature in the investigated temperature range due to the strong exchange coupling. At room temperature, it exceeds the Gd magnetization, and is aligned to the external magnetic field. Upon lowering the temperature, the magnetization of the Gd sublattice increases strongly. Due to the much weaker exchange coupling it follows a Brillouin-type behavior of an exchange-enhanced paramagnet. At a certain temperature, the

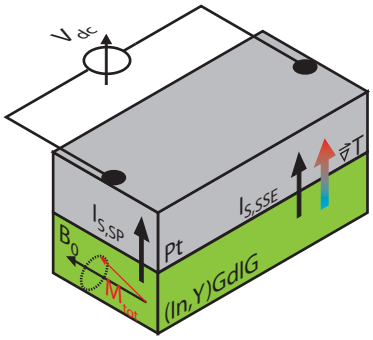

Figure 5.5: Schematic view of the GdIG/Pt bilayer. At ferromagnetic resonance conditions, the magnetization precesses, resulting in a spin current $I_{\mathrm{S,SP}}$ from the GdIG into the Pt (spin pumping). A microwave current flowing in the Pt gives rise to a temperature gradient, leading to a pumped spin current of $I_{\mathrm{S,SSE}}$, due to the spin Seebeck effect. Both spin currents are detected by conversion into charge currents by the ISHE and detection as a voltage through the electrical connections on the short sides of the Pt layer.

magnetization compensation temperature T_{M} (with $T_{\mathrm{M}} = 85.5\,\mathrm{K}$ in our case), the Gd magnetization equals the net iron magnetization. At $T < T_{\mathrm{M}}$, the Gd magnetization aligns to the applied magnetic field while the net iron magnetization (which now is smaller than the Gd one) is antiparallel to the external magnetic field.

For the electrical measurements of the bilayers, the Pt film was contacted at the short sides (see Fig. 6.2). The sample was then inserted into a Bruker 4118X-MD5 microwave cavity resonator, with a resonance frequency of $\omega_{\mathrm{C}}/(2\pi) = 9.7\,\mathrm{GHz}$. The microwave radiation at a power of 63 mW was provided by an Agilent E8257D microwave source. An external magnetic field of $-0.6\,\mathrm{T} < B_0 < 0.6\,\mathrm{T}$ was applied in the plane of the bilayer, along the short side of the sample. Ferromagnetic resonance was recorded by measuring the microwave reflection from the cavity using homodyne detection.

When sweeping the external magnetic field, FMR is excited at the resonance field in the InYGdIG which gives rise to a spin current flowing from the resonantly excited InYGdIG to the Pt (spin pumping, see Fig. 6.2). This spin current is converted into a charge current due to the inverse spin hall effect (ISHE) and then detected as a dc voltage V_{dc}, using a nanovoltmeter connected to the contacts on the Pt. While the sample is carefully placed at the minimum of the microwave electric field in the cavity, the microwave electric field is not zero over the whole sample volume and metallic contacts. This leads to an induced microwave current in the Pt layer, resulting in

Joule heating of the Pt. Consequently, a thermal gradient from the InYGdIG to the Pt develops, giving rise to a spin Seebeck spin current (see Fig. 6.2) [86]. This spin current is also observed by measuring the resulting ISHE voltage. The resonator was placed in a He flow cryostat during the experiments, so that the temperature could be adjusted between 4 K and 300 K. We performed dc voltage measurements as a function of external magnetic field B_0 at various, fixed temperatures. Due to the heating of the sample by the microwave current, the cryostat temperature is lower than the sample temperature in our experiments. By comparing the SSE amplitudes measured at different input power and different cryostat temperatures near the compensation temperature, we estimate that the sample temperature exceeds the cryostat temperature by 18 K at a microwave power of 63 mW, and an indicated cryostat base temperature of 70 K. However, this temperature difference may vary with cryostat base temperature, which is why we only state the cryostat temperature (and not the sample temperature) in our results presented below. This, and the difference of applied external magnetic fields, leads to a discrepancy in compensation temperatures when comparing the SQUID magnetization and the dc voltage data.

5.1.4 Experimental Results

In Fig. 5.6, we show the dc voltage data measured at selected temperatures, both for a magnetic field upsweep and a downsweep. These voltage signals consist of three separate contributions: A spin Seebeck voltage V_{SSE}, a spin pumping voltage V_{SP} and a microwave rectification voltage V_{SMR}. At a fixed temperature, V_{SSE} is dependent on the direction of the total magnetization in the ferrimagnet. Therefore, this signal changes its sign upon field inversion, showing a characteristic hysteresis reminiscent of the hysteresis in the $M(H)$ curve. It can phenomenologically be modeled by a modified Langevin function:

$$V_{\mathrm{SSE}} = A_{\mathrm{SSE}} \left(\frac{\cosh((B_0 - B_{\mathrm{c}})/s)}{\sinh((B_0 - B_{\mathrm{c}})/s)} - \frac{s}{B_0 - B_{\mathrm{c}}} \right) , \tag{5.21}$$

where B_0 is the external magnetic field, B_{c} is the coercive field, s parametrizes the slope of the hysteresis, and A_{SSE} is the amplitude of the spin Seebeck effect, defined as half the difference between the saturation SSE signal at positive and negative B_0.

The spin pumping voltage V_{SP} is characterized by symmetric Lorentzian peaks localized at the FMR resonance fields. They invert their sign upon magnetization

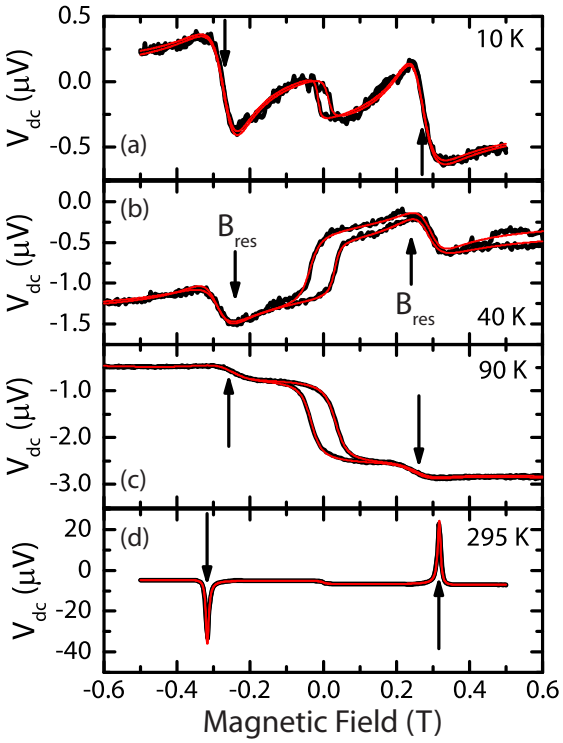

Figure 5.6: DC voltage measurement at various temperatures for a magnetic field upsweep and downsweep (black line). The resonance fields are indicated by black arrows. The red lines are fits according to Eq. (5.24).

reversal [12,85]. Thus V_{SP} can be modeled as

$$V_{\mathrm{SP}} = \frac{A_{\mathrm{SP}}\Delta B^2}{(B_0 - B_{\mathrm{res}})^2 + \Delta B^2} - \frac{A_{\mathrm{SP}}\Delta B^2}{(B_0 + B_{\mathrm{res}})^2 + \Delta B^2}\,, \tag{5.22}$$

where B_{res} is the FMR resonance field, ΔB is the FMR linewidth, and A_{SP} is the amplitude of the Lorentzian spin pumping signal at positive magnetic field.

The microwave rectification voltage V_{SMR} is caused by a microwave current in the Pt, combined with a modulation of the resistance of the platinum at the same frequency. In conducting ferromagnets this phenomenon is well known and the modulation is due to anisotropic magnetoresistance (AMR) [52–54]. Recently, the same effect has also been shown to exist in ferromagnetic insulator/normal metal bilayers showing spin Hall magnetoresistance (SMR), where the SMR substitutes for the AMR [55, 56]. The modulation of the Pt resistance is strongest near the resonance fields, because the precession amplitude of the magnetization is greatest near reso-

nance. This leads to a signal that is centered around the FMR resonance fields, just like spin pumping. The line shape of V_{SMR} is a combination an antisymmetric (peak-dip) shape around the resonance field and a Lorentzian (symmetric line shape). The amplitude and the polarity of both the symmetric and antisymmetric contributions to V_{SMR} depend on the phase difference between the microwave current in the Pt and the microwave magnetic field, as well as the orientation of the sample relative to the external magnetic field B_0 and the microwave magnetic field [56, 108, 109]. Since it is virtually impossible to completely suppress rectification effects, in particular since rectification only linearly scales with the FMR linewidth, we take into account a V_{SMR} which consists of a symmetric part $V_{\mathrm{SMR,s}}$ as well as an antisymmetric part $V_{\mathrm{SMR,a}}$. Since the symmetric part of V_{SMR} unfortunately shows the same symmetry as V_{SP} (Eq. (5.22)) and thus cannot be easily distinguished from spin pumping voltage, we therefore can only extract the total symmetric voltage signal, $V_{\mathrm{S}} = V_{\mathrm{SP}} + V_{\mathrm{SMR,s}}$, with an amplitude A_{S}. The antisymmetric part of V_{SMR} can be expressed as [56, 108, 109]

$$V_{\mathrm{SMR,a}} = \frac{A_{\mathrm{A}}\Delta B(B_0 - B_{\mathrm{res}})}{(B_0 - B_{\mathrm{res}})^2 + \Delta B^2} + \frac{A_{\mathrm{A}}\Delta B(B_0 + B_{\mathrm{res}})}{(B_0 + B_{\mathrm{res}})^2 + \Delta B^2}\,. \tag{5.23}$$

Here, A_{A} is the amplitude of the antisymmetic Lorentzian type voltage. All contributions, V_{SSE}, V_{S}, and $V_{\mathrm{SMR,a}}$ are evident in Fig. 5.6 (a), where we show the DC voltage data recorded at a base temperature of 10 K. At the resonance fields B_{res}, marked by black arrows, we find a superposition of symmetric (spin pumping and rectification) voltages and antisymmetric rectification voltages. For an external field of $-B_{\mathrm{res}}$, the Lorentzian has a negative sign, while at B_{res} the Lorentzian is positive, yielding a positive A_{S}. Near zero magnetic field the hysteresis characteristic of the SSE voltage is evident. In this case the SSE voltage is positive for negative fields, and negative for positive fields, corresponding to a negative A_{SSE}. The red line is a fit of the observed voltage to

$$V_{\mathrm{dc}} = V_{\mathrm{S}} + V_{\mathrm{SMR,a}} + V_{\mathrm{SSE}} + V_0 + cB_0\,, \tag{5.24}$$

where V_0 accounts for a constant offset voltage in the nanovoltmeter, and cB_0 accounts for a thermal drift as well as the (linearized) effect of increasing applied magnetic field on the magnetization. The fit is performed separately for the up- and downsweeps.

For the 40 K measurement shown in Fig. 5.6(b), V_{dc} is qualitatively different compared to the measurement at 10 K. As can be seen most easily again in the hysteretic part of the voltage, A_{SSE} is now positive. The sign of A_{S} is also still positive. At 90 K

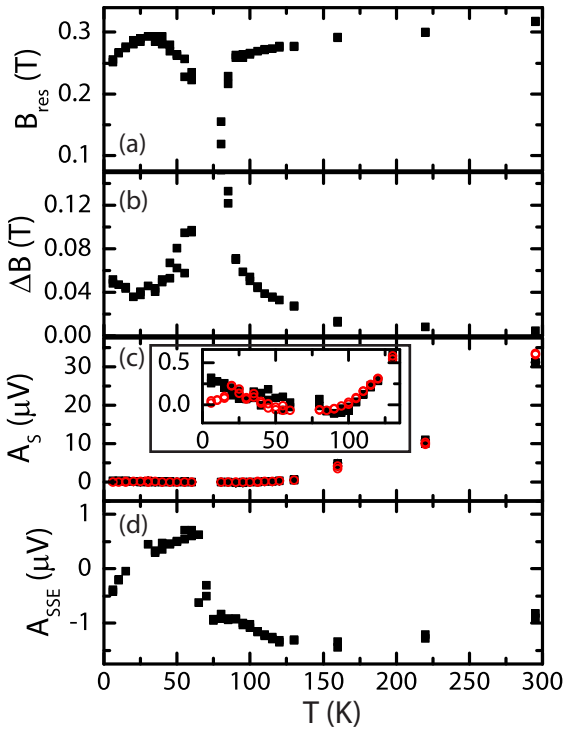

Figure 5.7: Analysis of the dc Voltage V_{dc} measured as a function of temperature. Fitting with Eq. (5.24) yields (a) the magnetic resonance field B_{res}, (b) the FMR linewidth ΔB, (c) the amplitude A_{S} of the symmetric Lorentzian contribution to the dc voltage, and (d) the spin Seebeck amplitude A_{SSE}. The red dots in (c) are calculated using Eq. (5.26)

(Fig. 5.6(c)), A_{SSE} is negative, as in the 10 K measurement. Moreover, the sign of A_{S} is now is inverted. At 295 K (Fig. 5.6(d)), A_{S} is now clearly positive, like at the lowest temperatures. The sign of A_{SSE} does not change relative to the 90 K measurement.

In summary, our experiments show that both the spin Seebeck effect amplitude A_{SSE} as well as the amplitude A_{S} of the symmetric part of the dc voltage V_{dc} each invert their respective signs twice in the temperature range between 10 K and 295 K. We also note that the FMR resonance fields B_{res}, marked by black arrows in Fig. 5.6, and the corresponding FMR linewidth ΔB substantially change as a function of temperature.

5.1.5 Discussion

Figure 5.7 shows a compilation of the information extracted from the fits to the dc voltages measured at various temperatures. We extract the magnetic resonance

field, the resonance line width, the amplitude of the spin Seebeck effect, A_{SSE}, and the amplitude of the symmetric part of V_{dc}, A_{S}, by fitting the $V_{\mathrm{dc}}(B_0)$ curves with Eq. (5.24).

Since in InYGdIG, the sublattice gyromagnetic values are very similar to each other [110,111], T_{M} and T_{L} differ only slightly. We thus cannot experimentally differentiate T_{M} and T_{L} within our temperature resolution of 2 K and use the term compensation temperature for both T_{M} and T_{L} synonymously in this section.

We first discuss the resonance field B_{res} plotted in Fig. 5.7(a). We find that B_{res} clearly decreases when approaching the compensation temperature of 80 K both from higher and lower temperatures. We expect this behavior for $T > T_{\mathrm{L}}$ (80 K-100 K), since γ_{eff} strongly increases near T_{L} (Eq. (5.19)), corresponding to a decrease of the resonance field as corroborated by our experiment. We attribute the drop of the resonance field at temperatures lower than the compensation temperature (40 K-60 K) to the cubic anisotropy that is present in InYGdIG. This anisotropy reduces the magnetic resonance field. When the total magnetization decreases close to compensation, the role of anisotropy is enhanced, since the effective anisotropy field increases as $K_{\mathrm{c}}/M_{\mathrm{tot}}$ [97, 112], where K_{c} is the cubic anisotropy constant. Taken together, the temperature dependence shown in Fig. 5.7(a) is the typical behavior for GdIG near compensation [113,114].

The resonance half width at half maximum linewidth ΔB is shown in Fig. 5.7(b) and shows a strong increase around compensation. This behaviour is expected from Eq. (5.20): At the angular momentum compensation point T_{L}, α_{eff} strongly increases, leading to an increased linewidth in FMR. The measurement of the FMR resonance position and linewidth allows us to localize the compensation point to about (70 ± 10) K (cryostat temperature).

In Fig. 5.7(c), the amplitude A_{S} of the symmetric Lorentzian-type voltage is shown as a function of temperature (black dots). A_{S} changes sign twice as a function of temperature, around 102 K and again between 60 K and 80 K. According to the model for spin pumping in compensating ferrimagnets proposed in Sects. 5.1.1 and 5.1.2, two sign changes of the spin pumping ISHE voltage are indeed expected, one at T_{M} and another at T_{L}. However, since the gyromagnetic ratios of Fe and Gd are very similar, T_{M} and T_{L} in our InYGdIG film cannot differ by more than 40 K. Furthermore, as discussed above, the compensation temperature is between 60 K and 80 K, such that the sign change at about 100 K cannot be understood in terms of spin pumping alone.

However, the observed behavior can be rationalized considering both the spin pumping and rectification voltages. Both are strongly dependent on the magnetic resonance linewidth. In spin pumping, the measured voltage is proportional to $\sin^2(\theta) \approx \theta^2$, where θ is the precession cone angle (see Eq. (5.17) in Sect. 5.1.1). At constant microwave power, the precession cone angle at resonance can be approximated by [115]

$$\theta = \frac{b_1}{\Delta B}\,, \tag{5.25}$$

where b_1 is the microwave magnetic field, which depends on microwave power. It follows that the spin pumping voltage depends on ΔB as $1/\Delta B^2$. Conversely, the rectification voltage depends on $\sin(\theta)$, [56, 108, 109] and thus depends on ΔB as $1/\Delta B$. Therefore, if ΔB is small, the spin pumping contribution to A_S will dominate, while rectification contributions to A_S will become increasingly relevant when ΔB becomes large, i.e. near compensation. To disentangle the two contributions to A_S shown in Fig. 5.7(c) we analyze A_S with

$$A_\mathrm{S} = \frac{C_\mathrm{SMR}}{\Delta B} + \frac{C_\mathrm{SP}}{\Delta B^2}\,. \tag{5.26}$$

The red open circles in Fig. 5.7 (c) are calculated according to Eq. (5.26), using as parameters $C_\mathrm{SMR} = -1.5 \times 10^{-8}\,\mathrm{VT}$, $C_\mathrm{SP} = 8.3 \times 10^{-10}\,\mathrm{VT}^2$ and the measured values of ΔB depicted in Fig. 5.7 (b). The evolution of $A_\mathrm{S}(T)$ is nicely reproduced by this simple model. The sign changes in A_S evident in Fig. 5.7 (c) are thus not related to sign changes in spin pumping, but rather to the competition between spin pumping and rectification effects (with opposite sign) as a function of temperature. This implies that our data does not yield any evidence for a change of the spin polarization orientation of the pumped spin current. This indeed is in accordance to the model developed in Sect. 5.1.1, as we expect a sign change in spin pumping only in the very narrow temperature window between T_M and T_L. Since this temperature range presumably is very narrow (a few K at best) it is difficult to resolve in our experiment. In addition, the electrically detected spin pumping voltage scales unfavorably with the FMR linewidth, which makes it even more difficult to resolve.

We now turn to the measured spin Seebeck amplitude displayed in Fig. 5.7(d). Around room temperature, we find a weakly temperature dependent spin Seebeck amplitude $A_\mathrm{SSE} < 0$. Since the spin Seebeck effect voltage is unaffected by the increase in FMR linewidth, it can be measured in the compensation region, where an abrupt

sign change in the temperature window of $65\,\mathrm{K} < T < 75\,\mathrm{K}$ is observed. Another, more gradual sign change takes place at a much lower temperature of $T \approx 20\,\mathrm{K}$. A similar behavior in the spin Seebeck amplitude has been reported by Geprägs *et al.* [92] in gadolinium iron garnet/Pt thin film bilayers. There, the sign changes in the spin Seebeck effect take place at higher temperatures, due to the higher compensation temperature in undoped GdIG.

The SSE temperature dependence is evidently different from the one observed for spin pumping. In spin pumping, the voltage sign inverts due to spin current spin polarization reversal, which, according to the model in Sect. 5.1.1, is restricted to the compensation temperature region. More precisely, the spin current pumped by the ferromagnetic mode of the ferrimagnet is expected to invert its polarization once at T_M and once at T_L. This is not the case for the spin Seebeck effect, where at least one inversion in spin current polarization is observed at temperatures far below either T_M or T_L and only a single sign change occurs in the spin Seebeck voltage near the compensation temperature. The qualitative discrepancies between the SSE spin current and the spin current pumped by the FMR mode may seem surprising, because the mechanisms generating the pumped spin current in spin pumping and the spin Seebeck effect usually are assumed to be very similar [57]. We note, however, that the excitation of the spin system which is at the origin of the two effects is qualitatively different. In spin pumping, only a single mode is excited, the ferromagnetic resonance mode of the ferrimagnet, which is selectively driven by the microwave radiation. In the SSE, on the other hand, the spin system is excited thermally, over a broad range of frequencies and wave numbers. All possible magnon modes with an energy of less than $k_\mathrm{B}T$ are excited, including the exchange mode in the ferrimagnet, which is not included in the model discussed in Sect. 5.1.1. We speculate that the sign change in the SSE at $T \approx 20\,\mathrm{K}$ could be due to the freezing out of the exchange modes, as 20 K correspond to about 400 GHz, comparable to exchange mode frequencies [96]. Therefore, the different temperature dependence of the spin current resulting from spin pumping and the SSE suggests that exchange modes are very important for a detailed understanding of the spin Seebeck effect in compensating ferrimagnets. Further experiments however are warranted to corroborate this conjecture.

5.1.6 Summary and Conclusions

We have developed a model for spin pumping based on angular momentum conservation, describing the spin current that is pumped into a normal metal layer from a ferrimagnet excited in the ferromagnetic mode. According to this model, the spin current pumped by the ferromagnetic mode can invert its polarization (sign) only in the temperature range between the magnetization compensation temperature T_M and the angular momentum compensation temperature T_L. Moreover, the polarization of the pumped spin current does not depend on which magnetic sublattice is in contact with the normal metal at the interface (or if both are). We compare these predictions to spin pumping measurements, performed as a function of temperature on a indium and yttrium doped gadolinium iron garnet/Pt heterostructure. InYGdIG is a compensating ferrimagnet, with $T_\mathrm{M} \approx T_\mathrm{L} \approx 85\,\mathrm{K}$. The evolution of the electrically detected (ISHE) spin pumping voltage observed in experiment can be semi-quantitatively understood in our model. To further corroborate the model laid out in chapter 5.1.1, spin pumping should be performed on a compensating ferrimagnet featuring a larger separation between the compensation temperatures T_M and T_L. An inversion of the sign of the spin pumping voltage signal should then be observable between T_M and T_L. Replacing the gadolinium of GdIG with other rare earth elements with non-zero orbital angular momentum (e.g. dysprosium) should result in a rare earth sublattice gyromagnetic ratio which is considerably lower than that of the iron sublattices. Since the separation of the compensation temperatures depends on the difference of the sublattice gyromagnetic ratios, such garnets should be promising candidates for these experiments.

Interestingly, spin Seebeck measurements performed simultaneously to the magnetic resonance experiments show a qualitatively different behavior. The SSE voltage changes sign twice, once around T_M and again at a much lower temperature $T \approx 20\,\mathrm{K}$. This strongly suggests that the excitation of other magnon modes than the ferromagnetic mode – e.g. exchange modes – has to be taken into account to achieve a solid understanding of the temperature dependence of the spin Seebeck effect. In principle the approach detailed here can also be used to describe spin pumping by exchange modes. Then the temperature dependent occupation of these magnon modes along with their (temperature dependent) effective gyromagnetic ratios should allow for the description of the spin Seebeck effect voltage as a function of temperature.

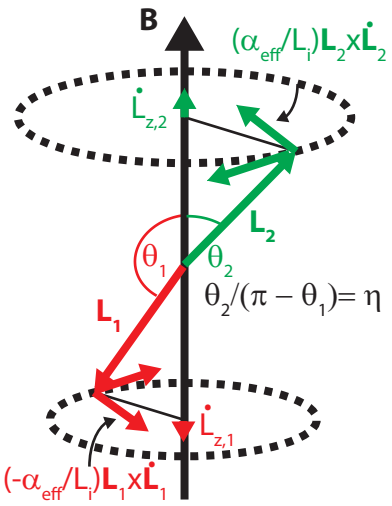

Figure 5.8: The precession of the angular momentum of the two sublattices in an easy axis antiferromagnet in the left-handed (-) mode (See text). $\mathbf{L}_2$ is more strongly deflected from the z-axis than $\mathbf{L}_1$. The ratio of the cone angles of the sublattices $\eta = \theta_2/(\pi - \theta_1)$ is a constant dependent on the antiferromagnetic material. The pumped dc spin current is proportional to the change in total z-direction angular momentum, $\dot{L}_{z,1} + \dot{L}_{z,2}$.

5.2 Spin Pumping in the Antiferromagnet MnF_2

In this section, we transfer the model we developed in Sect. 5.1.1 for the ferromagnetic resonance mode of the ferrimagnet to the exchange resonance modes of an easy-axis antiferromagnet. Subsequently, we test this approach on the model easy axis antiferromagnet MnF_2. We perform magnetic field and frequency dependent FMR resonance and spin pumping on a MnF_2 single crystal on which a platinum strip has been deposited. Although we measure a dc signal across the platinum strip, we conclude that this signal is not due to spin pumping. The experimental work described in this section has been performed by Marc Philipp Ross in the course of his diploma thesis [116], which I supervised.

5.2.1 Modeling Spin Pumping in Antiferromagnets

Antiferromagnetic Resonance Modes

The coupled LLG equations that describe the dynamics of the antiferromagnetic sublattice excitations of an easy axis antiferromagnet are very similar to the ones de-

scribing the dynamics of the ferrimagnet (see Eqs. (5.8) and (5.8)) [117].

$$\dot{\mathbf{M}}_1 = \gamma_1 \mathbf{M}_1 \times (\mathbf{B} - \beta \mathbf{M}_2 + B_\mathrm{A} \mathbf{e}_z) + \frac{\alpha_1}{M_1} \mathbf{M}_1 \times \dot{\mathbf{M}}_1 \tag{5.27}$$

$$\dot{\mathbf{M}}_2 = \gamma_2 \mathbf{M}_2 \times (\mathbf{B} - \beta \mathbf{M}_1 - B_\mathrm{A} \mathbf{e}_z) + \frac{\alpha_2}{M_2} \mathbf{M}_2 \times \dot{\mathbf{M}}_2 \,, \tag{5.28}$$

The only difference to the ferrimagnetic case is the addition of an uniaxial anisotropy field B_A in along the z-axis, parallel to the external magnetic field. The two sublattices are identical, so that $M_1 = M_2 = M_i$, $\gamma_1 = \gamma_2 = \gamma_i$, and $\alpha_1 = \alpha_2 = \alpha_i$. The precession modes that result from the coupled equations (5.27) and (5.28) have been calculated in [117]. Both sublattice magnetizations and angular momenta precess around the z-axis. The precession frequencies are [117]:

$$\omega_\pm = \gamma(B \pm \sqrt{B_\mathrm{A}(2B_\mathrm{E} + B_\mathrm{A})}) \,, \tag{5.29}$$

where $B_\mathrm{E} = \beta M_i$ is the exchange field of the respective other sublattice. Positive frequencies signify right-handed precession of the sublattice magnetizations around the z-axis, while negative frequencies signify left handed precession of the sublattice magnetizations around z. The field $\sqrt{B_\mathrm{A}(2B_\mathrm{E} + B_\mathrm{A})} = B_\mathrm{c}$ is the spin flop field. At the spin flop field, both sublattice magnetizations are reoriented so that they are then nearly perpendicular to the z-axis [118]. At external magnetic fields above the spin flop field, the character of the resonant modes drastically changes [119]. We will restrict this discussion to external magnetic fields lower than the spin flop field.

The left handed precession mode is depicted in Fig. 5.8. In contrast to the ferromagnetic resonance mode of the ferrimagnet, the sublattices are not strictly antiparallel during antiferromagnetic resonance. In the right-handed precession mode (+), $\mathbf{M}_1$ is further deflected from the z-axis than $\mathbf{M}_2$ is from the negative z-axis, $\theta_{1+}/(\pi - \theta_{2+}) = \eta$. In the left-handed precession mode (-), $\mathbf{M}_2$ is deflected more, $(\pi - \theta_{2-})/\theta_{1-} = \eta$. The constant η is material dependent and can be calculated from [117]

$$\frac{\eta + 1}{\eta - 1} = \sqrt{(2B_\mathrm{E} + \mathrm{B_A})/B_\mathrm{A}} \,. \tag{5.30}$$

Since in most antiferromagnets $B_\mathrm{E} \gg B_\mathrm{A}$, the sublattices precess nearly antiparallelly, with $\eta \gtrsim 1$. The sublattice magnetization components in the x-y plane are antiparallel, even when antiferromagnetic resonance is excited. Viewed along the z-axis, the sublattices thus rotate with a phase difference of 180 degrees.

The absolute magnitude of the precession cone angles depends, much like in ferromagnetic resonance, on the magnitude of the microwave magnetic field driving the precession and the damping constant α_i. It is approximately [115]

$$\theta_1 = \frac{b_1}{\Delta B} \tag{5.31}$$

where the antiferromagnetic half-width half maximum linewidth ΔB is [115]

$$\Delta B_\pm = \frac{\alpha_i \omega_\pm}{\gamma} \frac{B_\mathrm{E}}{B_\mathrm{A}} \,. \tag{5.32}$$

Comparing this expression with the FMR linewidth $\Delta B = \alpha\omega/\gamma$ of a ferromagnet, we can (analogously to the ferrimagnetic case) define an effective damping constant for the antiferromagnet

$$\alpha_\mathrm{eff} = \alpha_i \frac{B_\mathrm{E}}{B_\mathrm{A}} \,. \tag{5.33}$$

Similarly to the ferrimagnetic case, α_eff is larger than the sublattice damping constants α_i. We can now express the dynamics of the sublattices excited in antiferromagnetic resonance below the spin flop field as:

$$\dot{\mathbf{M}}_{1,\pm} = \gamma_i \mathbf{M}_1 \times (\mathbf{B} \pm B_\mathrm{c}\mathbf{e}_z) \pm \frac{\alpha_\mathrm{eff}}{M_i} \mathbf{M}_1 \times \dot{\mathbf{M}}_1 \,, \tag{5.34}$$

$$\dot{\mathbf{M}}_{2,\pm} = \gamma_i \mathbf{M}_2 \times (\mathbf{B} \pm B_\mathrm{c}\mathbf{e}_z) \mp \frac{\alpha_\mathrm{eff}}{M_i} \mathbf{M}_2 \times \dot{\mathbf{M}}_2 \,, \tag{5.35}$$

where the ratio of the precession cone angles is η.

Antiferromagnetic Spin Pumping

To calculate the pumped spin current, we start from Eq. (5.4)

$$I_s = -\dot{L}_{z,\mathrm{tot}} \frac{\alpha'_\mathrm{eff}}{\alpha_\mathrm{eff}} \,. \tag{5.36}$$

Here, we have introduced the effective spin pumping damping constant which in a compensated antiferromagnet/normal metal interface (where $\alpha'_1 = \alpha'_2$) is

$$\alpha'_\mathrm{eff} = \alpha'_i \frac{B_\mathrm{E}}{B_\mathrm{A}} \,. \tag{5.37}$$

In experiment, α'_{eff} can directly be measured by comparing the linewidth of an antiferromagnet with and without contact to a normal metal layer, analogously to the ferromagnet. We express the spin pumping spin current as the total change in angular momentum in the magnetic system due to spin pumping. Thus

$$I_s = -(\dot{L}_{z,1} + \dot{L}_{z,2})\frac{\alpha'_{\text{eff}}}{\alpha_{\text{eff}}}\,. \tag{5.38}$$

Since the last terms in Eqs. (5.34) and (5.35) are of the same form as in the ferromagnetic case Eq. (5.1), we analogously write for the change in z-direction angular momentum (cf. Eq. (5.7)):

$$\dot{L}_{z,1} = L\sin^2(\theta_1)\alpha_{\text{eff}}\omega\,, \tag{5.39}$$

$$\dot{L}_{z,2} = -L\sin^2(\theta_2)\alpha_{\text{eff}}\omega\,. \tag{5.40}$$

Using Eqs. (5.39) and (5.40), Eq. (5.38) becomes:

$$I_s = -\omega\alpha'_{\text{eff}}L(\sin^2(\theta_1) - \sin^2(\theta_2)) \tag{5.41}$$

Since θ_1 and θ_2 are of similar size (see Eq. (5.30)), the pumped spin current resulting from the antiferromagnetic resonance in an easy-axis antiferromagnet is small relative to spin pumping in a ferromagnet. While the precession frequency ω is typically larger in an antiferromagnet, the precession cone angles tend to be smaller due to the stronger viscous (Gilbert) damping at higher frequency (see Eq. (5.31) and the analogous discussion for the ferromagnetic case in Sect. 2.2). It is also important to note that the product of $\omega\alpha_{\text{eff}}$ can be directly inferred from the antiferromagnetic resonance linewidth $\Delta B = \omega\alpha_{\text{eff}}/\gamma_i$. The resonance linewidth therefore already provides and upper limit for the magnitude of $\omega\alpha'_{\text{eff}}$. To sum up, since the precession cone angles of both sublattices are similar and are expected to be of equal or lower amplitude compared to ferromagnets at the same drive power, while α'_{eff} of an antiferromagnet is similar to the α' of a ferromagnet, we expect less pumped spin current generated via spin pumping in resonantly driven antiferromagnets compared to ferromagnets.

5.2.2 Sample and Experimental Setup

For our experiment we choose MnF_2 as an antiferromagnet. It is a model easy-axis antiferromagnet with the easy axis oriented along the crystalline c-axis [120]. Its

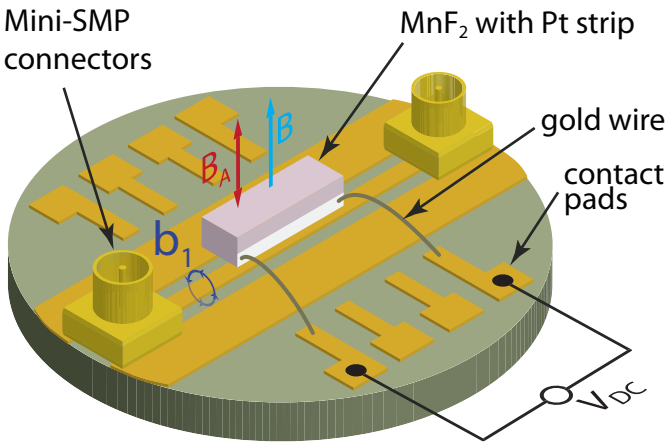

Figure 5.9: Measurement geometry for antiferromagnetic spin pumping: A MnF_2 single crystal with a platinum strip deposited on it is mounted on a coplanar waveguide (CPW) structure. A microwave ac current in the CPW drives antiferromagnetic resonance. The voltage generated by electrically detected spin pumping is measured using contacts at either end of the Pt strip. An external magnetic field is applied along the magnetic easy-axis of the crystal. Image adapted from [116].

exchange field $B_\mathrm{E} \approx 53\,\mathrm{T}$, anisotropy field $B_\mathrm{A} \approx 0.84\,\mathrm{T}$ spin flop field $B_\mathrm{c} \approx 9.5\,\mathrm{T}$ [119,121,122] and Neel temperature $T_\mathrm{N} = 67\,\mathrm{K}$ [123] are well known. Since MnF_2 is a well-understood antiferromagnet, several studies of magnetic resonance have already been performed and can be used as reference [119,121,122].

To enable electrically detected spin pumping, a platinum strip of 210 μm width and 7 nm thickness is deposited on the $0.5 \times 3\,\mathrm{mm}^2$ side of a $3 \times 1 \times 0.5\,\mathrm{mm}^3$ MnF_2 crystal. The easy axis of anisotropy in this crystal is perpendicular to the $1 \times 3\,\mathrm{mm}^2$ side of the crystal. The crystal is then placed onto a copper coplanar waveguide (CPW) structure, as shown in Fig. 5.9. The width of the center conductor is 560 μm The Pt strip is contacted at both sides and the voltage between the contacts is recorded. At both sides of the coplanar waveguide structure, mini-SMP connectors are mounted. Using these connectors, a microwave ac current can be driven in the CPW using a vector network analyzer (VNA). The ac current causes an ac microwave magnetic field around the center conductor of the CPW, driving the antiferromagnetic resonance. The sample and CPW are inserted into a magnet cryostat, enabling us to adjust the temperature in the range of $4\,\mathrm{K} < T < 300\,\mathrm{K}$ as well as apply magnetic fields up to 17 T along the c-axis of the MnF_2 crystal. More details on the experimental

techniques used can be found in Ref. [116].

5.2.3 Results and Discussion

Using the setup described above, we measure the antiferromagnetic resonance absorption and electrically detected spin pumping voltage at a temperature of $T = 4\,\mathrm{K}$. The microwave power provided by the VNA was 11 dBm. The microwave circuits used were able to support ac currents up to 20 GHz. To lower the antiferromagnetic resonance frequency of the left-handed precession mode to below 20 GHz, external magnetic fields $9\,\mathrm{T} < B < 10\,\mathrm{T}$ are applied. In Fig. 5.10(a,b), the microwave transmission $|S_{21}|^2$ measured by the VNA is shown as a function of microwave frequency and applied magnetic field. To account for the frequency dependent performance of the microwave circuit used, a reference value of $|S_{21}(\omega)|^2\,@B = \pm 9\,\mathrm{T}$ is subtracted from the measured data measured at frequency ω, similar to the correction performed in Sect. 4.2.2. A line of greater absorption (darker) is visible, which is the signature of antiferromagnetic resonance. Upon closer inspection, we observe a superposition of several spin wave modes in the bulk of the MnF_2 crystal. The frequency-field dispersion decreases in frequency for magnetic fields lower than the spin flop field $B_c \approx 9.5\,\mathrm{T}$, and then increases again after the spin flop. The dispersion of the antiferromagnetic modes does not reach zero frequency, as would be expected from Eq. (5.29). This is due to a slight misalignment between the external magnetic field and magnetic easy axis. This behavior is well understood and described in more detail in [115, 116, 119]. As expected, the signature of antiferromagnetic resonance does not change under magnetic field inversion.

In Fig. 5.10(c,d), we show the measured dc voltage between the contacts on the platinum strip, as a function of external magnetic field and microwave frequency. As in the $|S_{21}|^2$ data of Fig. 5.10(a,b), $V_{\mathrm{DC}}(\omega)|@B = 9\,\mathrm{T}$ has also been subtracted from the data measured at frequency ω, to account for the frequency dependence of the microwave circuitry. We find the same dispersion as in the transmission spectra also for the measured dc voltage V_{DC}. Upon field inversion, the polarity of the measured voltage does not change. In the model for spin pumping described above, we however expect the spin current, and thus the electrically detected spin pumping dc voltage to change sign upon magnetic field inversion. This is not the case in our data, and therefore we conclude that the observed dc voltage is not due to electrically detected spin pumping.

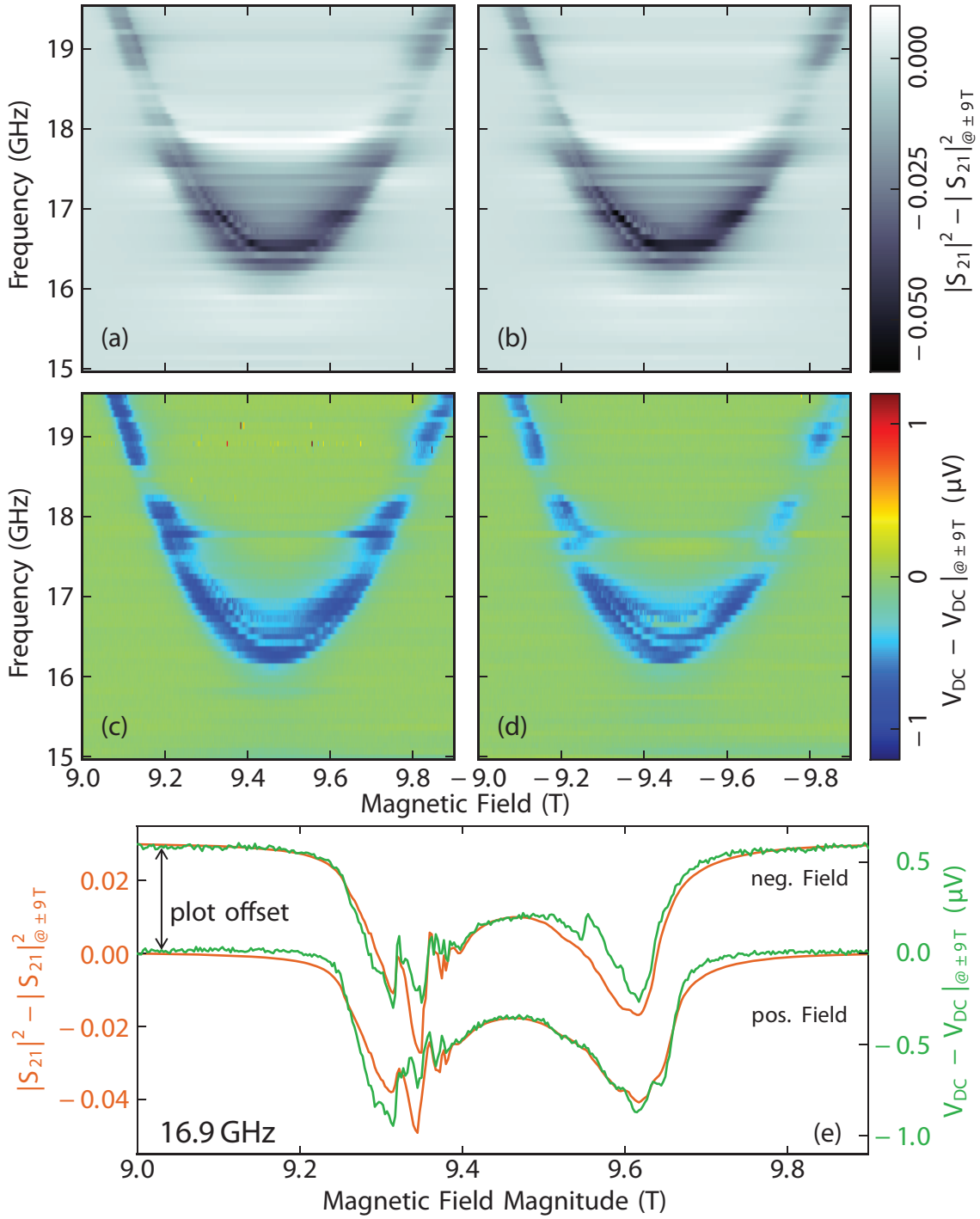

Figure 5.10: Antiferromagnetic resonance (a,b) and electrically detected spin pumping (c,d) in MnF_2 as a function of frequency and applied magnetic field at a temperature of 4 K, presented as a false color plot. A reference value at ±9 T (outside of resonance) is subtracted from the data. (e) Magnetic field cuts of the same data as in (a-d), at a fixed frequency of 16.9 GHz. Image adapted from [116].

In Fig. 5.10(e), we show a magnetic field cut of the data shown in Fig. 5.10(a-d) at a constant fixed frequency of 16.9 GHz. In the microwave transmission data, shown in orange, we observe several spin wave modes both above and below the spin flop field $B_c \approx 9.5\,\mathrm{T}$. The line widths in the region below B_c are around 10 mT, comparable to the resonance lines found in thin film YIG. The microwave absorption due to antiferromagnetic resonance is identical at positive and negative magnetic fields. The peaks in the dc voltage, shown in green, coincide with the peaks in the microwave absorption in the $|S_{21}|^2$ data. The line shape is also very similar, thus the dc voltage is proportional to the absorbed power in antiferromagnetic resonance. As discussed above, the dc voltage does not change polarity when the external magnetic field is inverted, ruling out spin pumping as its source. Instead of spin pumping, the observed dc voltage could be generated by microwave rectification via the spin Hall magnetoresistance (SMR), as discussed in Sect. 5.1.5, which can produce signals similar to spin pumping. To calculate the line shape of these signals as a function of magnetic field direction, first the SMR effect in antiferromagnets would need to be investigated. To the best of our knowledge, there are no such studies published to date. A more thorough treatment of possible sources of the measured dc voltage can be found in [116].

However, the measured voltages for the positive and negative magnetic field sweeps differ slightly. This difference could originate from spin pumping. This difference is smaller than 200 nV, which we can set as an upper limit of the spin pumping voltage generated in our experiment.

Comparing Eq. (eq:afmsperg) with Eq. (5.7) for the ferromagnet we predict the dc voltage generated by spin pumping, analogously to Eq. (2.14) for small precession cone angles,

$$V_{\mathrm{sp}} = e g^{\uparrow\downarrow} \theta_{\mathrm{SH}} \lambda_{\mathrm{SD}} \tanh\left(\frac{t_{\mathrm{N}}}{2\lambda_{\mathrm{SD}}}\right) \frac{\omega}{2\pi} R w \theta_1^2 \left(1 - \frac{1}{\eta^2}\right) . \tag{5.42}$$

Since the spin mixing conductance of most materials are similar, we assume a spin mixing conductance of $g^{\uparrow\downarrow} = 10^{19}\,\mathrm{m}^{-2}$ also for the MnF_2/Pt interface. The ratio of the precession cone angles for MnF_2 is $\eta = 1.19$. To calculate the precession cone angle θ_1, it is necessary to first quantify the ac magnetic field b_1 around the center conductor of the coplanar waveguide structure. We will here perform a rough estimate of b_1. The microwave power output of the VNA on port one in our experiment is $P_{\mathrm{in}} = 13\,\mathrm{mW}$. Off-resonance, the power transmitted is $P_{\mathrm{out}} = |S_{21}|^2 * P_{\mathrm{in}} = 0.01 * P_{\mathrm{in}}$. Assuming

the attenuation of the microwave circuitry from port one of the VNA to the CPW is the same as the one from the CPW to port two of the VNA, that means that the power incident on the CPW structure is $P_{\mathrm{CPW}} = \sqrt{|S_{21}|^2} * P_{\mathrm{in}} = 0.1 * P_{\mathrm{in}} = 1.3\,\mathrm{mW}$. At a system impedance of $50\,\Omega$, the rf current flowing in the CPW is thus calculated to be $I_{\mathrm{CPW}} = 5\,\mathrm{mA}$. Using Biot-Savart's law, the magnetic field directly above the CPW center conductor is calculated to $b_{1,0} = 6\,\mu\mathrm{T}$. A homogeneous magnetic field of this magnitude over the whole sample would yield a precession cone angle $\theta_1 = b_1/\Delta B = 0.0006$ [115], using the linewidth $\Delta B = 10\,\mathrm{mT}$ measured in experiment. Using $R = 1.03\,\mathrm{k}\Omega$, $\lambda_{\mathrm{SD}} = 1.6\,\mathrm{nm}$, and $\theta_{\mathrm{SH}} = 0.06$, the expected spin pumping voltage is $V_{\mathrm{sp}} = 80\,\mathrm{nV}$. Unfortunately, this is lower than the sensitivity achieved in experiment, explaining the lack of an observable spin pumping voltage in our experiment.

5.2.4 Conclusion

In this section, we have developed a model for pumped spin currents in easy-axis antiferromagnets. Based on that model, we predict that pumped spin currents in these antiferromagnets are relatively small as compared to the ferromagnetic case. In the case of MnF_2 it is smaller by a factor of $(1 - 1/\eta^2) = 0.3$.

We have performed an antiferromagnetic resonance and electrically detected spin pumping experiment on a bilayer of MnF_2 and platinum. While we observe a dc voltage when MnF_2 is driven in antiferromagnetic resonance, its signature is not consistent with spin pumping, being invariant under magnetic field inversion. We conclude that the spin pumping voltage generated in our experiment must be smaller than 200 nV. This is consistent with our model, which predicts $V_{\mathrm{sp}} = 80\,\mathrm{nV}$ using our experimental parameters.

In order to observe spin pumping voltages in MnF_2, the antiferromagnetic spin pumping experiment should be performed at higher power, which can be achieved by improving the microwave transmission properties of the microwave cables between the VNA and the CPW structure. Another option is to employ a CPW resonator structure to enhance b_1. In that case, however, the spin pumping measurement is limited to a single frequency. It would also be advantageous to reduce the size of the MnF_2 crystal such that it can fit on the center conductor of the CPW structure, thus optimizing the microwave magnetic field averaged over the whole crystal, boosting the cone angle of the sublattice magnetization precession.

Chapter 6

Spin Hall Magnetoimpedance

It is generally assumed that the spin Hall physics are independent of frequency up to tens or hundreds of GHz. Moreover, even optically detected voltages at THz frequencies [124] have been interpreted in terms of the inverse SHE. Such a fast response of the spin Hall effect appears reasonable, since microscopic models attribute the SHE to spin-orbit coupling. However, no systematic study of θ_{SH} as a function of frequency has been put forward.

Although spin pumping experiments have been performed as a function of ferromagnetic resonance frequency [35, 125], in these measurements a dc spin current is converted into a measurable dc charge voltage by means of the spin Hall effect. The extracted spin pumping voltage thus reflects the dc spin Hall angle, irrespective of ferromagnetic resonance frequency. In contrast, ac spin pumping experiments [15,38] are sensitive to the ac spin Hall angle and the frequency independence of the spin Hall angle at GHz frequencies is implied in the work of Weiler *et al.* [15].

In order to critically test the presumed frequency-independence of spin Hall physics in the GHz frequency range, spin Hall magnetoresistance (SMR) experiments as a function of frequency appear particularly attractive. The characteristic dependence of electrical resistance on the magnetization direction depends quadratically on the spin Hall angle θ_{SH} [29], i.e. on spin Hall physics. The SMR thus is very sensitive to a possible change of the spin Hall effect viz. the spin Hall angle θ_{SH} with frequency.

In this chapter, we first give a brief overview of the spin Hall magnetoresistance mechanism. Then we report on magnetoimpedance on a yttrium iron garnet/platinum (YIG/Pt) bilayer. We measure the magnetoimpedance by applying an ac charge current with frequency $\omega/(2\pi)$ to the bilayer, and investigate how the resistance $R(\omega, \mathbf{M})$ of the bilayer changes both as a function of frequency, and as a function of the ori-

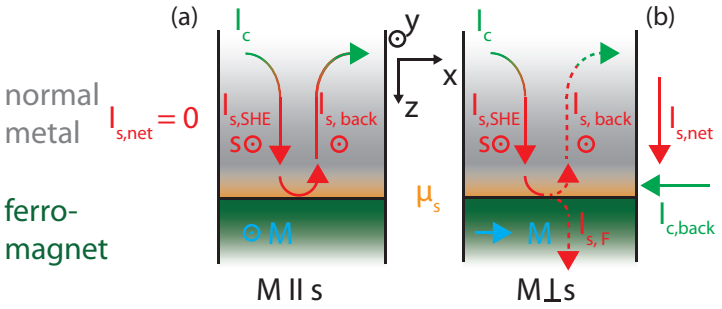

Figure 6.1: The spin Hall magnetoresistance mechanism in a insulating magnet/normal metal bilayer. A charge current I_c is driven in the normal metal layer. Due to the spin Hall effect, a spin current $I_{s,SHE}$ is generated, which flows perpendicularly to the interface. At the interface, a spin accumulation is built up (shown in orange), generating a backflow spin current $I_{s,back}$. (a) If the magnetization of the magnetic film is parallel to the spin current polarization (along y), no spin current can cross the interface. Then, in steady state $I_{s,SHE} = I_{s,back}$, no net spin current flows. (b) If the magnetization of the magnetic film is perpendicular to the spin current polarization, a spin current can cross the interface. This results in a net spin current $I_{s,net}$ in the normal metal even in steady state. The conversion of $I_{s,net}$ to a charge current via the inverse spin Hall effect is measured as a resistance increase of the normal metal layer.

entation of the magnetization **M** in the YIG film. Our data, recorded at room temperature, invariably and quantitatively exhibit the evolution of the resistance with magnetization orientation characteristic of SMR for charge current frequencies from dc to 3 GHz. In other words, the magneto-resistive response of our YIG/Pt bilayer (viz. the SMR effect) does not depend on frequency to within experimental accuracy up to frequencies of at least 3 GHz. Moreover, our data suggests that the SMR prevails up to 8 GHz (the highest frequency used in our experiment), but a quantitative evaluation is precluded by calibration issues.

From a more applied perspective, this experiment also tests the viability of the SHE for high-frequency all-electrical spin current generation, and for SMR-based fast readout of the magnetization orientation of an insulating ferromagnet, which is desirable for use in spintronic devices. The work presented in this chapter is published in Ref. [126].

6.1 Mechanism of Spin Hall Magnetoresistance

We will in this section motivate the orientation dependence of the SMR resistance as well as the dependency of the magnetoresistance ratio on θ_{SH}^2. A more rigorous derivation of the SMR effect is available in Ref. [29]. The spin Hall magnetoresistance was discovered only recently [27] in YIG/Pt bilayers, but is observable in any normal metal/ferromagnetic insulator (N/F) bilayer [28]. Here, the resistance of the normal metal film depends on the orientation of the magnetization in the ferromagnetic insulator. The mechanism is shown in Fig. 6.1. A charge current $\mathbf{I}_\mathrm{c}$ is driven in the N layer along the x-direction, parallel to the N/F interface. As we have already discussed in Sect. 2.3.1, the spin Hall effect (SHE) then causes a spin current $\mathbf{I}_\mathrm{s,SHE}$ in z-direction, with a polarization $\mathbf{s}$ along the y-axis. If the spin current cannot pass the N/F interface, a spin accumulation $\boldsymbol{\mu}_s$ will build up at the interface. This spin accumulation is proportional to the spin current generated by the spin Hall effect, and thus to the spin Hall angle θ_SH. The spin accumulation will cause a backflow spin current $\mathbf{I}_\mathrm{s,back}$ in a direction opposite to the SHE spin current. In steady state, this spin current will be of equal magnitude as the SHE spin current. Thus the net spin current in the N layer is zero.

However, the mechanism of spin transfer torque [8–10] can cause a spin current $\mathbf{I}_\mathrm{s,F}$ to be absorbed by a F at the N/F interface, thereby exciting the magnetization in the F. The interface spin current depends on the relative orientations of the polarization of the spin current accumulation $\mathbf{s}$ and the magnetization (with the magnetization unit vector $\mathbf{m}$), as well as and the interface quality [127]:

$$\mathbf{I}_\mathrm{s,F} \propto g^{\uparrow\downarrow}\mathbf{m} \times (\mathbf{m} \times \boldsymbol{\mu}_\mathrm{s}) \,, \tag{6.1}$$

Equation (6.1) shows that if the magnetization in the F is parallel to $\boldsymbol{\mu}_\mathrm{s}$, then the interface spin current vanishes. This is the situation depicted in Fig. 6.1(a). However, if $\mathbf{m}$ is perpendicular to $\boldsymbol{\mu}_\mathrm{s}$, a spin current will cross the interface. This situation is depicted in Fig. 6.1(b). Here, the spin accumulation is reduced relative to the situation of Fig. 6.1(a), due to the additional interface spin current. This means that the backflow spin current $\mathbf{I}_\mathrm{s,back}$ is also reduced. Then, even in steady state $\mathbf{I}_\mathrm{s,back} < \mathbf{I}_\mathrm{s,SHE}$. The difference between $\mathbf{I}_\mathrm{s,back}$ and $\mathbf{I}_\mathrm{s,SHE}$ is proportional to the spin current accumulation at the interface and thus θ_SH. This net spin current $\mathbf{I}_\mathrm{s,net}$ in N will be converted by the inverse spin Hall effect (ISHE) to a charge current $\mathbf{I}_\mathrm{c,back}$,

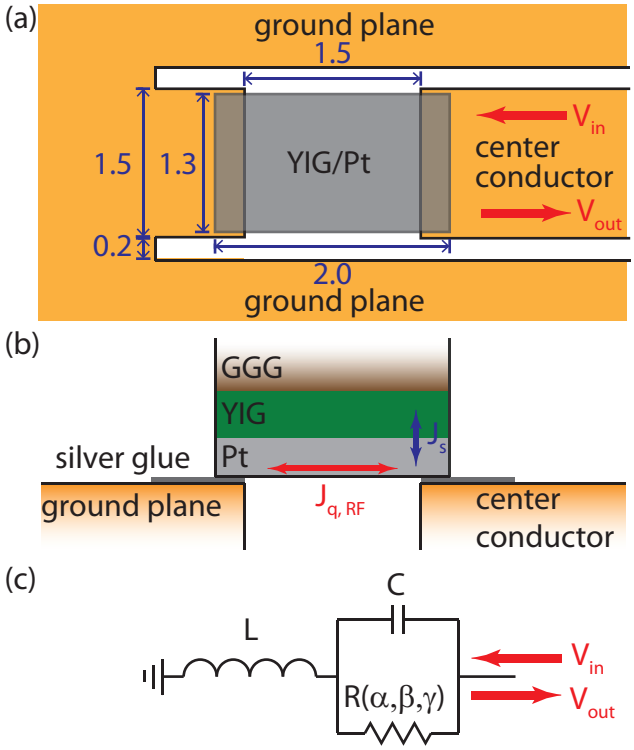

Figure 6.2: (a,b) YIG/Pt bilayer bridging a gap in the Cu center conductor of a coplanar waveguide (CPW) structure shown in (a) top view, (b) cross-sectional drawing along the center conductor. The dimensions shown are given in mm. (c) The equivalent electrical circuit model used to describe the YIG/Pt bilayer on the CPW.

which flows oppositely to the original charge current $\mathbf{I}_{\mathrm{c}}$. $\mathbf{I}_{\mathrm{c,back}}$ is proportional to $\mathbf{I}_{\mathrm{s,net}} \propto \theta_{\mathrm{SH}}$, with an additional proportionality to θ_{SH} due to the ISHE. Overall the $\mathbf{I}_{\mathrm{c,back}}$ is therefore proportional to θ_{SH}^2. $\mathbf{I}_{\mathrm{c,back}}$ effectively reduces the current flowing in the N layer thus enhancing its resistance, which is thus dependent on θ_{SH}^2 and the orientation of the magnetization of the ferromagnet.

6.2 Sample and Experimental Setup

The YIG/Pt bilayer was fabricated by Stephan Grprägs at the WMI by growing a 55 nm thick YIG film on a (111)-oriented single-crystalline gadolinium gallium garnet substrate using laser-MBE [28, 81]. Without breaking the vacuum, the sample was subsequently transferred to an electron beam evaporation chamber and a Pt film with a thickness of 4 nm was deposited onto the YIG. More details on the sample

preparation procedure are given in Ref. [28].

To measure the spin Hall magnetoresistance at high frequencies, as a first step a test fixture is designed which enables the flow of a microwave current in the Pt layer. The bilayer is therefore integrated into a coplanar waveguide (CPW) structure, which consists of a copper ground plane and a copper center conductor, which are separated by thin gaps in the copper. This structure is patterned on a printed circuit board using photolithography at the WMI. Depending on the dimensions of the center conductor and ground plane, as well as the substrate thickness, the characteristic impedance of such a device can be tailored to be $50\,\Omega$, enabling broadband microwave experiments and ideal rf current transmission. The easiest way to integrate the Pt layer into the CPW structure is to replace a part of the center conductor, which caries the current, with the Pt film of the YIG/Pt bilayer allowing the rf current to flow through the Pt. To that end, a hole is cut out of the center conductor. Subsequently, this hole is bridged with the YIG/Pt bilayer that is glued onto the sample chip using silver glue, with the Pt layer facing the CPW center conductor

There are two possible ways to measure the impedance at microwave frequency: reflection and transmission measurements. For transmission measurements, the CPW structure needs to be contacted with microwave connectors at the input and output port. For the reflection measurement, only one connector needs to be used, while the other end of the CPW center conductor is connected to the ground plane. It was found in test experiments that the frequency dependent microwave transmission/reflection spectra improved in quality when shorter sections of CPW were used. This is due to the fact that on CPW structures standing wave resonances occur. The shorter the CPW structure is, the higher is the frequency of the lowest-frequency resonance. Since the transmission and reflection changes strongly near resonant frequencies, the measurement sensitivity for small changes in transmission/reflection is reduced, when electrical resonances occur. Shorter CPWs are more easily realized with the reflection type measurements, since each connector needs a certain length of CPW and reflection type measurements require only one connector. We were able to reduce the length of the CPW from the connector to the connection to the ground plane to just 8 mm. The dimensions of the structure used in the experiment described here is as follows: The width of the center conductor of the CPW is 1.5 mm, with a gap of 0.2 mm to the ground planes. The center conductor is interrupted by a $1.5 \times 1.5\,\mathrm{mm}^2$ square gap in the PCB board. We diced a rectangular piece with lateral dimensions of

$2 \times 1.3\,\mathrm{mm}^2$ from the as grown YIG/Pt sample, which is bridging the gap in the CPW structure. This setup is schematically shown in Fig. 6.2(a,b). A smaller structure would still enhance higher frequency operation. However, very small sample sizes are then required that are very difficult to manually position on, and attach to, the center conductor.

The ac current is injected using a surface mount mini-SMP connector at one end of the CPW structure. It is important that the microwave cables leading to the connector are not touched or moved during the measurements, as this causes spurious signals in our microwave reflection measurement that overlay SMR signal. The CPW/sample chip is thus mounted between the pole shoes of a rotatable electromagnet, and is not moved itself. We mounted the sample chip in three different ways (see Figs. 6.5(a, e, i)): In the in-plane (ip) configuration, the magnet rotation axis is parallel to the film normal, so that the magnetic field is always in the plane of the YIG/Pt bilayer. The magnetic field direction is parametrized by the angle α between the charge current direction and the magnetic field direction. In the oopj configuration the rotation axis of the magnetic field is parallel to the current direction, with the angle β between the magnetic field and the film normal. In the oopt configuration, the rotation axis lies in the film plane, perpendicular to the current direction. The oopt angle γ is enclosed by the magnetic field direction and the film normal.

We measure the evolution of the SMR as a function of the orientation α, β, and γ of the magnetic field. Strictly speaking, the resistance in SMR measurements is however not dependent on the external magnetic field orientation (parametrized by α, β, and γ), but rather the orientation of the magnetization in the YIG film. We use a magnetic field magnitude of 0.6 T in our experiments. In the ip configuration, the magnetization is to very good approximation parallel to the external magnetic field, since the magnetic anisotropy field(s) in the YIG film plane are much smaller than the applied external field. However, due to shape anisotropy in the thin YIG film, this is not the case for the out-of plane rotations. In the following we derive the magnetization orientation as a function of the external magnetic field assuming that the magnetization of the sample corresponds to one single magnetic domain, in a so-called Stoner-Wohlfarth approach. Here, the equilibrium magnetization orientation is determined by the magnitude and direction of the externally applied magnetic field $\mathbf{H}$ and the anisotropies stemming from the shape or the crystalline properties of the sample. Following Ref. [39], we use a free energy approach to calculate the direction

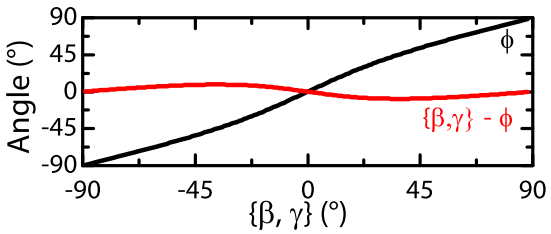

Figure 6.3: Simulation: the angle ϕ between the magnetization $\mathbf{M}$ of the YIG film and the film normal (black line) and the angle between the external magnetic field $\mathbf{H}$ and the magnetization (red line) as a function of the out-of-plane angles β, γ, as defined in Fig. 6.5. The magnitude of the external magnetic field is 0.6 T.

of the magnetization vector. The free energy density for a thin YIG film is taken as

$$F_{\text{tot}} = F_{\text{Zeeman}} + F_{\text{shape}} \,, \tag{6.2}$$

where $F_{\text{Zeeman}} = -\mu_0 \mathbf{M} \cdot \mathbf{H}$ is the Zeeman energy density and $F_{\text{shape}} = 1/2\mu_0 M_{\text{sat}}^2 \cos^2(\phi)$ is the shape anisotropy energy density for the oopj and oopt rotations, which depends on the saturation magnetization M_{sat} of the magnetic material as well as the angle ϕ between the magnetization and the film normal. Since YIG does not feature any strong magnetocrystalline anisotropies [120], only shape anisotropy needs to be considered. A minimization of F_{tot} with respect to magnetization angle ϕ yields the equilibrium orientation of the magnetization which is shown as a function of the out of plane external magnetic field angles β and γ in Fig. 6.3. For our simulation, we used the saturation magnetization of YIG, $M_{\text{sat}} = 143\,\text{kA/m}$ [120] and an external magnetic field of 0.6 T. We find that the angle between the external magnetic field and the magnetization is less than ten degrees using an external magnetic field of 0.6 T, at all out of plane angles. We will thus present our SMR data as a function of external field orientation (the quantity varied in experiment) rather than magnetization.

6.3 Reflection Measurement of the Impedance

The sample that is integrated into the CPW structure constitutes a load that is not equal to the system impedance $Z_0 = 50\,\Omega$. Therefore, part of the ac current is reflected at the sample. Measuring this reflection allows us to extract the impedance of the sample [128]. The reflection of the sample is recorded using a vector network analyzer

(VNA) which records the complex scattering parameter [129]

$$S_{11} = \frac{V_1^-}{V_1^+}\,, \tag{6.3}$$

where V_1^+ is the voltage driven into the sample and V_1^- is the voltage reflected from the sample. Since both voltages have a phase, the scattering parameter is complex-valued.

The scattering parameter S_{11} depends on the impedance as [129]

$$S_{11}(Z) = \frac{Z - Z_0}{Z + Z_0}\,. \tag{6.4}$$

The measured reflection is most sensitive to changes in impedance close to the characteristic impedance $Z_0 = 50\,\Omega$ of the system. Here, a small change in impedance leads to a relatively large change in S_{11}, while the absolute value of S_{11} is small. The sample used in our experiments has a resistance of $R_0 = 97\,\Omega$, more than the ideal value for optimal sensitivity. However, because the aspect ratio of the sample is determined by the CPW on which it is mounted, the resistance can only be adjusted by increasing the Pt layer thickness. This in turn will decrease the SMR ratio observed [28, 29]. The Pt layer thickness of 4 nm is nearly ideal for the amplitude of the SMR, while the resulting $R_0 = 97\,\Omega$ still results in a good sensitivity to a change of impedance, and is therefore a good compromise for high frequency SMR measurements.

6.3.1 Microwave Calibration of the Setup

To accurately measure S_{11}, the setup needs to be calibrated. In microwave cables, the microwave signal is typically damped by $0.2 - 1\,\mathrm{dB/m}$, depending on frequency and cable quality. There are also several connectors in the measurement setup, at the port of the VNA, between different cables leading to the sample as well as the mini-SMP connector at the sample itself. At all of these connections there are slight impedance mismatches, leading to reflections in the feedline. Lastly, on the sample chip itself, between the mini-SMP connector and the sample there is also an impedance mismatch. All of these effects affect the measured S_{11} and need to be accounted for in a calibration. We now describe the calibration protocol used in our experiments. The calibration of our reflection measurement is performed in such a way that the calibration plane is as close to the sample as possible, as we expect a significant

impedance mismatch at the transition from the semi-rigid microwave cable to the CPW structure. This impedance mismatch takes place at the mini-SMP connector itself and on the printed circuit board at the interface to the mini-SMP connector. To focus on our sample properties, we include these sources of mismatch in the calibration procedure and thus obtain a calibration plane right at our sample. To achieve this, homemade rather than commercial high-precision calibration standards have to be used. Although the homemade calibration standards are of inferior quality compared to their commercial counterparts, we profit from the fact that the plane of reference is moved beyond the last set of connectors, resulting in an improved measurement accuracy.

Assessing the quality of our calibration standards through a direct measurement would be very difficult, because we have no way to calibrate such a reference experiment. We can however try to quantify the deviation of our measurement standards from the ideal. For calibration, we use three calibration standards: open, short, and load [130].

For the open calibration standard we employ an empty sample carrier. It features a capacitance to ground across the gap where the sample is placed during the actual experiment, which is however only of the order of 0.1 fF, corresponding to an impedance of 531 kΩ at 3 GHz. The open calibration standard should thus not lead to an appreciable calibration error.

For the short calibration standard, we connect the center conductor to the ground plane using three aluminum wire bonds of 25 μm diameter at either side for a total of six bonds in parallel. These bond wires have a length of about 0.4 mm. The impedance of these wires consists of a resistance and an inductance, as well as a capacitance, where the latter however is small [131]. The resistivity of Al is 2.65 $\mu\Omega$ cm, which results in a bond resistance of 5 mΩ. This increases with frequency due to the skin effect. The skin depth of Al at 10 GHz is $\delta = 0.88\,\mu$m, which leads to an increase in resistance to a total of 85 mΩ, which is still insignificant. The inductance of a wire with 25 μm diameter and a length of 0.4 mm can be calculated [132] to be 0.275 nH. Since there are six bond wires in parallel, the total inductance is lowered, but cannot simply be divided by six, due to coupling between the bonds [131]. If we estimate a total inductance of 0.1 nH, the resulting reactance $X_L = \omega L$ at 3 GHz is 1.9 Ω. Thus the short calibration standard is not perfect and thus introduces an error into the calibration. We calculate that the use of a calibration standard with an impedance

$Z = 1.9\,\Omega$ instead of an impedance $Z = 0\,\Omega$ introduces an error in the order of 10 % in a reflection measurement, where $S_{11} = (Z - Z_0)/(Z + Z_0)$. $Z_0 = 50\,\Omega$ is the characteristic impedance of the microwave circuit.

The $50\,\Omega$ load calibration standard is realized by two Vishay CH02016-100RGF $100\,\Omega$ thin film microwave resistors placed in parallel at either side of the center line connecting it to the ground plane. The reactance of these elements is shown to be much smaller than their resistance up to frequencies of about 10 GHz. The accuracy of the resistance of these resistors is rated at 2 %, which is smaller than the error expected from the short standard.

6.3.2 Calculation of the SMR Resistance from Microwave Reflection

To extract the magnetization orientation dependent resistance R of the YIG/Pt bilayer from the measured scattering parameter S_{11} (corrected using the calibration data), it is converted to the complex impedance Z of the sample via

$$Z(\omega) = \frac{Z_0(1 + S_{11}(\omega))}{1 - S_{11}(\omega)}\,, \tag{6.5}$$

where $Z_0 = 50\,\Omega$ is the characteristic impedance of the system. To extract the magnetization orientation dependent resistance R of the YIG/Pt bilayer from the complex impedance, we use the circuit model sketched in Fig. 6.2(c). L and C hereby are an inductance and a capacitance, respectively, taken as frequency independent constants. This model is consistent with models applied to surface mount resistors [133]. The impedance of this L-R-C circuit shown in Fig. 6.2(c) is given by

$$Z(\omega) = \frac{1}{R\left(C^2\omega^2 + \frac{1}{R^2}\right)} + i\left(\omega L - \frac{C\omega}{C^2\omega^2 + \frac{1}{R^2}}\right)\,. \tag{6.6}$$

In a first step, we calculate $Z(\omega)$ from the measurement data via Eq. (6.5). We then simultaneously fit $\Re(Z)$ and $\Im(Z)$ with Eq. (6.6), using R, L, and C as fit parameters. Since at higher frequencies electrical circuit resonance phenomena occur, which cannot be reproduced by the equivalent circuit model, only the part of $Z(\omega)$ with $\omega/(2\pi) < 3\,\mathrm{GHz}$ is included in the fit.

This is exemplarily illustrated in Fig. 6.4, where the real and imaginary parts of the complex impedance as well as the fit according to Eq. (6.6) (green line) are plotted

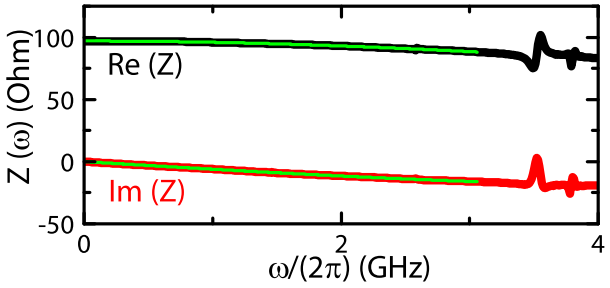

Figure 6.4: $Z(\omega)$ recorded for $\mu_0|\mathbf{H}| = 0.6\,\mathrm{T}$ and $\alpha = -90°$ in the ip rotation measurement. Both are fitted simultaneously with Eq. (6.6) (green line), yielding the capacitance $C = 0.2\,\mathrm{pF}$ and inductance $L = 1\,\mathrm{nH}$ of the equivalent circuit of Fig. 6.2(c).

for the measurement with the external field in the film plane. For both the oopj and oopt rotation the data and fit look very similar. For all 3 rotation planes we find that $C = 2 \times 10^{-13}\,\mathrm{F}$ and $L = 1 \times 10^{-9}\,\mathrm{H}$ consistently describe the data. We did not find L or C to be magnetization orientation dependent. The parameter R is found from the fit to be $R = 97\,\Omega$, corresponding to the measured dc resistance of the device.

The total resistance R consists of two components: the resistance R_0 of the Pt film which is independent of frequency and magnetic field, and R_1, which is magnetization orientation dependent. The (possible) frequency dependence of R_1 is the key focus of this chapter. R_1 can be taken as small compared to R_0, because the magnetoresistance ratios R_1/R_0 measured in YIG/Pt are smaller than 10^{-2} [27, 28, 134, 135]. Using L and C, we can in a second step calculate the magnetization orientation dependent resistance from the measured impedance by solving Eq. (6.6) for R:

$$R(\omega, \{\alpha, \beta, \gamma\}) = \frac{\sqrt{L^2\omega^2 - |Z(\omega, \{\alpha, \beta, \gamma\})|^2}}{\sqrt{C^2\omega^2\left(|Z(\omega, \{\alpha, \beta, \gamma\})|^2 - L^2\omega^2\right) + 2LC\omega^2 - 1}}\,. \tag{6.7}$$

$R(\omega, \{\alpha, \beta, \gamma\})$ includes the frequency and magnetic field independent dc resistance R_0 of the platinum and the magnetization orientation dependent resistance R_1. Since the values of L and C are only reliably determined for frequencies of $\omega/(2\pi) < 3\,\mathrm{GHz}$, the extraction of $R(\omega)$ at frequencies $\omega/(2\pi) > 3\,\mathrm{GHz}$ cannot be relied on quantitatively.

6.4 Results

To establish a reference for the ac resistance measurements, we first measured the dc resistance as a function of the magnetic field orientation at a fixed magnetic field magnitude $\mu_0 H = 0.6\,\mathrm{T}$ for all three magnetic field rotation configurations. In these experiments, a constant bias charge current is applied to the CPW strip with a Keithley 2400 sourcemeter, and the resistance is calculated from the voltage drop.

In a second set of experiments, we measured the complex reflection coefficient S_{11} with an Agilent N5242A vector network analyzer (VNA) as a function of frequency $f = \omega/(2\pi)$, and as a function of the magnetic field orientation angles α, β, and γ. Again, the magnetic field magnitude hereby was 0.6 T. More precisely, for each measured magnetic field orientation, the frequency of the VNA microwave drive signal is swept, and the corresponding $S_{11}(\omega)$ recorded. Then the magnetic field is rotated to the next orientation, $S_{11}(\omega)$ is recorded, etc.

In Fig. 6.5, we show the ac magnetoresistance obtained from our measurements for the three rotation planes. This figure is organized as follows: there are 4 panels for each rotation plane, respectively: in (a,e,i) we show a sketch of the measurement geometry for the three rotation planes and the rotation angle of the external magnetic field. In (b,f,j) we show the frequency dependent resistance averaged over all N magnetization orientations studied in a given magnetic field rotation plane

$$\widetilde{R}(\omega) = \frac{1}{N}\sum_{i=1}^{N} R(\omega, \{\alpha_i, \beta_i, \gamma_i\}) \tag{6.8}$$

as a function of ac current frequency.

Panels (c,g,k) show the resistance modulation ΔR,

$$\Delta R(\omega, \{\alpha, \beta, \gamma\}) = R(\omega, \{\alpha, \beta, \gamma\}) - \widetilde{R}(\omega)\,, \tag{6.9}$$

as a function of both frequency and magnetic field angle in a false color plot, while ΔR traces recorded at selected frequencies are depicted in panels (d,h,l).

Due to calibration issues for $\omega/(2\pi) > 3\,\mathrm{GHz}$, the resistance calculated from Eq. (6.7) diverges at certain frequencies corresponding to standing wave resonances arising from reflections at the interface of the CPW structure and the sample. These background oscillations are suppressed in ΔR, which makes it possible to plot ΔR in the false color plots of Figs. 6.5(c,g,k) using the same color code over the whole frequency range

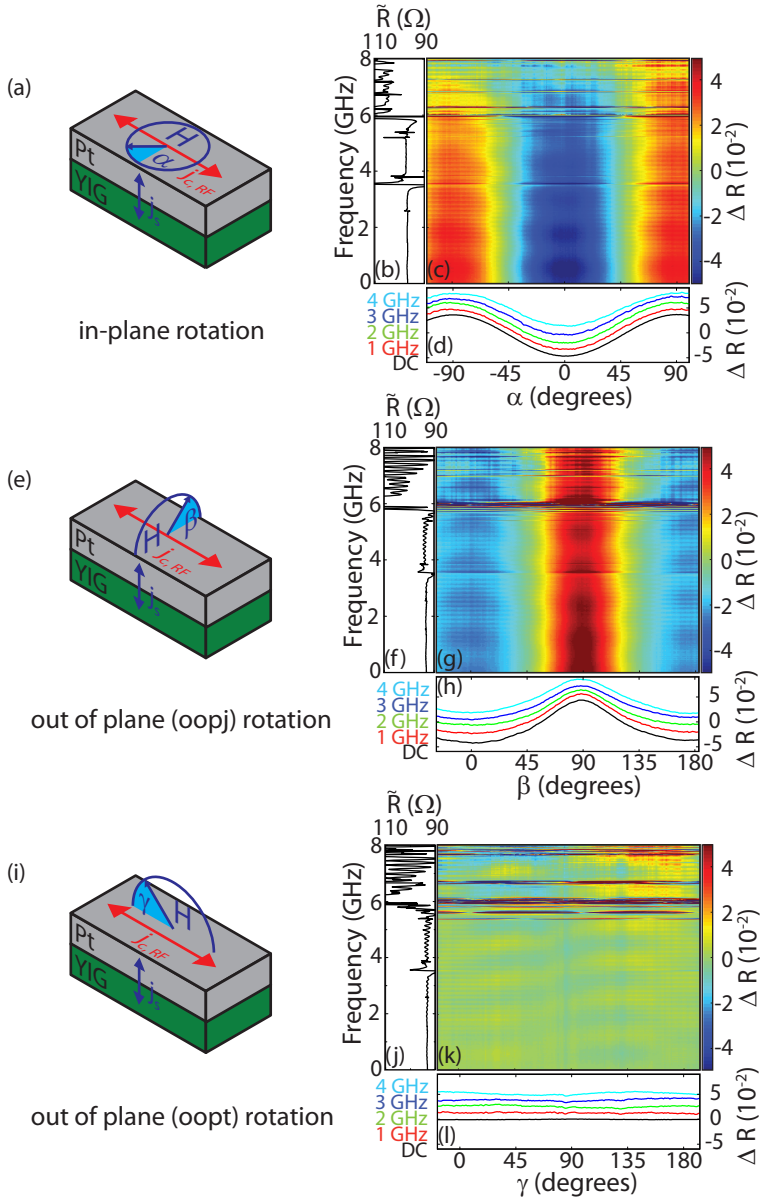

Figure 6.5: Frequency dependent resistance for the ip, oopj, and oopt rotation planes. (a,e,i) A sketch of the YIG/Pt bilayer and the external magnetic field relative to the applied bias current direction. α parametrizes the angle of the magnetic field in the ip rotation, β in the oopj rotation, and γ in the oopt rotation. (b,f,j) $\widetilde{R}$ (Eq. (6.8)) from frequencies of dc to 8 GHz for the respective magnetic field rotations. (c,g,k) The resistance modulation ΔR with respect to ac current frequency and the corresponding magnetic field rotation angles at a constant external magnetic field of $\mu_0|\mathbf{H}| = 0.6\,\mathrm{T}$. (d,h,l) ΔR as a function of the respective rotation angles at different, fixed frequencies: dc (black line), 1 GHz (red line), 2 GHz (green line), 3 GHz (blue line), 4 GHz (light blue line). The ΔR curves are offset for clarity.

used in experiment.

We first analyze the change in dc resistance as a function of the magnetization orientation. For a (dc) SMR-like behavior [28, 135], we expect a $\cos^2(\alpha)$-like resistance modulation with amplitude R_1 on a constant offset R_0 upon rotating the magnetization in the film plane:

$$R_{\mathrm{ip}}(\alpha) = R_0 + R_1 \cos^2 \alpha \,. \tag{6.10}$$

The ratio

$$\frac{R_1}{R_0} = \frac{2\theta_{\mathrm{SH}}^2 \lambda_{\mathrm{SD}}^2 \rho t^{-1} G_{\mathrm{r}} \tanh^2(\frac{t}{2\lambda_{\mathrm{SD}}})}{1 + 2\lambda_{\mathrm{SD}} \rho G_{\mathrm{r}} \coth(\frac{t}{\lambda_{\mathrm{SD}}})} \tag{6.11}$$

depends on the spin Hall angle θ_{SH}, the resistivity ρ of the Pt, the spin diffusion length λ_{SD}, the real part of the spin mixing interface conductance G_{r} [29], and the thickness t of the Pt film. As usually done in the literature [27, 28, 134, 135], we here take all of these parameters as constants, independent of frequency and magnetic field. We furthermore assume that θ_{SH} is purely real. For the oopj rotation, we expect

$$R_{\mathrm{oopj}}(\beta) = R_0 + R_1 \cos^2 \beta \,. \tag{6.12}$$

In the oopt rotation, the SMR is independent of the magnetization orientation [29] with

$$R_{\mathrm{oopt}} = R_0 + R_1 \,. \tag{6.13}$$

The black lines in Figs. 6.5(d,h,l) show the change in resistance $\Delta R(dc)$ for $\mu_0|\mathbf{H}| = 0.6\,\mathrm{T}$ as a function of the angle. The characteristic $\cos^2(\alpha)$-dependence of Eq. (6.10) is clearly evident in Fig. 6.5(d) as well as the expected $\cos^2(\beta)$ type modulation of Eq. (6.12) for the oopj rotation in Fig. 6.5(h). In the latter case, the $\cos^2(\beta)$ modulation is not ideal, which is attributed to shape anisotropy: In Fig. 6.6, we compare the normalized dc ΔR data from Fig. 6.5(h) to $\cos^2(\phi(\beta))$ and $\cos^2(\beta)$, where ϕ is the angle between the magnetization and the film normal simulated in Sec. 6.2. For the calculation of $\cos^2(\phi(\beta))$, we used the $(\phi(\beta))$ data calculated for YIG from Fig. 6.3. In both the $\cos^2(\phi(\beta))$ and the experimental data, we see the same deviation from $\cos^2(\beta)$. We note also that the computed MR ratio, $max(\Delta R) - min(\Delta R)/R_0$ is not affected by the deviation of the magnetization orientation from the external magnetic field orientation. At $\beta = 0°$ and $\beta = 90°$, the orientations where the extrema of the resistance, $max(\Delta R)$ and $min(\Delta R)$, are reached, the magnetization and external magnetic field are aligned ($\beta = \phi$). Last but not least, for a rotation of the 0.6 T

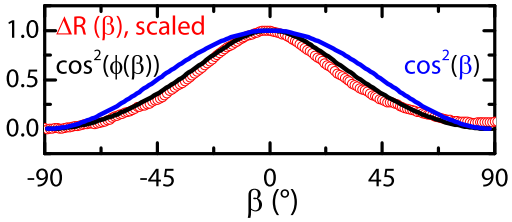

Figure 6.6: Comparison of $\cos^2(\phi(\beta))$ (black line), $\cos^2(\beta)$ (blue line) and the normalized dc ΔR data of Fig. 6.5(h) (red dots) as a function of the oopj magnetic field angle β. For $\phi(\beta)$, we use the simulated data shown in Fig. 6.3.

magnetic field in the oopt rotation plane, the resistance is constant (Fig. 6.5(l)), as expected from Eq. (6.13). Since the magnetization orientation in this rotation plane does not affect the magnetoresistance, the angle between the magnetization and the external magnetic field is not relevant.

Thus the observed angular dependence is the one expected from the SMR effect according to Eqs. (6.10)-(6.13). The dc resistance $R_0 = 97\,\Omega$ and a resistance modulation amplitude $R_1 = max(\Delta R) - min(\Delta R) = 0.083\,\Omega$ yield a MR ratio of $R_1/R_0 = 8.6 \times 10^{-4}$. Using the parameters $\theta_{\mathrm{SH}} = 0.11$, $\lambda_{\mathrm{SD}} = 1.5\,\mathrm{nm}$, $G_{\mathrm{r}} = 4 \times 10^{14}\,\Omega^{-1}\,\mathrm{m}^2$ [28, 57] and the thickness of the Pt film of $t = 4\,\mathrm{nm}$, one expects a dc SMR magnitude of $R_1/R_0 = 7.7 \times 10^{-4}$ from Eq. (6.11), in good agreement to the MR ratio measured experimentally.

We find that the phenomenology of the magnetoresistance observed does not change when making the transition from dc to ac bias currents. In the ip rotation of the external magnetic field, shown in Fig. 6.5(c), we find a modulation of the resistance with a $\cos^2(\alpha)$ dependency, regardless of the ac current frequency, up to at least 3 GHz. Similarly, the oopj data (Fig. 6.5(g)) show a $\cos^2(\beta)$ dependency, while in the oopt orientation (Fig. 6.5(k)) the resistance is independent of magnetization orientation. In Figs. 6.5(d,h,l), we compare the change in resistance with respect to the applied magnetic field angle at dc as well as 1 GHz, 2 GHz, 3 GHz, and 4 GHz ac currents: the curve shape and the amplitude of the modulation is the same, irrespective of frequency. Qualitatively, this modulation persists at frequencies higher than 3 GHz. However, due to the homemade calibration standards and CPW structures, the resistance extraction becomes increasingly unreliable above 3 GHz. Plotting the MR ratio as a function of frequency in Fig. 6.7, we observe oscillations with frequency: there are fast oscillations, with a period of 0.15 GHz and slower oscillations of greater

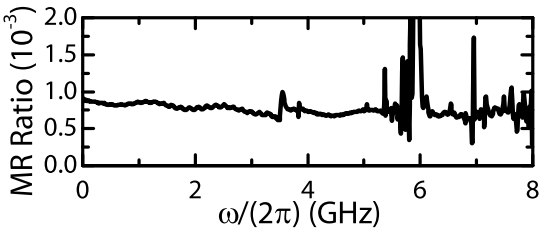

Figure 6.7: The MR ratio R_1/R_0 as a function of frequency for the oopj rotation.

amplitude, with a period of 1.2 GHz. Furthermore, at frequencies above 3 GHz, where electrical circuit resonances occur, the MR ratio diverges. However, no overall trend of the MR ratio is apparent, suggesting that the oscillations and divergences are only due to imperfect calibration rather than a time constant present in the SMR effect. In the latter case a decrease of the MR ratio with frequency is expected, as the system could no longer follow the periodic modulation of the charge current. The amplitude of the slower oscillations at frequencies of less than 3 GHz is 10^{-4}, from which we can estimate the experimental uncertainty to be $1 \times 10^{-4}/8.6 \times 10^{-4} \approx 12\%$. This value is comparable to the one we estimate from calibration uncertainty of the short standard. We thus find that the phenomenology of the SMR can be described up to frequencies of at least 3 GHz with real, frequency independent values for L, C, R, as well as θ_{SH}, of which only the resistance R is magnetization orientation dependent.

6.5 Conclusions

The fact that the SMR effect persists up to at least $\omega/(2\pi) = 3\,\mathrm{GHz}$ means that the interaction time constants $\tau = 1/\omega$ relevant for the SMR effect are shorter than 53 ps. Since the SMR requires both the spin Hall effect and spin torque transfer [29,136,137], i.e. spin-orbit interaction, this can be compared with the spin-orbit interaction time τ_{SO} in platinum. In the free electron model $(2\pi\tau_{\mathrm{SO}})^{-1}$ is estimated to be in the hundreds of GHz [138], and much shorter τ_{SO} are inferred from spin injection viz. spin transport experiments [139]. A constant SMR magnitude up to tens of GHz thus appears reasonable.

From a more applied perspective, our experiments show that the SMR can be used to read out the orientation in a ferromagnetic insulator such as YIG electrically in about 50 ps.

In summary, we have measured the SMR effect in a YIG/Pt bilayer, using currents

with frequencies from dc up to 8 GHz. We can describe our results with a simple L-R-C circuit model with frequency independent constants, of which only the resistance R is magnetization dependent. We find a SMR amplitude (magnetoresistance ratio) of 8.6×10^{-4}, which is unaltered from dc up to frequencies of several GHz. This implies that the spin Hall physics and θ_{SH} in particular enabling the SMR effect are frequency independent within experimental accuracy up to frequencies of at least 3 GHz. This is consistent with theoretical work proposing that the time constants of the SMR should be governed by the spin-orbit interaction.

Chapter 7

Summary

This thesis deals with spin currents in ferrimagnet/normal metal bilayers. In spin pumping, the spin current is driven by a non-equilibrium state in the ferrimagnet due to the absorption of microwave radiation (FMR). Spin pumping is the focus of this thesis. Spin pumping is discussed in new contexts, such as strong coupling (chapter 4) and that of multi-sublattice magnetic systems, ferrimagnets and antiferromagnets (chapter 5). The non-equilibrium state necessary to drive a spin current can also be induced in the normal metal, by driving a charge current through that layer (the spin Hall effect). This is the basis of the spin Hall magnetoresistance (SMR) effect, the frequency dependence of which is the subject of chapter 6. In the following, the most important results of this thesis are summarized.

In chapter 3, we present spin pumping experiments in a series of thin film YIG/Pt bilayers. A variation of the Pt layer thickness enables us to determine the spin diffusion length in the Pt layer $\lambda_{\mathrm{SD,Pt}} = (1.6 \pm 0.5)\,\mathrm{nm}$ as well as the spin Hall angle, $\theta_{\mathrm{SH}} = 0.06 \pm 0.04$. The previously reported values of these parameters span several orders of magnitude. Since platinum has become the standard normal metal to use in experiments such as spin pumping, the spin Seebeck effect, and spin Hall magnetoresistance, these parameters are crucial to the quantitative analysis of these experiments. Recent studies of dc transport spin Hall magnetoresistance in YIG/platinum bilayers [28, 64] find values of the spin Hall angle and the spin diffusion length compatible to the ones determined here, which again confirms the similarities between the SMR and spin pumping mechanisms. This has already been pointed out in Ref. [57], which includes many of the data described in this chapter. The data also feature in Ref. [44], where damping-detected and electrically-detected spin pumping are compared. Using the approach laid out here, the spin Hall angle and spin diffusion length

of metals other than platinum could in principle also be determined, as has been done in Ref. [140], where however the thickness of the normal metal layer was not varied. Thus instead of directly determining the spin diffusion length, that analysis is dependent on literature values.

We furthermore varied the thickness of the YIG layer, and observed that the interface spin current in thick YIG layers ($t_{\mathrm{YIG}} > 60\,\mathrm{nm}$) increases with YIG thickness. Since spin pumping is understood as an interface effect, this increase is unexpected. The increase is possibly due to spin pumping from non-uniform spin wave modes, the excitation of which could be concentrated at the YIG/Pt interface, leading to an increased spin pumping efficiency. However, spin pumping experiments in which the thickness of the YIG is varied more systematically should be performed, in a broader range of YIG thicknesses and also using YIG thicknesses greater than 200 nm, the maximum YIG thickness available in our experiments.

Spin pumping in YIG/Pt, which is strongly coupled to the standing wave mode in a microwave cavity is the subject of chapter 4. In microwave cavity based ferromagnetic resonance, the coupling between the cavity mode and the ferromagnetic resonance mode scales as $g_{\mathrm{eff}} \propto \sqrt{N_{\mathrm{s}}}$, where N_{s} is the number of spins in the magnetic system. A large coupling rate g_{eff} compared to the relaxation rate of the cavity and the spin system causes a hybridization of the cavity mode and the magnetic resonance mode of the YIG. This regime is called strong coupling. In the frequency vs. magnetic field dispersion, an anticrossing of the two modes is observed. Experimentally, strong coupling is usually measured by recording the microwave cavity response. In YIG, strong coupling to a cavity has first been demonstrated in Ref. [74], to which the data analysis was contributed in the course of this thesis. We here investigate the possibility of measuring the spin excitation directly, in addition to the cavity response, by measuring the electrically detected spin pumping signal. First, we develop a model to predict the magnetic field and frequency dependent excitation of the spin system and the microwave cavity, based on input-output theory. Using this model, we calculate the resulting reflection of microwave radiation at the microwave cavity and the dc voltage measured in electrically detected spin pumping. The model is applicable irrespective of the coupling strength, both in the strong coupling and in the weak coupling regime. If the spin mixing conductance at the interface, the spin Hall angle, and the spin diffusion length of the normal metal are known, the model can also be used to predict the electrically detected spin pumping voltage amplitude from FMR

data. This has previously been only possible in the weakly coupled case and at the microwave cavity frequency. We also predict that the spin pumping voltage signal at constant microwave power is substantially reduced when using magnetic layers of greater volume, relative to thin film ferromagnets. This is due to the fact that the magnetization excitation is distributed over the whole of the bulk sample, while only the spin excitation close to the YIG/Pt interface results in pumped spin current.

To test the model, we perform ferromagnetic resonance as well as spin pumping first on a thin film YIG/Pt bilayer, as a function of both microwave frequency and external magnetic field. The observed microwave reflection and spin pumping voltage are qualitatively and quantitatively consistent with our model calculations. We then perform spin pumping on a bulk YIG/Pt sample, again as a function of microwave frequency and magnetic field. In this sample, the cavity-spin system coupling strength is substantially increased as evidenced by the observed anticrossing in the microwave reflection data. Due to the bulk character of the YIG, the spin pumping signal is predicted to be smaller by two orders of magnitude in this sample compared to the thin film YIG/Pt bilayer experiment. The dc voltage data do not show a signature consistent with the spin pumping. Instead, we observe a dc voltage which we attribute to the spin Seebeck effect, due to microwave heating of the sample. The ability to differentiate between the signature of the spin Seebeck effect and spin pumping is one of the merits of the proposed model.

We conclude that in order to observe spin pumping in the strong coupling regime, the number of spins in the YIG layer needs to be very finely tuned. This is due to the fact that spin pumping is more easily observed in samples comprising a thin magnetic film, while a thick magnetic film is required for strong coupling. Additionally, the YIG needs to be of very high quality to ensure low damping, making it easier to reach the strong coupling regime, even with lower coupling strength. Using thick films of yttrium iron garnet layer grown by liquid phase epitaxy as the magnetic layer for spin pumping in strong coupling seems promising, as these films have excellent damping properties and can be grown to the required thickness [88]. Spin pumping should then be more easily observable and time-dependent, strong coupling, spin pumping experiments can be envisioned as a next step. This experiment would yield the time-dependent spin excitation of the YIG, in addition to the time-dependent excitation of the cavity, which has already been observed in a YIG single crystal coupled to a microwave cavity [65].

In chapter 5, we investigate in detail spin pumping in magnetic systems with more than one magnetic sublattice, such as ferrimagnets and antiferromagnets. In ferrimagnetic spin pumping, our model, based on the conservation of angular momentum, shows that it is irrelevant for the sign of the pumped spin current which magnetic sublattice(s) are in contact with the normal metal. Rather, the sign of the spin current pumped by the ferromagnetic resonance mode is solely determined by the sign of the effective gyromagnetic ratio of the ferrimagnet. This resolves a point heatedly debated in the community. We compare these theoretical conjectures with electrically detected spin pumping measurements, recorded using an indium and yttrium doped gadolinium iron garnet/platinum bilayer. Gadolinium iron garnet features three magnetic sublattices, of which the magnetization of the gadolinium sublattice is strongly temperature dependent due to its relatively weak exchange coupling. Therefore, a magnetization compensation temperature exists, at which the net magnetization of the iron and the magnetization of the gadolinium are of equal magnitude. If the temperature is swept over the compensation temperature, the sublattice magnetization orientations are inverted. The spin pumping spin current observed in experiment does however not change sign at the compensation temperature, which is consistent with our model. To further corroborate the model, spin pumping should be performed on a compensating ferrimagnet featuring a large separation between the magnetization compensation temperatures T_{M} and the angular momentum compensation temperature T_{L}. Since the sign of the gyromagnetic ratio inverts T_{M} and T_{L}, an inversion of the sign of the spin pumping voltage signal should then be observable in this temperature range. This regime is inherently inaccessible using ferromagnets, where the gyromagnetic ratio is always negative. Replacing the gadolinium ions of GdIG with other rare earth ions with non-zero orbital angular momentum (e.g. dysprosium [141]) should result in a rare earth sublattice gyromagnetic ratio which is considerably lower than that of the iron sublattices. Since the separation of the compensation temperatures depends on the difference of the sublattice gyromagnetic ratios, such garnets should be promising candidates such an experiment. The results of chapter 5.1 will be published as Ref. [99].

Simultaneously to spin pumping, we perform spin Seebeck experiments on the same indium and yttrium doped gadolinium iron garnet/platinum bilayer. In the spin Seebeck voltage, we find two sign changes in the pumped spin current, similar to the data of Ref. [92]. This leads us to conclude that the exchange modes, where the

magnetic sublattices precess non-collinearly, are very relevant for the spin Seebeck effect in ferrimagnets. These exchange modes can be thermally excited, but are of much higher frequencies than the ferromagnetic modes and so are not excited in conventional spin pumping experiments at GHz frequencies. This explains the difference in the temperature dependence between the spin Seebeck effect and spin pumping voltages. Our model approach could also be used to describe spin pumping due to excitation of the exchange modes which are relevant for the spin Seebeck effect. However, the temperature dependent occupation of the exchange magnon modes and the sign of their (temperature dependent) effective gyromagnetic ratios are needed for a quantitative description of the spin Seebeck effect voltage as a function of temperature within our model. The method of inferring a pumped spin current from the angular momentum balance is therefore also relevant beyond ferrimagnetic spin pumping.

We predict the pumped spin current in antiferromagnet/normal metal bilayers. Antiferromagnets comprise two identical, antiparallel sublattices, which are excited in the non-collinear exchange mode in antiferromagnetic resonance. According to our model, spin pumping in antiferromagnets is less efficient than spin pumping in ferromagnets, which is due to the small change in total angular momentum during antiferromagnetic precession, in which the sublattices are aligned nearly antiparallelly. In the antiferromagnet MnF_2, spin pumping is calculated to be one third as efficient as in a ferromagnet. This can be compared to Ref. [100], where it is claimed that spin pumping in antiferromagnets is efficient, but the absorption of microwave radiation by the antiferromagnet is not. Therefore Ref. [100] also predicts a comparatively lower spin pumping voltage in antiferromagnets. We discuss a spin pumping experiment using a bilayer of Pt and MnF_2. We do not observe the signature of spin pumping in the dc voltage measured, owing to the relatively low microwave magnetic driving field achieved in this experiment and the lower efficiency of spin pumping in an antiferromagnet. Performing the same experiment in a setup capable of delivering greater microwave power to the sample and thus greater microwave magnetic fields to drive the antiferromagnetic resonance could confirm our model calculations for the antiferromagnet.

The spin Hall magnetoresistance is a recently discovered magnetoresistive effect in ferromagnetic insulator/normal metal bilayers. It is based on the creation of spin currents in the normal metal layer by the spin Hall effect and their subsequent ab-

sorption in the ferromagnetic layer. The absorption depends on the orientation of the magnetization of the ferromagnetic insulator. If the spin current is absorbed, the resistance of the Pt film increases. To date SMR has only been investigated at dc currents. In chapter 6, we investigate the spin Hall magnetoresistance at microwave frequency ac currents. For this purpose, we design a test fixture for a YIG/Pt bilayer that enables us to drive a calibrated microwave ac current through the Pt film. We find that the magnetoresistance ratio does not change as a function of frequency up to at least 3 GHz. Our experiment suggests that the magnetoresistance ratio is constant also at higher frequencies, but calibration issues preclude us from a quantitative analysis at frequencies above 3 GHz. We can thus deduce the frequency independence of the spin Hall angle θ_{SH}, on which the magnetoresistance ratio depends quadratically, for frequencies up to 3 GHz. From a more applied perspective, our experiment proves that the magnetization direction of a ferromagnet can be read out using spin Hall magnetoresistance with frequencies of at least 3 GHz. These results are published in Ref. [126].

In conclusion, we have investigated the generation of pure spin currents in magnetic insulator/normal metal bilayers. The transfer of angular momentum as a spin current over the magnetic insulator/normal metal is also a focus of this thesis. We describe spin pumping and the spin Hall magnetoresistance and also touch on the subject of the spin Seebeck effect. All of these effects depend on the transfer of angular momentum between the two layers. The investigation of these effects in new contexts, namely spin pumping in the strong coupling regime, spin pumping employing compensating ferrimagnets and antiferromagnets as the magnetic layer, and spin Hall magnetoresistance at GHz frequencies, provides new insight into the interplay of spin currents, magnetization and angular momentum.

Appendix A

List of YIG/Pt Bilayer Samples

In Tabs. A.1 and A.2, we list the samples used in chapter 3.

Table A.1: YIG/Pt bilayers with approximately constant YIG layer thickness and varying Pt thickness.

	t_{YIG} (nm)	t_{Pt} (nm)
YIG 58	56	1.3
YIG 57	58	2.2
YIG 53	53	2.5
YIG 52	50	7
YIG 60	54	8.5
YY 24	60	9.7
YIG 59	61	11.2
YY26	60	12.8
YIG 61	54	16.9
YY21	61	19.5

Table A.2: YIG/Pt bilayers with varying YIG layer thickness

	t_{YIG} (nm)	t_{Pt} (nm)
YIG 105	16	2.8
YIG 22	18	7
YIG 32	25	7
YIG 19	44	7
YIG 20	54	6.1
YIG 118	107	2.7
YIG 21	176	7
YIG 113	199	2.7

Appendix B

Homodyne Dectection Circuit

In the course of this thesis, a homodyne detection circuit was assembled in order to measure ferromagnetic resonance of magnetic thin film samples in a X-band microwave cavity. This circuit is similar to those found in commercially available electron paramagnetic resonance spectrometers. It supports frequencies $7\,\mathrm{GHz} < \omega/(2\pi) < 12\,\mathrm{GHz}$. It is optimized for relatively high powers (tens of mW), to enable the measurement of electrically detected spin pumping at the same time as ferromagnetic resonance. However, ferromagnetic and electron paramagnetic resonance experiments can also be performed at nanowatts of power using attenuators integrated in the RF branch of the circuit. The detection circuit is sketched in Fig. B.1. In the following, we list the parts of the detection circuit.

- 10 dB directional coupler, Marki Microwave, C10 0226: splits the microwave signal provided by a microwave source (input power fixed at 24 dBm for optimum

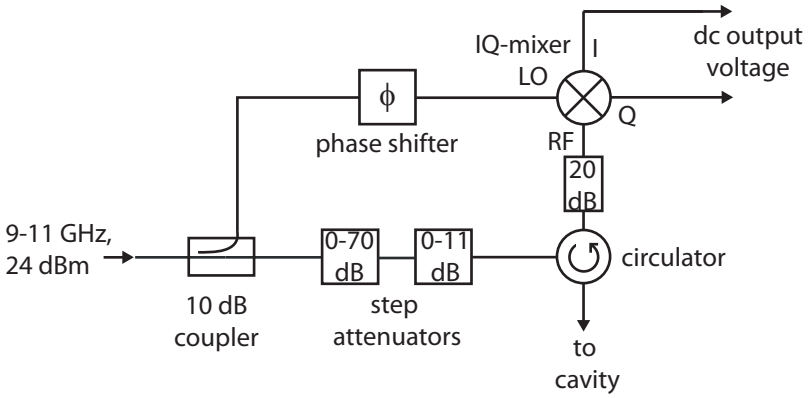

Figure B.1: The homodyne detection circuit assembled in the course of this thesis. For a list of parts, see text.

performance) in two. One part of the signal (RF branch) is used to drive FMR in the microwave cavity, the other provides the local oscillator (LO branch) tone to the mixer.

- Manual step attenuators, Agilent 8495B-002 and Agilent 8494B-002: provide control of the microwave power incident on the microwave cavity.
- Circulator Narda West 0712: channels incoming microwave radiation to the microwave cavity; the reflected microwave signal from the resonator (containing the FMR signal) is directed to the IQ mixer.
- Phase shifter ATM, Model P 1506: controls the phase of the LO branch.
- IQ mixer, Marki Microwave IQ-0618: homodynes the FMR signal, and outputs dc voltages at the I and Q ports, which can be recorded using dc electronics.
- 20 dB attenuator: shields the IQ mixer from excessive power on the RF port. Can be omitted if it is necessary to measure small signals.

Publications

- H. Huebl, C. W. Zollitsch, J. Lotze, F. Hocke, M. Greifenstein, A. Marx, R. Gross, and S. T. B. Goennenwein, *High Cooperativity in Coupled Microwave Resonator Ferrimagnetic Insulator Hybrids*, Phys. Rev. Lett. 111, 127003 (2013).

- M. Weiler, M. Althammer, M. Schreier, J. Lotze, M. Pernpeintner, S. Meyer, H. Huebl, R. Gross, A. Kamra, J. Xiao, Y.-T. Chen, H. Jiao, G. E. W. Bauer, and S. T. B. Goennenwein, *Experimental Test of the Spin Mixing Interface Conductivity Concept*, Phys. Rev. Lett. 111, 176601 (2013).

- M. Schreier, T. Chiba, A. Niedermayr, J. Lotze, H. Huebl, S. Geprägs, S. Takahashi, G. E. W. Bauer, R. Gross, and S. T. B. Goennenwein, *Current-induced spin torque resonance of a magnetic insulator*, arXiv 1412.7460 (2014).

- A. Kamra, S. von Hoesslin, N. Roschewsky, J. Lotze, M. Schreier, R. Gross, S. T. B. Goennenwein, H. Huebl, *Torque differential magnetometry using quartz tuning forks*, arXiv 1404.6341 (2014).

- J. Lotze, H. Huebl, R. Gross, and S. T. B. Goennenwein, *Spin Hall magnetoimpedance*, Phys. Rev. B 90, 174419 (2014).

- M. Schreier, G. E. W. Bauer, V. I. Vasyuchka, J. Flipse, K. Uchida, J. Lotze, V. Lauer, A. V. Chumak, A. A. Serga, S. Daimon, T. Kikkawa, E. Saitoh, B. J. van Wees, B. Hillebrands, R. Gross, and S. T. B. Goennenwein, *Sign of inverse spin Hall voltages generated by ferromagnetic resonance and temperature gradients in yttrium iron garnet platinum bilayers*, Journal of Physics D: Applied Physics 48, 025001 (2015).

- M. Härtinger, C. H. Back, J. Lotze, M. Weiler, S. Geprägs, H. Huebl, S. T. B. Goennenwein, and G. Woltersdorf, *Spin pumping in YIG/Pt bilayers as a function of layer thickness*, submitted (2015).

- J. Lotze, K. Ganzhorn, S. Geprägs, F. della Coletta, H. Skarsvåag, A. Brataas, H. Huebl, R. Gross, and S. T. B. Goennenwein, *Spin Pumping in Gadolinium Iron Garnet / Platinum bilayers*, submitted (2015)

Bibliography

[1] S. A. Wolf, D. D. Awschalom, R. A. Buhrman, J. M. Daughton, S. von Molnár, M. L. Roukes, A. Y. Chtchelkanova, and D. M. Treger, Science **294**, 1488 (2001).

[2] I. Žutić, J. Fabian, and S. Das Sarma, Rev. Mod. Phys. **76**, 323 (2004).

[3] S. Bader and S. Parkin, Annual Review of Condensed Matter Physics **1**, 71 (2010).

[4] S. Murakami, N. Nagaosa, and S.-C. Zhang, Science **301**, 1348 (2003).

[5] S. Datta and B. Das, Applied Physics Letters **56** (1990).

[6] M. N. Baibich, J. M. Broto, A. Fert, F. N. Van Dau, F. Petroff, P. Etienne, G. Creuzet, A. Friederich, and J. Chazelas, Phys. Rev. Lett. **61**, 2472 (1988).

[7] G. Binasch, P. Grünberg, F. Saurenbach, and W. Zinn, Phys. Rev. B **39**, 4828 (1989).

[8] J. Slonczewski, Journal of Magnetism and Magnetic Materials **159**, L1 (1996).

[9] L. Berger, Phys. Rev. B **54**, 9353 (1996).

[10] D. Ralph and M. Stiles, Journal of Magnetism and Magnetic Materials **320**, 1190 (2008).

[11] O. Mosendz, J. E. Pearson, F. Y. Fradin, G. E. W. Bauer, S. D. Bader, and A. Hoffmann, Phys. Rev. Lett. **104**, 046601 (2010).

[12] F. Czeschka, L. Dreher, M. Brandt, M. Weiler, M. Althammer, I.-M. Imort, G. Reiss, A. Thomas, W. Schoch, W. Limmer, H. Huebl, R. Gross, and S. Goennenwein, Phys. Rev. Lett. **107**, 046601 (2011).

[13] L. H. Vilela-Leão, G. L. da Silva, C. Salvador, S. M. Rezende, and A. Azevedo, J. Appl. Phys. **109**, (2011).

[14] C. H. Du, H. L. Wang, Y. Pu, T. L. Meyer, P. M. Woodward, F. Y. Yang, and P. C. Hammel, Phys. Rev. Lett. **111**, 247202 (2013).

[15] M. Weiler, J. M. Shaw, H. T. Nembach, and T. J. Silva, Phys. Rev. Lett. **113**, 157204 (2014).

[16] C. Hahn, G. de Loubens, M. Viret, O. Klein, V. V. Naletov, and J. Ben Youssef, Phys. Rev. Lett. **111**, 217204 (2013).

[17] K. Uchida, H. Adachi, T. Ota, H. Nakayama, S. Maekawa, and E. Saitoh, Appl. Phys. Lett. **97**, 172505 (2010).

[18] M. Weiler, M. Althammer, F. D. Czeschka, H. Huebl, M. S. Wagner, M. Opel, I.-M. Imort, G. Reiss, A. Thomas, R. Gross, and S. T. B. Goennenwein, Phys. Rev. Lett. **108**, 106602 (2012).

[19] M. Schreier, A. Kamra, M. Weiler, J. Xiao, G. E. W. Bauer, R. Gross, and S. T. B. Goennenwein, Phys. Rev. B **88**, 094410 (2013).

[20] S. Hoffman, K. Sato, and Y. Tserkovnyak, Phys. Rev. B **88**, 064408 (2013).

[21] D. Meier, T. Kuschel, L. Shen, A. Gupta, T. Kikkawa, K. Uchida, E. Saitoh, J.-M. Schmalhorst, and G. Reiss, Phys. Rev. B **87**, 054421 (2013).

[22] D. Qu, S. Y. Huang, J. Hu, R. Wu, and C. L. Chien, Phys. Rev. Lett. **110**, 067206 (2013).

[23] S. M. Rezende, R. L. Rodríguez-Suárez, R. O. Cunha, A. R. Rodrigues, F. L. A. Machado, G. A. Fonseca Guerra, J. C. Lopez Ortiz, and A. Azevedo, Phys. Rev. B **89**, 014416 (2014).

[24] M. Dyakonov and V. Perel, Physics Letters A **35**, 459 (1971).

[25] J. E. Hirsch, Phys. Rev. Lett. **83**, 1834 (1999).

[26] Y. K. Kato, R. C. Myers, A. C. Gossard, and D. D. Awschalom, Science **306**, 1910 (2004).

[27] H. Nakayama, M. Althammer, Y.-T. Chen, K. Uchida, Y. Kajiwara, D. Kikuchi, T. Ohtani, S. Geprägs, M. Opel, S. Takahashi, R. Gross, G. E. W. Bauer, S. T. B. Goennenwein, and E. Saitoh, Phys. Rev. Lett. **110**, 206601 (2013).

[28] M. Althammer, S. Meyer, H. Nakayama, M. Schreier, S. Altmannshofer, M. Weiler, H. Huebl, S. Geprägs, M. Opel, R. Gross, D. Meier, C. Klewe, T. Kuschel, J.-M. Schmalhorst, G. Reiss, L. Shen, A. Gupta, Y.-T. Chen, G. E. W. Bauer, E. Saitoh, and S. T. B. Goennenwein, Phys. Rev. B **87**, 224401 (2013).

[29] Y.-T. Chen, S. Takahashi, H. Nakayama, M. Althammer, S. T. B. Goennenwein, E. Saitoh, and G. E. W. Bauer, Phys. Rev. B **87**, 144411 (2013).

[30] X. Marti, I. Fina, C. Frontera, J. Liu, P. Wadley, Q. He, R. J. Paull, J. D. Clarkson, J. Kudrnovský, I. Turek, J. KuneŽ, D. Yi, J.-H. Chu, C. T. Nelson, L. You, E. Arenholz, S. Salahuddin, J. Fontcuberta, T. Jungwirth, and R. Ramesh, Nature Materials **13**, 367 (2014).

[31] A. S. Núñez, R. A. Duine, P. Haney, and A. H. MacDonald, Phys. Rev. B **73**, 214426 (2006).

[32] Y. Tserkovnyak, A. Brataas, and G. E. W. Bauer, Phys. Rev. B **66**, 224403 (2002).

[33] Y. Tserkovnyak, A. Brataas, and G. E. W. Bauer, Phys. Rev. Lett. **88**, 117601 (2002).

[34] Y. Tserkovnyak, A. Brataas, G. E. W. Bauer, and B. I. Halperin, Rev. Mod. Phys. **77**, 1375 (2005).

[35] O. Mosendz, V. Vlaminck, J. E. Pearson, F. Y. Fradin, G. E. W. Bauer, S. D. Bader, and A. Hoffmann, Phys. Rev. B **82**, 214403 (2010).

[36] E. Saitoh, M. Ueda, H. Miyajima, and G. Tatara, Applied Physics Letters **88**, 182509 (2006).

[37] F. Czeschka, Spin Currents in Metallic Nanostructures, Ph.D. thesis, Walther-Meißner Institut (2011).

[38] D. Wei, M. Obstbaum, M. Ribow, C. H. Back, and G. Woltersdorf, Nature Communications **5**, 3768 (2014).

[39] S. Vonsovskii, Ferromagnetic Resonance (Israel Program for Scientific Translations, 1964).

[40] D. Stancil and A. Prabhakar, Spin Waves: Theory and Applications (Springer, 2009).

[41] A. Morrish, The Physical Principles of Magnetism, An IEEE Press classic reissue (Wiley, 2001).

[42] S. Chikazumi and C. Graham, Physics of Ferromagnetism, International Series of Monographs on Physics (Clarendon Press, 1997).

[43] Y. Guan, W. Bailey, E. Vescovo, C.-C. Kao, and D. Arena, Journal of Magnetism and Magnetic Materials **312**, 374 (2007).

[44] M. Härtinger, C. Back, J. Lotze, M. Weiler, S. Geprägs, H. Huebl, S. Goennenwein, and G. Woltersdorf, submitted (2015).

[45] N. F. Mott, Proceedings of the Royal Society of London A: Mathematical, Physical and Engineering Sciences **124**, 425 (1929).

[46] L. Berger, Phys. Rev. B **2**, 4559 (1970).

[47] R. Karplus and J. M. Luttinger, Phys. Rev. **95**, 1154 (1954).

[48] K. Ando, T. Yoshino, and E. Saitoh, Applied Physics Letters **94**, 152509 (2009).

[49] H. Jiao and G. E. W. Bauer, Phys. Rev. Lett. **110**, 217602 (2013).

[50] S. A. Manuilov, S. I. Khartsev, and A. M. Grishin, Journal of Applied Physics **106**, 123917 (2009).

[51] S. S. Kalarickal, P. Krivosik, M. Wu, C. E. Patton, M. L. Schneider, P. Kabos, T. J. Silva, and J. P. Nibarger, Journal of Applied Physics **99**, 093909 (2006).

[52] Y. S. Gui, N. Mecking, X. Zhou, G. Williams, and C.-M. Hu, Phys. Rev. Lett. **98**, 107602 (2007).

[53] L. Bai, P. Hyde, Y. S. Gui, C.-M. Hu, V. Vlaminck, J. E. Pearson, S. D. Bader, and A. Hoffmann, Phys. Rev. Lett. **111**, 217602 (2013).

[54] A. Azevedo, L. H. Vilela-Leão, R. L. Rodríguez-Suárez, A. F. Lacerda Santos, and S. M. Rezende, Phys. Rev. B **83**, 144402 (2011).

[55] R. Iguchi, K. Sato, D. Hirobe, S. Daimon, and E. Saitoh, Applied Physics Express **7**, 013003 (2014).

[56] T. Chiba, G. E. W. Bauer, and S. Takahashi, Phys. Rev. Applied **2**, 034003 (2014).

[57] M. Weiler, M. Althammer, M. Schreier, J. Lotze, M. Pernpeintner, S. Meyer, H. Huebl, R. Gross, A. Kamra, J. Xiao, Y.-T. Chen, H. Jiao, G. E. W. Bauer, and S. T. B. Goennenwein, Phys. Rev. Lett. **111**, 176601 (2013).

[58] Z. Qiu, K. Ando, K. Uchida, Y. Kajiwara, R. Takahashi, H. Nakayama, T. An, Y. Fujikawa, and E. Saitoh, Applied Physics Letters **103**, 092404 (2013).

[59] T. Kimura, Y. Otani, T. Sato, S. Takahashi, and S. Maekawa, Phys. Rev. Lett. **98**, 156601 (2007).

[60] L. Liu, T. Moriyama, D. C. Ralph, and R. A. Buhrman, Phys. Rev. Lett. **106**, 036601 (2011).

[61] K. Ando, S. Takahashi, K. Harii, K. Sasage, J. Ieda, S. Maekawa, and E. Saitoh, Phys. Rev. Lett. **101**, 036601 (2008).

[62] S. Mizukami, Y. Ando, and T. Miyazaki, Phys. Rev. B **66**, 104413 (2002).

[63] H. Kurt, R. Loloee, K. Eid, W. P. Pratt, and J. Bass, Applied Physics Letters **81**, 4787 (2002).

[64] S. Meyer, M. Althammer, S. GeprÃďgs, M. Opel, R. Gross, and S. T. B. Goennenwein, Applied Physics Letters **104**, 242411 (2014).

[65] X. Zhang, C.-L. Zou, L. Jiang, and H. X. Tang, Phys. Rev. Lett. **113**, 156401 (2014).

[66] H. Wu, R. E. George, J. H. Wesenberg, K. Mølmer, D. I. Schuster, R. J. Schoelkopf, K. M. Itoh, A. Ardavan, J. J. L. Morton, and G. A. D. Briggs, Phys. Rev. Lett. **105**, 140503 (2010).

[67] Y. Kubo, C. Grezes, A. Dewes, T. Umeda, J. Isoya, H. Sumiya, N. Morishita, H. Abe, S. Onoda, T. Ohshima, V. Jacques, A. Dréau, J.-F. Roch, I. Diniz, A. Auffeves, D. Vion, D. Esteve, and P. Bertet, Phys. Rev. Lett. **107**, 220501 (2011).

[68] A. Imamoğlu, Phys. Rev. Lett. **102**, 083602 (2009).

[69] O. O. Soykal and M. E. Flatté, Phys. Rev. B **82**, 104413 (2010).

[70] O. O. Soykal and M. E. Flatté, Phys. Rev. Lett. **104**, 077202 (2010).

[71] R. H. Dicke, Phys. Rev. **93**, 99 (1954).

[72] M. Tavis and F. W. Cummings, Phys. Rev. **170**, 379 (1968).

[73] I. Chiorescu, N. Groll, S. Bertaina, T. Mori, and S. Miyashita, Phys. Rev. B **82**, 024413 (2010).

[74] H. Huebl, C. W. Zollitsch, J. Lotze, F. Hocke, M. Greifenstein, A. Marx, R. Gross, and S. T. B. Goennenwein, Phys. Rev. Lett. **111**, 127003 (2013).

[75] Y. Tabuchi, S. Ishino, T. Ishikawa, R. Yamazaki, K. Usami, and Y. Nakamura, Phys. Rev. Lett. **113**, 083603 (2014).

[76] Y. Cao, P. Yan, H. Huebl, S. T. B. Goennenwein, and G. E. W. Bauer, Phys. Rev. B **91**, 094423 (2015).

[77] A. A. Clerk, M. H. Devoret, S. M. Girvin, F. Marquardt, and R. J. Schoelkopf, Rev. Mod. Phys. **82**, 1155 (2010).

[78] D. Walls and G. Milburn, Quantum Optics, SpringerLink: Springer e-Books (Springer, 2008).

[79] T. Holstein and H. Primakoff, Phys. Rev. **58**, 1098 (1940).

[80] C. Poole, Electron Spin Resonance: A Comprehensive Treatise on Experimental Techniques/Second Edition, Dover books on physics (Dover Publ., 1983).

[81] M. Opel, J. Phys. D: Appl. Phys. **45**, 033001 (2012).

[82] M. A. Gilleo and S. Geller, Phys. Rev. **110**, 73 (1958).

[83] E. Abe, H. Wu, A. Ardavan, and J. J. L. Morton, Applied Physics Letters **98**, 251108 (2011).

[84] P. F. Herskind, A. Dantan, J. P. Marler, M. Albert, and M. Drewsen, Nature Physics **5**, 494 (2009).

[85] K. Ando, Y. Kajiwara, S. Takahashi, S. Maekawa, K. Takemoto, M. Takatsu, and E. Saitoh, Phys. Rev. B **78**, 014413 (2008).

[86] M. Schreier, N. Roschewsky, E. Dobler, S. Meyer, H. Huebl, R. Gross, and S. T. B. Goennenwein, Applied Physics Letters **103**, 242404 (2013).

[87] E. G. Spencer, R. C. LeCraw, and A. M. Clogston, Phys. Rev. Lett. **3**, 32 (1959).

[88] P. Görnert, R. Hergt, E. Sinn, M. Wendt, B. Keszei, and J. Vandlik, Journal of Crystal Growth **87**, 331 (1988).

[89] B. Heinrich, C. Burrowes, E. Montoya, B. Kardasz, E. Girt, Y.-Y. Song, Y. Sun, and M. Wu, Phys. Rev. Lett. **107**, 066604 (2011).

[90] V. Castel, N. Vlietstra, B. J. van Wees, and J. Ben Youssef, Phys. Rev. B **90**, 214434 (2014).

[91] J. Lustikova, Y. Shiomi, Z. Qiu, T. Kikkawa, R. Iguchi, K. Uchida, and E. Saitoh, Journal of Applied Physics **116**, 153902 (2014).

[92] S. Geprägs, A. Kehlberger, T. Schulz, C. Mix, F. Della Coletta, S. Meyer, A. Kamra, M. Althammer, G. Jakob, H. Huebl, R. Gross, S. T. B. Goennenwein, and M. Kläui, arXiv 1405.4971 (2014).

[93] G. F. Dionne, Journal of Applied Physics **41**, 4874 (1970).

[94] M. Gilleo, Journal of Physics and Chemistry of Solids **13**, 33 (1960).

[95] K. P. Belov, Physics-Uspekhi **39**, 623 (1996).

[96] B. Lax and K. Button, Microwave ferrites and ferrimagnetics, Lincoln Laboratory publications (McGraw-Hill, 1962).

[97] R. Giles and M. Mansuripur, J. Mag. Soc. Japan **15-S1**, 299 (1991).

[98] K. Ganzhorn, Experimental Study of Spin Currents in Compensated Rare Earth Garnets, Master's thesis, Walther-Meißner Institut (2014).

[99] J. Lotze, K. Ganzhorn, S. Geprägs, F. della Coletta, H. Skarsvåg, A. Brataas, H. Huebl, R. Gross, and S. T. B. Goennenwein, submitted (2015).

[100] R. Cheng, J. Xiao, Q. Niu, and A. Brataas, Phys. Rev. Lett. **113**, 057601 (2014).

[101] F. Brown and D. Park, Phys. Rev. **93**, 381 (1954).

[102] S. Geschwind and L. R. Walker, Journal of Applied Physics **30**, S163 (1959).

[103] M. Schreier, G. E. W. Bauer, V. I. Vasyuchka, J. Flipse, K. Uchida, J. Lotze, V. Lauer, A. V. Chumak, A. A. Serga, S. Daimon, T. Kikkawa, E. Saitoh, B. J. van Wees, B. Hillebrands, R. Gross, and S. T. B. Goennenwein, Journal of Physics D: Applied Physics **48**, 025001 (2015).

[104] J. Bernasconi and D. Kuse, Phys. Rev. B **3**, 811 (1971).

[105] G. F. Dionne, Journal of Applied Physics **42**, 2142 (1971).

[106] R. Pauthenet, Journal of Applied Physics **29**, 253 (1958).

[107] R. Pauthenet, Journal of Applied Physics **30**, S290 (1959).

[108] T. Chiba, M. Schreier, G. E. W. Bauer, and S. Takahashi, Journal of Applied Physics **117**, 17 (2015).

[109] M. Schreier, T. Chiba, A. Niedermayr, J. Lotze, H. Huebl, S. Geprägs, S. Takahashi, G. E. W. Bauer, R. Gross, and S. T. B. Goennenwein, arXiv 1412.7460 (2014).

[110] S. Geschwind, Phys. Rev. Lett. **3**, 207 (1959).

[111] G. P. Rodrigue, H. Meyer, and R. V. Jones, Journal of Applied Physics **31**, S376 (1960).

[112] R. K. Wangsness, Phys. Rev. **93**, 68 (1954).

[113] G. P. Rodrigue, H. Meyer, and R. V. Jones, Journal of Applied Physics **31**, S376 (1960).

[114] B. A. Calhoun, J. Overmeyer, and W. V. Smith, Phys. Rev. **107**, 993 (1957).

[115] A. Gurevich and G. Melkov, Magnetization Oscillations and Waves (Taylor & Francis, 1996).

[116] M. P. Ross, Spin Dynamics in an Antiferromagnet, Master's thesis, Walther-Meißner Institut (2013).

[117] F. Keffer and C. Kittel, Phys. Rev. **85**, 329 (1952).

[118] I. S. Jacobs, Journal of Applied Physics **32** (1961).

[119] M. Hagiwara, K. Katsumata, H. Yamaguchi, M. Tokunaga, I. Yamada, M. Gross, and P. Goy, International Journal of Infrared and Millimeter Waves **20**, 617 (1999).

[120] J. Coey, Magnetism and Magnetic Materials, Magnetism and Magnetic Materials (Cambridge University Press, 2010).

[121] J. P. Kotthaus and V. Jaccarino, Phys. Rev. Lett. **28**, 1649 (1972).

[122] F. M. Johnson and A. H. Nethercot, Phys. Rev. **114**, 705 (1959).

[123] C. Kittel, Introduction to Solid State Physics (Wiley, 2004).

[124] T. Kampfrath, M. Battiato, P. Maldonado, G. Eilers, J. Nötzold, S. Mährlein, V. Zbarsky, F. Freimuth, Y. Mokrousov, S. Blügel, M. Wolf, I. Radu, P. M. Oppeneer, and M. Münzenberg, Nat. Nanotechnol. **8**, 256 (2013).

[125] V. Castel, N. Vlietstra, B. J. van Wees, and J. B. Youssef, Phys. Rev. B **86**, 134419 (2012).

[126] J. Lotze, H. Huebl, R. Gross, and S. T. B. Goennenwein, Phys. Rev. B **90**, 174419 (2014).

[127] A. Brataas, Y. V. Nazarov, and G. E. W. Bauer, Phys. Rev. Lett. **84**, 2481 (2000).

[128] Agilent Technologies, Advanced impedance measurement capability of the RF I-V method compared to the network analysis method, Application Note (2001).

[129] D. Pozar, Microwave Engineering, 4th Edition (Wiley Global Education, 2011).

[130] J. Dunsmore, Handbook of Microwave Component Measurements: with Advanced VNA Techniques (Wiley, 2012).

[131] F. Alimenti, P. Mezzanotte, L. Roselli, and R. Sorrentino, Microwave Theory and Techniques, IEEE Transactions on **49**, 142 (2001).

[132] F. Grover, Inductance Calculations: Working Formulas and Tables, Dover phoenix editions (Dover Publications, 2004).

[133] D. Sengupta and V. Liepa, Applied Electromagnetics and Electromagnetic Compatibility, Wiley Series in Microwave and Optical Engineering (Wiley, 2005).

[134] N. Vlietstra, J. Shan, V. Castel, B. J. van Wees, and J. Ben Youssef, Phys. Rev. B **87**, 184421 (2013).

[135] C. Hahn, G. de Loubens, O. Klein, M. Viret, V. V. Naletov, and J. Ben Youssef, Phys. Rev. B **87**, 174417 (2013).

[136] P. M. Haney, H.-W. Lee, K.-J. Lee, A. Manchon, and M. D. Stiles, Phys. Rev. B **87**, 174411 (2013).

[137] P. M. Haney, H.-W. Lee, K.-J. Lee, A. Manchon, and M. D. Stiles, Phys. Rev. B **88**, 214417 (2013).

[138] J. Sakurai, Modern Quantum Mechanics (Addison-Wesley, 1994).

[139] S. Takahashi and S. Maekawa, Sci. Tech. Adv. Mater. **9**, 014105 (2008).

[140] M. Weiler, J. Shaw, H. Nembach, and T. Silva, Magnetics Letters, IEEE **5**, 1 (2014).

[141] G. Dionne, Magnetic Oxides (Springer US, 2010).

Acknowledgments

During my years at the Walther-Meißner-Institut, many people contributed to this thesis. I would like to thank:

- Prof. Dr. Rudolf Gross, for giving me the opportunity to do my thesis work at the Walther-Meißner-Institut, and for his help with manuscript preparation.
- Dr. Sebastian Gönnenwein, for directly supervising me. For his many very good research ideas. For his enthusiasm during epic-length discussions. For always providing a fresh perspective. And for pushing me to always think just a little bit further.
- Dr. Hans Hübl, for often co-supervising me. For his helpful expertise with microwave technology, and always having just the right microwave component in his desk drawer. And for his frequent demand: 'Lächeln!', which was sometimes helpful.
- Everyone involved in sample fabrication at the WMI, in particular Sibylle Meyer, Dr. Matthias Althammer, Dr. Stephan Geprägs, and Dr. Matthias Opel. Without them, none of the experiments described in this thesis would have been possible.
- My diploma and master students, Philipp Ross and Kathrin Ganzhorn, for their very useful work which contributed to this thesis.
- Everyone at the WMI magnetism group, for their insight and for providing a very pleasant work environment.
- Prof. Dr. Martin Brandt, for his expertise in magnetic resonance, for measurement time on his machines, and for frequent loans of equipment.
- Dr. Akash Kamra, for bringing the worlds of theoretical and experimental physics together for me and being a lot of fun at the same time.

- Hans Skarsvåg and Prof. Arne Brataas, for extensive discussions about ferrimagnetic spin pumping.
- The technical staff at the WMI and everyone in the mechanical workshop.
- The other long-term residents of office 136, Alexander Baust and Manuel Schwarz, for a great office atmosphere and for good entertainment when a break was needed.
- Alma, for many things, but in this context for being a great reason for going to work.
- My parents, Brigitte and Klaus-Peter and my sister Katharina. For all their support.